ROYAL INSTITUTE
OF TECHNOLOGY

Reconstructing force from harmonic motion

DANIEL PLATZ

Doctoral Thesis
Stockholm, Sweden 2013

TRITA-FYS 2013:21
ISSN 0280-316X
ISRN KTH/FYS/--13:21--SE
ISBN 978-91-7501-792-1

KTH School of Engineering Sciences
SE-100 44 Stockholm
SWEDEN

Akademisk avhandling som med tillstånd av Kungl Tekniska högskolan framlägges till offentlig granskning för avläggande av teknologie doktorsexamen i fysik fredagen den 14 juni 2013 klockan 13.00 i FA31, Albanova University Center, Kungl Tekniska högskolan, Roslagstullsbacken 21, Stockholm.

Tryck: Universitetsservice US AB

Abstract

High-quality factor oscillators are often used in measurements of very small force since they exhibit an enhanced sensitivity in the narrow frequency band around resonance. Forces containing frequencies outside this frequency band are often not detectable and the total force acting on the oscillator remains unknown. In this thesis we present methods to efficiently use the available bandwidth around resonance to reconstruct the force from partial spectral information.

We apply the methods to dynamic atomic force microscopy (AFM) where a tip at the end of a small micro-cantilever oscillates close to a sample surface. By reconstructing the force between the tip and the surface we can deduce different properties of the surface. In contrast, in conventional AFM only one of the many frequency components of the time-dependent tip-surface force allowing for only qualitative conclusions about the tip-surface force.

To increase the number of measurable frequency components we developed Intermodulation AFM (ImAFM). ImAFM utilizes frequency mixing of a multifrequency drive scheme which generates many frequencies in the response to the nonlinear character of the tip-surface interaction. ImAFM, amplitude-modulated AFM and frequency-modulated AFM can be considered as special cases of narrow-band AFM, where the tip motion can be described by a rapidly oscillating part and a slowly-varying envelope function. Using the concept of force quadratures, each rapid oscillation cycle can be analyzed individually and ImAFM measurements can be interpreted as a rapid measurement of the dependence of the force quadratures on the oscillation amplitude or frequency. To explore the limits of the force quadratures description we introduce the force disk which is a complete description of the tip-surface force in narrow-band AFM at fixed static probe height.

We present a polynomial force reconstruction method for multifrequency AFM data. The polynomial force reconstruction is a linear approximative force reconstruction method which is based on finding the parameters of a model force which best approximates the tip-surface force. Another class of reconstruction methods are integral techniques which aim to invert the integral relation between the tip-surface force and the measured spectral data. We present an integral method, amplitude-dependence force spectroscopy (ADFS), which reconstructs the conservative tip-surface force from the amplitude-dependence of the force quadratures. Together with ImAFM we use ADFS to combine high-resolution AFM imaging at high speeds with highly accurate force measurements in each point of an image. For the measurement of dissipative forces we discuss how methods from tomography can be used to reconstruct forces that are a function of both tip position and velocity.

The methods developed in this thesis are not limited to dynamic AFM and we describe them in the general context of a harmonic oscillator subject to an external force. We hope that theses methods contribute to the transformation of AFM from a qualitative imaging modality into quantitative microscopy and we hope that they find application in other measurements which exploit the enhanced sensitivity of a high-quality factor oscillator.

Sammanfatting

Oscillatorer med hög kvalitetsfaktor andvänds ofta vid mätningar av väldigt små krafter då de har en ökad känslighet i ett smalt frekvensband kring resonansfrekvensen. Krafter med frekvenskomponenter utanför detta frekvensband kan ofta inte mätas, varpå den den totala kraften som verkar på oscillatorn förblir okänd. I denna avhandling presenterar vi metoder för att effektivt utnyttja det tillgängliga frekvensbandet kring resonans till att rekonstruera krafter från ett partiellt frekvensspektrum.

Vi tillämpar metoderna på dynamisk atomkraftsmikroskopi (AFM) där en spets i änden av en mikrometerstor balk oscillerar nära en yta som ska undersökas. Genom att rekonstruera kraften mellan spetsen och ytan kan flera egenskaper hos ytan härledas. Detta står i kontrast med vanlig AFM där bara en av de många frekvenskomponenterna av den tidsberoende kraften kan mätas och bara kvalitativa slutsatser om ytan kan dras.

För att öka antalet mätbara frekvenskomponenter har vi utvecklat Intermodulations AFM (ImAFM). ImAFM utnyttjar att en drivsignal med flera frekvenser genom frekvensmixning kommer ge upphov till flera nya frekvenser som en reaktion på den icke-linjära interaktionen mellan spetsen och ytan. Intermodulations AFM, amplitud-modulerad AFM och frekvens-modulerad AFM kan alla ses som specialfall av smalbandigt AFM, där spetsens rörelse kan beskrivas med en snabbt oscillerande del och en långsamt varierande envelopp. Genom att använda ett koncept av kraft-kvadranter kan varje snabb oscillationscykel analyseras och ImAFM-mätningen kan tolkas som en snabb mätning av kraft-kvadranternas beroende på oscillationsamplituden eller frekvensen. För att utforska gränserna för denna beskrivning av kraften introducerar vi en kraft-skiva, vilket motsvarar den fulla beskrivningen av kraften i smalbandigt AFM.

Vi presenterar en metod för att rekonstruera kraften som ett polynom. Denna kraftrekonstruktion är en linjär approximativ rekonstruktions-metod i vilket målet är att hitta de parametrar av en modellfunktion som bäst motsvarar den riktiga kraften mellan spettsen och ytan. En annan klass av rekonstruktions-metoder är intergral-metoder som ämnar att invertera integrlekvationen mellan kraften och den uppmätta signalen. Vi presenterar en sådan integral-metod, amplitud-beroende kraft spektroskopi (ADFS), som rekonstruerar den konservativa delen av kraften. Tillsammans med ImAFM använder vi ADFS för att kombinera hög-upplöst AFM vid hög hastighet med noggranna kraftmätningar i varje bildpunkt av AFM-bilden. Vi diskuterar också hur metoder från tomografi kan utnyttjas för att rekonstruera dissipativa krafter som funktion av både position och hastighet.

Metoderna som är framtagna i denna avhandling är inte begränsade till bara AFM utan är beskrivna i en generell kontext av harmoniska oscillatorer med extern kraftpåverkan. Vi hoppas att dessa metoder bidrar till att omforma AFM från ett kvalitativt verktyg till ett kvantitativt kraftmikroskop och att den även kan användas i andra tillämpningar med hög-kvalitativa oscillatorer.

Contents

Abstract i

Sammanfatting ii

Contents iii

I Introduction 1

1 Measurements with the harmonic oscillators 3
1.1 Oscillations and their application . . . 3
1.2 The harmonic oscillator . . . 4
1.3 Noise and sensitivity of the harmonic oscillator . . . 8

2 Atomic force microscopy 13
2.1 The physics of cantilever-based detection . . . 13
2.2 Imaging and force measurements . . . 17
2.3 Multifrequency AFM . . . 19

3 Intermodulation atomic force microscopy 23
3.1 Nonlinear systems and atomic force microscopy . . . 23
3.2 IMP measurement and Fourier leakage . . . 27
3.3 IMP phase measurements . . . 31
3.4 Measurement time and the resonant detection band . . . 34
3.5 FPGA-based measurements . . . 35
3.6 Intermodulation AFM Software Suite . . . 37
3.7 Experimental results . . . 38
3.7.1 ImAFM approach measurements . . . 39
3.7.2 ImAFM imaging . . . 42

4 Interpreting narrow-band AFM 47
4.1 Motion and force . . . 47
4.2 Force representation and limits of blind force reconstruction . . . 49

4.3 Single cycle time domain analysis 51

5 Force reconstruction methods **55**
5.1 Approximative reconstruction methods 55
5.1.1 Linear approximative methods 56
5.1.2 Nonlinear approximative methods 59
5.2 Integral reconstruction methods 60
5.2.1 Amplitude-dependence force spectroscopy 60
5.2.2 Atomic force tomography 62

6 Conclusions and outlook **69**

Bibliography **71**

Appendix **81**
A.1 Fabrication of the PS/PMMA blend sample 81
A.2 The double Abel transform 81
A.3 Derivations of the atomic force tomography equations 82

Acknowledgments **85**

II Papers **87**

"An jeder Sache etwas zu sehen suchen, was noch niemand gesehen und was noch niemand gedacht hat."

(To seek in everything something to see, which has never before been seen nor sought.)

Georg Christoph Lichtenberg (1742-1799)
German mathematican and first professor
for experimental physics in Germany

Part I

Introduction

Chapter 1

Measurements with the harmonic oscillators

1.1 Oscillations and their application

The word "oscillation" has its roots in the Latin word "oscillatio" which literally means "swing"[1]. An oscillating system or oscillator is a dynamical system which swings, or oscillates, between two more more states as time passes. If the system returns to every state in a regular time interval the oscillations are called periodic and the length of the regular interval defines the period of the oscillation. Oscillating systems can be found everywhere in nature and society. Examples include the motion of the planets around the sun[2], rhythmic activity in the central nervous system[3], business cycles in economic activity[4, 5], chemical reactions[6, 7] or the change of a neutrino flavor[8]. Because of the frequent appearance of oscillations in nature some non-western cultures even think of time as a periodic oscillating process (wheel of time) instead of a linear time bar[9]. In science and engineering oscillators are among the most-studied systems.

A class of oscillators that played an important role in the development of science are mechanical oscillators, where a discrete or distributed mass oscillates around an equilibrium position. As mechanical systems can be easily built and be readily studied experimentally, they are among the first to be systematically studied and they have been used in a variety of artistic and engineering applications.

An enormous variety of mechanical resonators can be found in music. Every string or drum-based instrument exploits a oscillating string or membrane and the sound of each instrument depends on the details of the used oscillator. Even flutes can be considered as mechanical oscillators where pressure oscillations in a shallow cavity is driven by a stream of air.

One of the most common engineering examples of a mechanical oscillator is the pendulum which is a freely swinging mass suspended from a pivot point. Galileo Galilei observed experimentally that the period of a freely swinging pendulum is

independent of its oscillation amplitude[10]. This observation introduced counting the number of oscillation cycles of a swinging pendulum as the basic principle for the measurement of time for hundreds of years. An increasingly accurate measurement of time was required for marine navigation very sophisticated clocks based on pendula were constructed. Since pendulum clocks are very sensitive to perturbations from the environment, different oscillators like balance wheels have been invented. Nowadays, the most accurate clocks are based on counting oscillation cycles in quantum mechanical mechanical systems, transitions between different atomic energy levels serve as the basis of time measurements[11]. Not only time can be measured with pendula. Jean Bernard Foucault used a simple pendulum to demonstrate the rotation of the earth around its north-south axis.

In recent years the advancement of miniaturization technology allows the fabrication of micro- and nanomechanical oscillators on a industrial scale. Though, usually not noticeable in our everyday life, these systems can be found as tuning forks in clocks, accelerometers in cars, or gyroscopes in mobile phones. At the forefront of research new mechanical systems like carbon nanotubes are studied to achieve higher oscillation frequencies[12]. Micro-mechanical oscillators have been the first macroscopic objects which haven been cooled to their quantum mechanical ground state using methods form laser physics[13, 14]. In the field of ultrasensitive detection mechanical resonators are used for biomedical applications like cancer diagnosis[15] and for pushing the sensitivity limits of weight measurement down to the detection of single protons[16]. The scientific sensing application with probably the most wide-spread use of a mechanical oscillator is dynamic atomic force microscopy (AFM) in which an cantilever beam oscillates close to a sample surface[17].

In AFM and in many other sensing applications one is interested in detecting external forces acting on the oscillator. In this thesis we present general methods for reconstructing these external forces and we apply the methods to AFM. However, since the oscillator is modeled as a general linear system we expect use of the methods in other measurements which are based on perturbing an oscillation, or resonance.

1.2 The harmonic oscillator

The simplest model which exhibits oscillating behaviour is a point mass particle subject to a linear restoring force, e.g. the force of a linear spring. For this system Newton's second law becomes

$$m\ddot{z} + kz = 0 \tag{1.1}$$

where $z = z(t)$ is the particle's position as a function of time t, m is the particle mass, k is the so-called spring constant and the dot denotes differentiation with respect to time. The solution to this linear ordinary differential equation is

$$z(t) = A\cos(\omega_0 t + \phi) \tag{1.2}$$

where $\omega_0 = \sqrt{k/m}$. For the initial conditions $z(0) = z_0$ and $\dot{z}(0) = v_0$ the amplitude A and phase ϕ are given by

$$A = \sqrt{z_0^2 + (v_0/\omega_0)^2}, \tag{1.3}$$

$$\tan(\phi) = \frac{v_0/\omega_0}{z_0}. \tag{1.4}$$

Due to this harmonic motion of the particle as shown in figure 1.1a the system described by equation (1.1) is called harmonic oscillator.

The harmonic oscillator model is one of the most important models in physics since it naturally arises for a particle in a bound potential U. If the equilibrium position of the particle is at $z_0 = 0$ the potential can be Taylor expanded for small deflections around $z_0 = 0$. The force F on the particle is then given by

$$F(z) = -\left.\frac{dU}{dz}\right|_{z=0} + \left.\frac{d^2U}{dz^2}\right|_{z=0} z + \mathcal{O}\left(z^2\right) \tag{1.5}$$

The first term vanishes as $z_0 = 0$ is the equilibrium position and if we identify

$$\left.\frac{d^2U}{dz^2}\right|_{z=0} = k \tag{1.6}$$

we readily obtain equation (1.1) as the first-order approximation to the equation of motion.

However, dissipative forces which cannot be represented by a potential function are also often present in oscillating systems. For small velocities these frictional forces can be described as

$$F_{\text{dis}} = -m\gamma\dot{z} \tag{1.7}$$

where γ is the damping coefficient. With this additional force the system is called the damped harmonic oscillator and the equation of motion becomes

$$m\ddot{z} + m\gamma\dot{z} + kz = 0 \tag{1.8}$$

which has the solution

$$z(t) = Ae^{-\lambda_\pm t + \phi} \tag{1.9}$$

where the amplitude A and phase ϕ are determined from the initial conditions. The exponent $\lambda_\pm$ is given by

$$\lambda_\pm = \frac{1}{2}\gamma \pm \sqrt{\frac{\gamma^2}{4} - \omega_0^2} \tag{1.10}$$

and it determines the qualitative behaviour of the solution as depicted in figure (1.1)b.

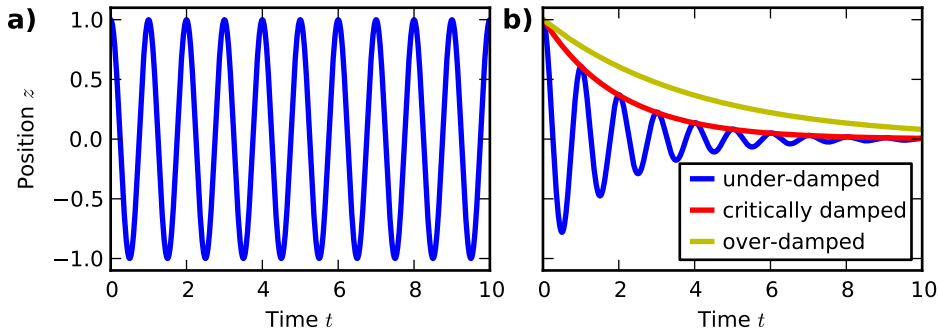

Figure 1.1: Motion of an un-damped (a) and a damped harmonic oscillator (b). The damped harmonic oscillator exhibits three qualitatively different types of motion. The under-damped motion is an oscillating motion with exponentially decreasing amplitude. As the damping constant increases the oscillating component becomes smaller and vanishes completely for the critically damped oscillator for which the oscillator returns to its equilibrium position on a exponential trajectory. For higher damping coefficients the oscillator is over-damped and exponentially approaches its equilibrium position. However, there one of the solutions for the over-damped harmonic oscillator has a longer decay time as as in the critically damped case.

- For $\gamma^2/4 < \omega_0^2$ the system is called under-damped and the solution exhibits an oscillating term with an exponential decay,

$$z(t) = Ae^{-\gamma/2t}\cos\left(\sqrt{\omega_0^2 - \frac{\gamma^2}{4}} + \phi\right) \tag{1.11}$$

- For $\gamma^2/4 = \omega_0^2$ the system is called critically damped and the solution becomes

$$z(t) = Ae^{-\gamma/2t+\phi} \tag{1.12}$$

- For $\gamma^2/4 > \omega_0^2$ the system is over-damped with the solutions

$$z(t) = Ae^{-\left(\frac{\gamma}{2}\pm\sqrt{\frac{\gamma^2}{4}-\omega_0^2}\right)t} \tag{1.13}$$

  of which one decays faster and the other one slower than the critically damped case.

The damping constant γ can be equivalently described in terms of a quality factor

$$Q = \frac{\omega_0}{\gamma}. \tag{1.14}$$

The quality factor is a measure of the energy which is lost by the oscillator to the environment in each cycle of a sinusoidal oscillation,

$$E_{\text{dis}} = 2\pi \frac{E_{\text{stored}}}{Q} \tag{1.15}$$

where E_{stored} is the energy initially stored in the oscillator. In what follows the quality factor is used instead of the damping constant.

When simple forces as those defined in equations (1.5) and (1.7) cause such rich behaviour of the system, one would expect that more general forces are even more difficult to understand. However, additional external drive force which can be considered as a function of time can be treated quite simply. In this case the system is called driven damped harmonic oscillator and the the equation of motion is

$$m\ddot{z} + m\frac{\omega_0}{Q}\dot{z} + kz = F(t) \tag{1.16}$$

Since equation (1.16) is linear in z the general solution is a linear superposition of harmonic oscillations at different frequencies. Such motion is naturally best analyzed using the Fourier transform.

The Fourier transform is based in the idea of representing a function as a superposition of harmonic functions as introduced by Joseph Fourier[18]. Generally, the Fourier transform $\mathcal{F}\{f\} = \hat{f}$ of a function $f : \mathbb{R} \to \mathbb{C}$ which is Lebesgue-integrable is defined as

$$\mathcal{F}\{f\}(\omega) = \hat{f}(\omega) = \frac{1}{2\pi}\int_{-\infty}^{\infty} f(t)e^{-i\omega t}dt \tag{1.17}$$

where i is the complex unit and ω is the angular frequency. Often $\hat{f}$ is called the representation of f in Fourier space or in the frequency domain while the domain of the original function f is called the time domain. The Fourier transform $\mathcal{F}$ has a unique inverse $\mathcal{F}^{-1}$ which is given by

$$\mathcal{F}^{-1}\left\{\hat{f}\right\}(t) = \int_{-\infty}^{\infty} \hat{f}(\omega)e^{i\omega t}d\omega \tag{1.18}$$

such that $\mathcal{F}^{-1}\{\mathcal{F}\{f\}\} = f$.

Using the definition of the Fourier transform equation (1.17) in the Fourier domain becomes

$$-m\omega^2\hat{z} + im\frac{\omega_0\omega}{Q}\hat{z} + k\hat{z} = \hat{F} \tag{1.19}$$

where $\hat{z}$ and $\hat{F}$ are the Fourier transforms of z and F respectively. Thus, the motion of a particle subject to an external drive force can simply be computed in Fourier space as

$$\hat{x} = \hat{\chi}\hat{F} \tag{1.20}$$

where

$$\hat{\chi} = \hat{\chi}(\omega) = \frac{\omega_0^2/k}{\omega^2 - \omega_0^2 + i\frac{\omega_0\omega}{Q}} \tag{1.21}$$

is the linear response function of the driven damped harmonic oscillator. The linear response function is linear in that sense that if $\hat{z}_1$ and $\hat{z}_2$ are solutions to equation (1.16) for two different drive forces $\hat{F}_1$ and $\hat{F}_2$ then $\lambda_1\hat{z}_1+\lambda_2\hat{z}_2$ is the solution to the drive force $\lambda_1\hat{F}_1+\lambda_2\hat{F}_2$. The function $\hat{\chi}$ is complex-valued and has a simple physical interpretation. For a single-frequency excitation of the form $F(t) = F_0\cos(\bar{\omega}t)$ the resulting motion is $z(t) = A\cos(\bar{\omega}t+\phi)$ where the amplitude A is given by

$$A(\bar{\omega}) = |\hat{\chi}(\bar{\omega})|\, F_0 \tag{1.22}$$

and the phase-lag ϕ between excitation and response by

$$\phi(\bar{\omega}) = \arg\left(\hat{\chi}(\bar{\omega})\right). \tag{1.23}$$

Figure 1.2a shows a plot of $|\hat{\chi}|$ as a function of the normalized frequency $\Omega = \omega/\omega_0$ for a quality factor of $Q = 500$. The amplitude $|\hat{\chi}|$ exhibits a sharp peak with a maximum at

$$\omega_{\max} \approx \omega_0 \tag{1.24}$$

which is called the resonance peak with a resonance frequency of ω_0. The existence of a resonance (peak) implies that there is a distinct frequency band in which small drive forces result in particle motion with big amplitudes. On the other hand, forces of equal strength far above the resonance frequency do not cause significant motion as the linear transfer function $\hat{\chi}$ decreases as $1/\omega^2$ and thus attenuates forces at higher frequencies.

The phase-lag ϕ in figure 1.2b exhibits similar behaviour. In the frequency band close to the resonance frequency the phase-lag ϕ is very responsive to small frequency changes of the excitation force. Away from resonance frequency the phase lag is approximately constant, being 0 below the resonance and $-\pi$ above the resonance.

The strength of the resonance depends on the quality factor Q. In figure 1.3 the amplitude and phase functions of the linear response function $\hat{\chi}$ are plotted close to $\Omega = 1$ for different values of Q. For higher values of Q the response amplitude A is higher and the phase ϕ changes more rapidly around $\Omega = 1$ where equals $-\pi/2$ independent of Q and k. In contrast, the amplitude A on resonance ($\Omega = 1$) is given by $A(\Omega = 1) = Q/k$.

1.3 Noise and sensitivity of the harmonic oscillator

The accurate measurement of different physical signals is at the heart of many scientific and engineering applications. Here, "accurate" means that the noise which is always present in any physical measurement should be much smaller than the signal of interest, or the signal-to-noise ratio (SNR) should be large. To optimize the accuracy of a measurement often the principle of resonant detection is used which is based on the idea of coupling a high quality factor harmonic oscillator to the experimental system such that the signal of interest can be considered as

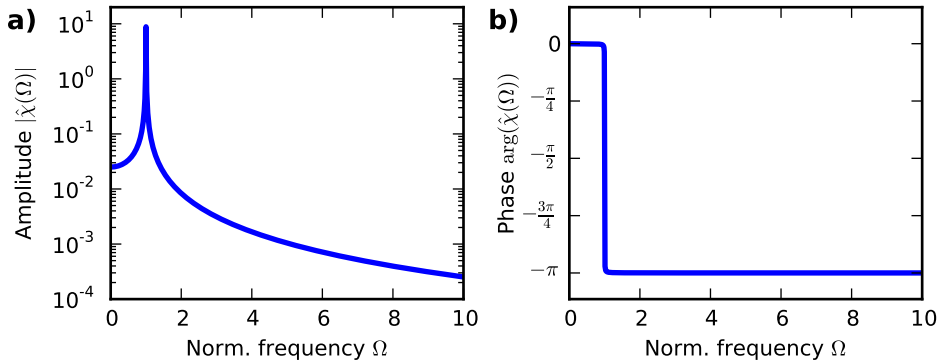

Figure 1.2: Amplitude (a) and phase (b) of the linear response function of a driven damped harmonic oscillator with $Q = 500$ and $k = 40$ Nm^{-1}.

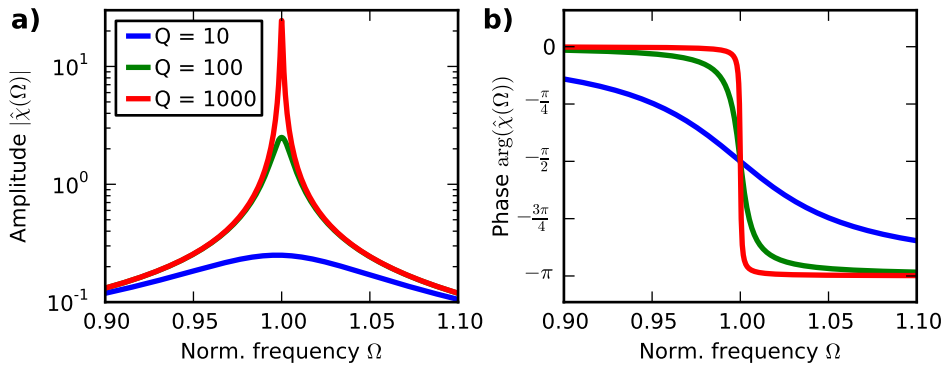

Figure 1.3: Amplitude (a) and phase (b) of the linear response function of a driven damped harmonic oscillator with $k = 40$ Nm^{-1} for different values of Q.

a time-dependent force acting on the oscillator. Inverting equation (1.20), we see that the force signal can easily be determined in Fourier space by measurement of the Fourier transform of the oscillator motion,

$$\hat{F}(\omega) = \hat{\chi}^{-1}(\omega)\hat{z}(\omega) \tag{1.25}$$

The fact that a measurement of the force requires a measurement of the oscillator's motion implies that both position and force noise contribute to the total noise in the measurement. To quantitatively analyze the noise we consider the power spectral density (PSD) of the oscillator position $\hat{S}_{zz}$ and of the force acting on the

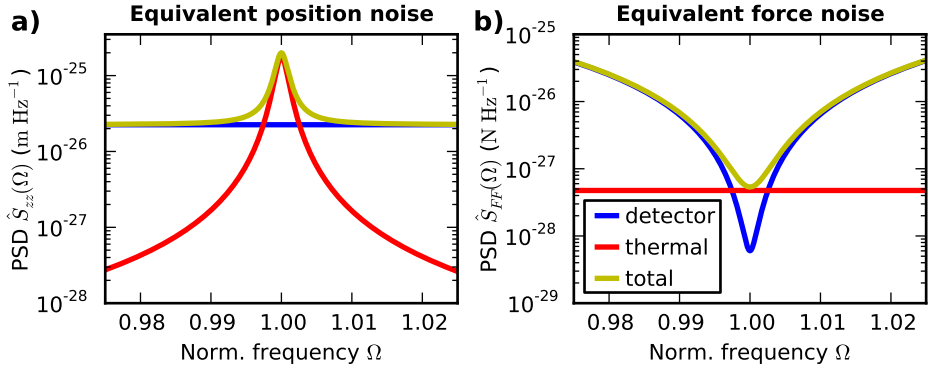

Figure 1.4: The power spectral density of detector noise, thermal noise and their sum close to resonance shown in the position (a) and force representation (b). The detection noise floor of $A_{\mathrm{det}} = 150.0 \times 10^{-15}$ m Hz^{-2}, the thermal noise of $F_{\mathrm{th}} = 21.8 \times 10^{-15}$ N Hz^{-1} and the oscillator parameters $Q = 514.0$ and $k = 26.6$ Nm^{-1} are taken from experimental data for a micro-cantilever oscillating in air at room temperature.

oscillator $\hat{S}_{FF}$ in the absence of an external drive force. They are defined as

$$\hat{S}_{zz}(\omega) = 2\pi \quad \hat{z}^*(\omega)\hat{z}(\omega) \tag{1.26}$$
$$\hat{S}_{FF}(\omega) = 2\pi \quad \hat{F}^*(\omega)\hat{F}(\omega) \tag{1.27}$$

where the star denotes complex conjugation. For a measurement of the oscillator position one source of noise is the detection system, like electronic noise in the measurement circuit. This detector noise can often be treated as white noise which is a frequency-independent noise background in the position PSD $\hat{S}_{zz}$ as shown in figure 1.4a. Plotted as an noise equivalent noise force PSD $\hat{S}_{FF}$, the corresponding noise background has a frequency-dependence give by $\hat{\chi}^{-1}$ and exhibits a minimum at the resonance frequency.

Another significant source of noise is the so-called thermal noise which has a deeper physical origin. For a real physical implementation of a harmonic oscillator not only conservative forces but also dissipative forces are present which might be due to internal friction or the coupling to a dissipative environment environment. Dissipative forces are always accompanied by fluctuation forces. A simple example for this relation was discussed by Albert Einstein[19]. He realized that the drag forces on a particle pulled through a viscous fluid are the same forces that cause Brownian motion of the particle when there is no external force pulling the particle.

This observation is formalized by the fluctuation dissipation theorem[20]. The mean square displacement $\langle(\Delta z)^2\rangle$ around the average value $\langle z(t)\rangle$ of a system can

be calculated from the position PSD $\hat{S}_{zz}$ as

$$\left\langle (\Delta z)^2 \right\rangle = \int_0^\infty \hat{S}_{zz}(\omega) d\omega. \tag{1.28}$$

The fluctuation-dissipation theorem connects the position PSD $\hat{S}_{zz}$ with the imaginary part of the linear response function $\hat{\chi}$ such that

$$\hat{S}_{zz} = \frac{2k_B T_{\text{bath}}}{\omega} \text{Im}\left(\hat{\chi}(\omega)\right) \tag{1.29}$$

allowing for a calculation of the position fluctuations from knowledge of the linear response function $\hat{\chi}$ together with the Boltzmann constant k_B and the temperature T_{bath} of the surrounding heat bath. For the harmonic oscillator the position PSD becomes

$$\hat{S}_{zz}(\omega) = k_B T_{\text{bath}} \frac{\omega_0^3/Qk}{\left(\omega_0^2 - \omega^2\right)^2 + \left(\frac{\omega_0 \omega}{Q}\right)^2}. \tag{1.30}$$

This position PSD can be interpreted as the system's response to a frequency-independent fluctuation force which can be determined as

$$F_{\text{th}} = \sqrt{\frac{k_B T_{\text{bath}}}{Q\omega_0}}. \tag{1.31}$$

Since this fluctuation force is derived from equilibrium thermodynamics it is often called thermal noise force. Thermal noise and detector noise are dual to each other in the sense that detector noise is frequency-independent in the position PSD while thermal noise is frequency-independent in the force PSD. For both the position and the force PSD thermal noise dominates in the region close to resonance in figure 1.4. In this region a measurement can be performed at the fundamental noise limit since the detection noise might be reduced by for example using better measurement electronics whereas the thermal noise is intrinsic to the oscillator and its environment.

The important figure of merit for a measurement is the SNR which is defined as

$$\text{SNR} = \frac{P_{\text{signal}}}{P_{\text{noise}}} \tag{1.32}$$

where P_{signal} is the power in the desired signal and P_{noise} is the total noise power. For a given measurement bandwidth B (inverse of the measurement time T) the signal power at SNR = 1 defines the minimum detectable force F_{min} giving a measure for the system sensitivity at the specified bandwidth B. Please note that the system sensitivity is often confused with the system responsivity which is simply the input-output conversion factor of the system given by the absolute value of the linear response function $\hat{\chi}$. Figure 1.5 shows the minimum detectable force for typical AFM parameters. The minimum detectable force exhibits a minimum at the

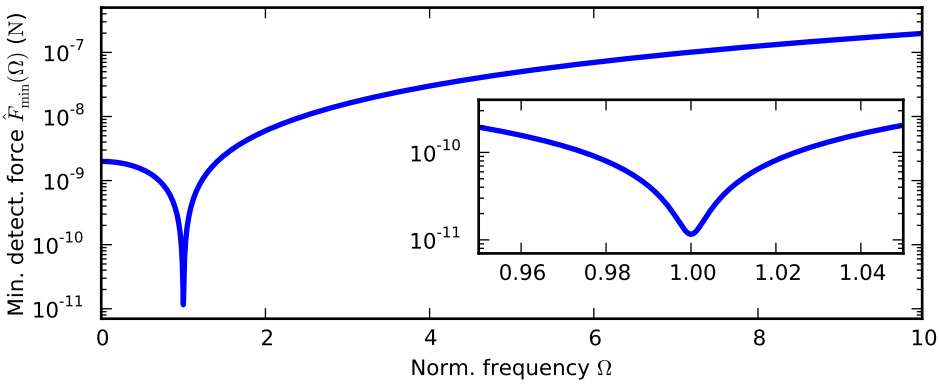

Figure 1.5: The smallest measurable force for a measurement bandwidth of $B = 500$ Hz. The noise and oscillator parameters are the same as for figure 1.4. The the minimum in the smallest measurable force is narrow on a broad frequency scale. However, as shown in the inset the minimum has a finite width allowing for very sensitive measurements in a narrow frequency band around resonance.

resonance frequency and increases at higher frequencies while it is nearly constant at frequencies lower than the resonance frequency. The very narrow minimum means that a high-Q oscillator oscillator is not good for measurement of forces with a broad-band spectrum. However, in the narrow band around resonance an optimal choice of the oscillator parameters ω_0, k and Q allows to for extremely sensitivity in a narrow band.

Chapter 2

Atomic force microscopy

2.1 The physics of cantilever-based detection

One example of the use of harmonic oscillators in measurements is atomic force microscopy (AFM)[21] which is a common tool in nanotechnology to image[22, 23, 24], measure[25, 26] and manipulate[27, 28, 29] matter on surfaces. At the heart of AFM is a micro-cantilever which is clamped at one end and free at the other end as depicted in figure 2.1. At the free end a small tip is attached whose position is usually measured with an optical lever system. The cantilever's tip interacts with the surface through many different types of forces such as dispersion forces, mechanical forces, electro-static forces, chemical forces, magnetic forces etc. hence the versatility of AFM. To externally control the interaction between the tip and the surface the cantilever can be positioned with sub-nanometer resolution in all three directions above the sample surface using a piezo-electric nano-positioning system. An additional piezo shaker can excite cantilever oscillations.

The cantilever is usually modeled as a one-dimensional continuum object using Euler-Bernoulli beam theory[30]. In this theory the deflection w of an beam element at position x along a cantilever of length L at time t, is governed by the equation

$$EI\frac{\partial^4 w(x,t)}{\partial x^4} + \mu\frac{\partial^2 w(x,t)}{\partial t^2} = F\left(x, w(x,t), t\right) \tag{2.1}$$

where E is the Young's modulus of the cantilever, I is the second moment of area and μ is the mass per unit area. We require that the general solution to equation (2.1) is a linear superposition of different oscillation modes which are separable in space and time such that

$$w(x,t) = \sum_{n=1}^{\infty} d^{(n)}(t)\Phi^{(n)}(x) \tag{2.2}$$

where the $d^{(n)}$ describe the mode dynamics and the $\Phi^{(n)}$ are the so-called mode shapes which can be obtained from equation (2.1) in the absence of an external

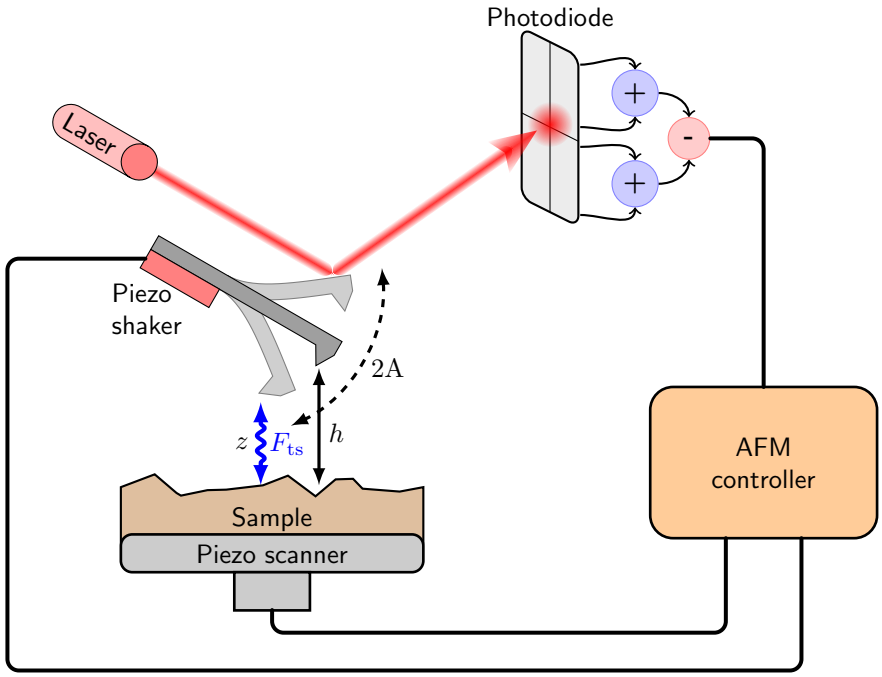

Figure 2.1: In a dynamic AFM tip at the end of a cantilever beam interacts with the surface through the tip-sample force F_{ts} while it oscillates with the amplitude A. In the absence of the tip-surface force and any drive force exerted by piezo shaker the tip is at rest at the static probe height h. The tip position is measured using a laser-based optical lever system. The photodiode is connected to the AFM controller electronics which additionally generates the voltages for the piezo shaker driving the cantilever and the piezo scanner adjusting the position of the cantilever with respect to the sample.

excitation force,

$$\frac{\partial^4 \Phi^{(n)}(x)}{\partial x^4} - \kappa^{(n)} \Phi(x) = 0 \tag{2.3}$$

where

$$\kappa^{(n)} = \frac{\left(\omega_0^{(n)}\right)^2 \mu L^4}{EI} \tag{2.4}$$

determines $\omega_0^{(n)}$ the resonance frequency of the n^{th} mode. For a cantilever beam which is clamped at one end and free at the other end the boundary conditions are

$$\Phi^{(n)}(0) = 0, \tag{2.5}$$

$$\left.\frac{\partial \Phi^{(n)}(x)}{\partial x}\right|_{x=0} = 0, \tag{2.6}$$

$$\left.\frac{\partial^2 \Phi^{(n)}(x)}{\partial x^2}\right|_{x=L} = 0, \tag{2.7}$$

$$\left.\frac{\partial^3 \Phi^{(n)}(x)}{\partial x^3}\right|_{x=L} = 0 \tag{2.8}$$

and the solution to equation (2.3) becomes

$$\begin{aligned} \Phi^{(n)}(x) = & \cos\left(\kappa^{(n)} x/L\right) - \cosh\left(\kappa^{(n)} x/L\right) \\ & - \frac{\cos\left(\kappa^{(n)}\right) + \cosh\left(\kappa^{(n)}\right)}{\sin\left(\kappa^{(n)}\right) + \sinh\left(\kappa^{(n)}\right)} \\ & \times \left(\sin\left(\kappa^{(n)} x/L\right) - \sinh\left(\kappa^{(n)} x/L\right)\right) \end{aligned} \tag{2.9}$$

where κ_n is obtained numerically from the characteristic equation

$$1 + \cos\left(\kappa^{(n)}\right) \cosh\left(\kappa^{(n)}\right) = 0 \tag{2.10}$$

The resonance frequencies $\omega_0^{(n)}$ obtained from equation (2.4) and some corresponding mode shapes are shown in figure 2.2 and 2.3 respectively. In contrast to the resonance frequencies of a vibrating string, the resonance frequencies of a cantilever beam clamped at one end and free at the other end do not scale linearly with the mode number n.

The dynamics of the different modes depend on the forces which act on the tip. In dynamic AFM the cantilever is externally excited by either shaking the clamped end or using a magnetic drive scheme. This external drive force is often model as an effective drive force which acts only at the free end of the cantilever. In conventional AFM, only the first cantilever mode is excited and thus the cantilever deflection can be approximated as

$$w(x,t) \approx q^{(1)}(t) \Phi^{(1)}(x) \tag{2.11}$$

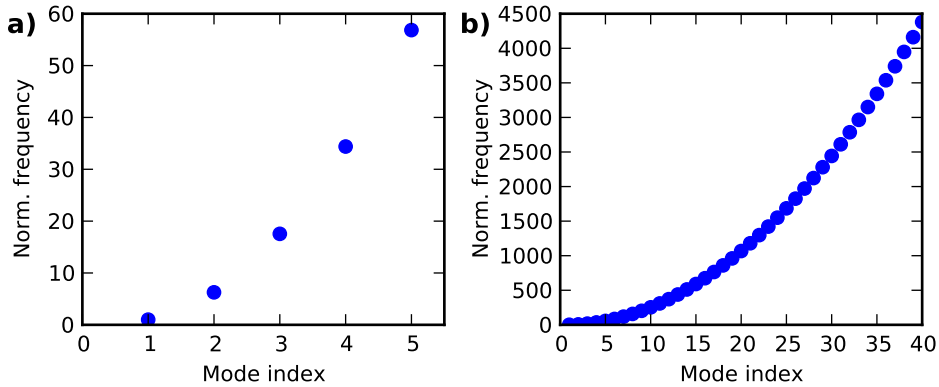

Figure 2.2: The resonance frequency as a function of the mode index for the first six modes (a) and the first 40 modes (b).

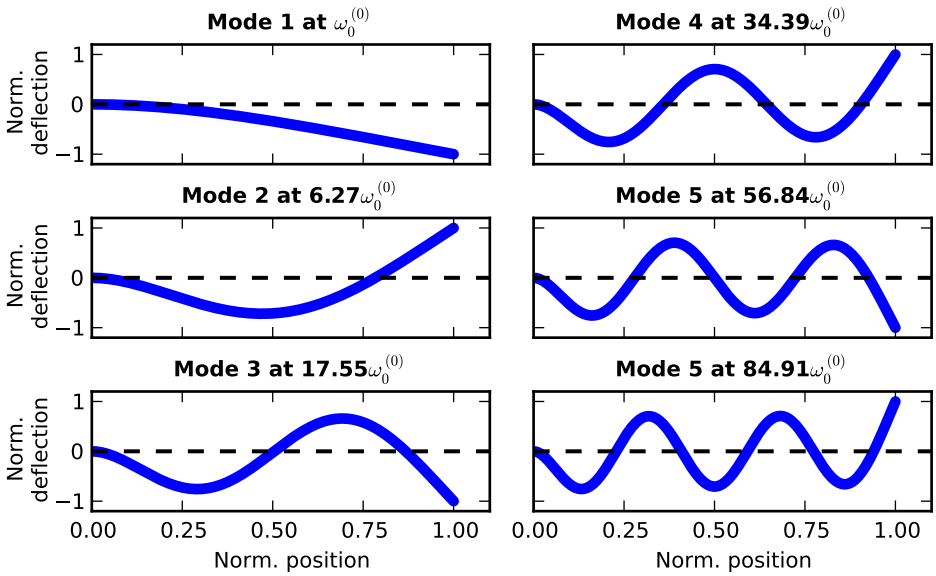

Figure 2.3: Mode shapes for first six modes of a cantilever clamped at the left end and free at the right end.

Moreover, it is assumed that close to the surface only the tip at the end interacts with the sample surface and a heuristic damping term is added to account for the fact that the cantilever is surrounded by a viscous fluid (air or liquids)[31]. With these assumptions about the forces acting on the cantilever the equation of motion describing the time-dependence of the beam deflection can be written as[32, 33]

$$\ddot{d} + \frac{\omega_0}{Q}\dot{d} + kd = F_{\mathrm{drive}}(t) + F_{\mathrm{ts}}(t) \tag{2.12}$$

where we dropped the mode index. The resonance frequency ω_0 and the spring constant k are determined by properties of the cantilever beam and the quality factor Q is due to the tip motion in a viscous fluid. Equation (2.12) reveals that the basic physics of AFM is the physics of a driven damped harmonic oscillator which is subject to an unknown tip-surface force F_{ts}.

2.2 Imaging and force measurements

When imaging a surface the tip is laterally scanned above the sample surface while a feedback mechanism adjusts the static probe height above the surface to generate an image of the surface topography. The feedback mechanism is usually based on a simple proportional-integral controller (PI loop) which attempts to keep the value of an measured physical quantity constant during the scan.

In the so-called quasi-static or contact imaging mode, this physical quantity is the tip deflection d from the equilibrium position. In this mode the tip is always in mechanical contact with the surface and equation (2.12) reduces to

$$kd = F_{\mathrm{ts}} \tag{2.13}$$

where F_{ts} is constant. However, one should note that both the static mode shape and the static spring constant differ slightly from the mode shape and the spring constants derived using the boundary conditions (2.5) - (2.8). One particular problem with quasi-static imaging is that the tip is in constant contact with the surface and the imaging force can damage the sample surface.

This problem of strong back action forces on the sample can be circumvented using dynamic imaging modes. In dynamic imaging the tip is sinusoidally excited and therefore oscillates above the sample surface such that the force on the tip varies during one oscillation cycle.

The most wide-spread dynamic imaging modes are amplitude-modulated AFM (AM-AFM) and frequency modulated AFM (FM-AFM). In AM-AFM both the strength and the frequency of the external excitation are fixed. The resulting tip motion close to the surface is approximately sinusoidal and given by[34]

$$z(t) = A\cos(\bar{\omega}t + \varphi) + h \tag{2.14}$$

where $\bar{\omega}$ is the excitation frequency and h is the static probe height above the surface as illustrated in figure 2.1. The oscillation amplitude A and the phase

lag φ between the excitation signal and the tip motion are the measured physical quantities and A is used as the input for the feedback loop.

Cantilevers in vacuum have much higher Q factors than in air or in liquids and the tip oscillation amplitude reacts much slower to a change in the tip-surface interaction. To deal with this slow response FM-AFM is often used under vacuum conditions. In FM-AFM an additional feedback loops adjusts the drive frequency such that the cantilever is always excited at the resonance frequency which shifts due to the interaction with the surface[35]. For such an excitation scheme the motion is always $-\pi/2$ out of phase with the excitation signal

$$z(t) = A\cos\left((\omega_0 + \delta\omega)t - \frac{\pi}{2}\right) + h \tag{2.15}$$

where $\delta\omega$ denotes the frequency shift away from the resonance. Often another feedback loop is used to also keep the oscillation amplitude A constant. For such an setup the measured physical quantities are the frequency shift $\delta\omega$ and the excitation strength F_{drive} where $\delta\omega$ is used as the feedback input.

Despite the name atomic "force" microscopy, the tip-surface interaction force above the sample surface remains unknown for both static and dynamic imaging. During static imaging the tip is kept at a constant deflection which is set as a feedback parameter, corresponding to a constant force between the tip and the surface. In contrast, in both AM-AFM and FM-AFM the force on the tip varies during an oscillation cycle. However, since there are only two physical quantities (A and φ or $\delta\omega$ and F_{drive}) only qualitative conclusions about the interaction between the tip and the surface can be drawn. To use AFM for quantitative force measurements different approaches have been developed which are mostly based on measurements of the measured physical quantities at different static tip heights above a single point of the surface.

The simplest force measurement is a measurement of the static deflection d as a function of the tip height h from which equation (2.13) directly reveals the force between the tip and the surface. However, in static measurements the transition region between attractive and repulsive surface forces is often not accessible due to abrupt jumps of the tip towards the surface when the force gradient exceeds the cantilever spring constant[26]. Moreover, forces depending on the tip velocity such as viscous damping forces can not be determined with static measurements.

Dynamic AM-AFM and FM-AFM measurements at different static tip heights h are sensitive to position-dependent damping forces and they do make use of the high signal-to-noise ratio on resonance. However, the measured quantities correspond to weighted averages of the tip-surface force over the oscillation range and thus reconstruction of the tip-surface interaction form experimental data is more complicated than for quasi static fore measurements. For FM-AFM the forces can be obtained by a discretization of the tip-surface force in position[36], by the inversion of a pseudo differential operator for the Laplace transform of the force[37, 38, 39] or in the limit of large oscillation amplitudes[40, 41]. For AM-AFM the situation is more complicated since the oscillation amplitude can be different for different probe

height, which corresponds to a different averaging kernel for each static tip height. Moreover, due to the nonlinear character of the tip-surface interaction, abrupt amplitude changes often occur when changing the static tip height[42, 43]. Up to the first amplitude jump the force can be obtained from the measured oscillation amplitude and phase by the inversion of an integral equation[44]. For the reconstruction in the full measurement region high order polynomial approximations[45], numerical solution of ordinary differential equations[46] or heuristic methods[47] inspired by the pseudo-differential solution for FM-AFM have been put forward. However, these AM-AFM methods either do not have closed form solutions or they are mathematically not well-grounded.

All the force measurement methods discussed above have in common that they are incompatible with imaging at acceptable speeds since they are based on a slow change of the static probe height. With dynamic methods based on FM-AFM and AM-AFM, the data acquired while imaging allow only qualitative analysis of the tip-surface force and the combination of quantitative force measurements with imaging at high spatial and temporal resolution has been a long-standing problem in the development of AFM.

2.3 Multifrequency AFM

The development of dynamic AFM has recently turned toward a new direction called multifrequency AFM[48]. In multifrequency AFM the tip motion comprises more than one single oscillation frequency in contrast conventional single frequency AM-AFM and FM-AFM (compare equations (2.14) and (2.15)). The new frequency components present in the tip motion might be generated by the nonlinear tip-surface force, a multifrequency drive scheme, or booth as depicted in figure 2.4 for different multifrequency methods in.

One of the early discoveries in multifrequency AFM was that the equations (2.14) and (2.15) only approximate the real tip motion and frequencies that are integer multiples of the drive frequencies are also present in the tip motion. These additional frequency components are called higher harmonics and they are generated by the nonlinear tip-surface interaction[49, 50]. Higher harmonics have been used for imaging[51, 52, 53] and a measurement of the complete spectrum of higher harmonics allows for a simple reconstruction of the tip-surface force as a function of time during an tip oscillation cycle[54]. However, the amplitudes of higher harmonics are very small as their frequencies do not coincide with the cantilever's resonance frequencies. Therefore, force measurements using higher harmonics often require strong interaction forces[54], special cantilevers[55, 56] or highly-damped environments[57]. Moreover, the accurate measurement of higher harmonics relies on an accurate calibration of the cantilever's linear response function over a wide frequency band. A wide-band position detector, or a photodiode detector with a high roll-off frequency is also required.

Other multifrequency methods make use of multiple cantilever eigenmodes. In

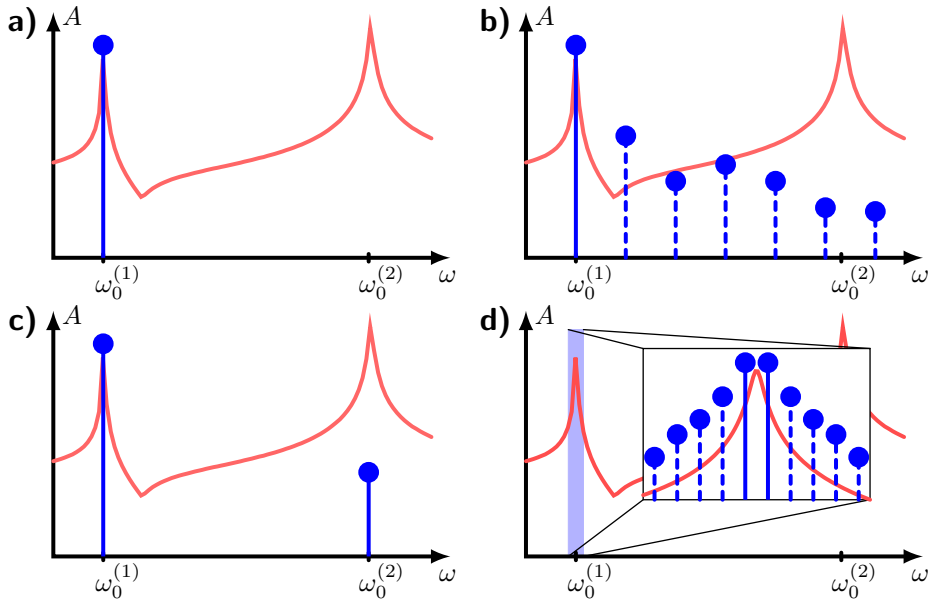

Figure 2.4: Schematics of the tip motion spectrum for conventional AFM (a), bimodal AFM (b), higher harmonics AFM (c) and narrow-band Intermodulation AFM (d). The cantilever is excited at the solid bars while the tip motion is measured at the solid and the dashed bars.

bimodal AFM, the first and the second cantilever resonances are externally excited with two single frequencies at which the tip motion is measured[58, 59, 60, 61, 62, 63, 64]. Bimodal AFM does not allow for quantitative reconstruction of tip-surface forces while scanning, but the amplitude and phase at the second cantilever eigenmode do provide two more measured physical quantities than conventional AM-AFM and FM-AFM. Recently, schemes with a frequency-modulated drive at the second eigenmode[65, 66, 67] and trimodal excitation [68] have been investigated.

Another multifrequency approach is the excitation over a continuous band of frequencies. This so-called band excitation method has been tested for different imaging modes[69, 70]. However, continuous band excitation is not practical in a real experiment with a finite measurement time. As we explain in the following a discrete frequency comb for excitation and measurement is much more advantageous for probing the tip-surface interaction.

Intermodulation AFM (ImAFM) is a method that combines the high information content of measurements at many harmonics with the high signal-to-noise ratio close to a cantilever resonance[71, 72]. In ImAFM, the nonlinear tip-surface force is used to create new frequency components, so-called intermodulation products (IMPs) that occur mixing products of a multifrequency drive. By choos-

ing an appropriate drive scheme a large number of IMPs can be generated close to the first cantilever a resonance for which well-established calibration schemes exist[73, 74, 75, 76]. In the following chapters we will focus on the particular case called narrow-band ImAFM where all of the discrete drive and response frequencies are confined to a narrow band near one resonance. However, one should note that many more drive and measurement schemes with possible in ImAFM, which may also involve multiple eigenmodes.

Chapter 3

Intermodulation atomic force microscopy

3.1 Nonlinear systems and atomic force microscopy

Intermodulation or frequency mixing is a phenomenon that occurs in many physical systems like superconductors[77, 78], optics[79] or matter waves[80] and it is also observed in our daily life in hearing[81, 82, 83] and music[84]. Systems theory can be used for a general mathematical description of intermodulation. A system h is excited or driven with a time-dependent signal $x(t)$ which generates a time-dependent response $y(t)$ at the output port (see figure 3.1).

If the system is linear the spectrum of the response $\hat{y}$ contains the same frequencies as the spectrum of the drive $\hat{x}$. In the simplest case the drive consists of only one pure tone and can be written as

$$x(t) = \cos(\bar{\omega}t) \tag{3.1}$$

for which the response of the linear system is

$$y(t) = g\cos(\bar{\omega}t + \varphi) \tag{3.2}$$

where the amplitude g and the phase φ depend on the actual system h and the drive frequency $\bar{\omega}$ (see figure 3.2).

Figure 3.1: A general system in a block diagram representation. The system has an input at which an time-dependent drive signal $x(t)$ is applied to excite the system. The response to the drive signal $y(t)$ can be measured at the output port.

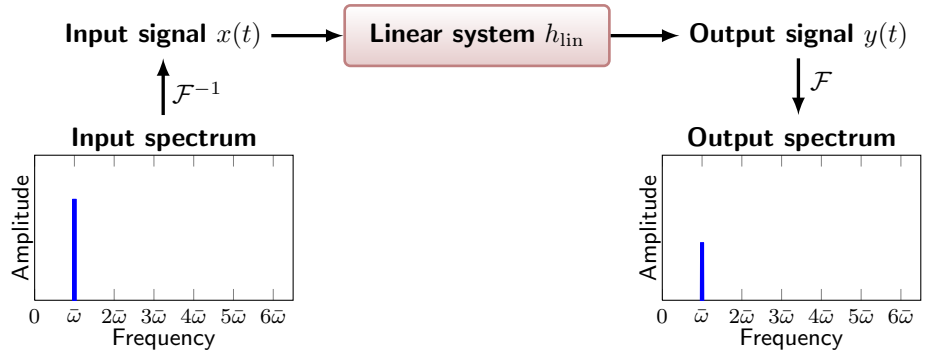

Figure 3.2: A linear system that is driven by a signal with only one pure tone at frequency $\bar{\omega}$ exhibits response only at the drive frequency $\bar{\omega}$.

An example of a nonlinear system is a system whose response can be described by a power series in the input signal,

$$y(x) = \sum_{n=0}^{\infty} g_n x^n. \tag{3.3}$$

Such a system exhibits a more complicated response to the single frequency drive defined in equation (3.1) since the response $y(t)$ contains terms like

$$\begin{aligned} (\cos(\bar{\omega}t))^2 &= \frac{1}{2} + \frac{1}{2}\cos(2\bar{\omega}t), && (3.4)\\ (\cos(\bar{\omega}t))^3 &= \frac{3}{4}\cos(\bar{\omega}t) + \frac{1}{4}\cos(3\bar{\omega}t), && (3.5)\\ &\vdots \end{aligned}$$

revealing the generation of new frequency components in the response spectrum at frequencies that are integer multiples of the drive frequency $\bar{\omega}$. These new frequency components are called harmonics and their amplitudes depend on the polynomial coefficients g_n.

For a drive signal containing two pure tons

$$x(t) = \cos(\omega_1 t) + \cos(\omega_2 t) \tag{3.6}$$

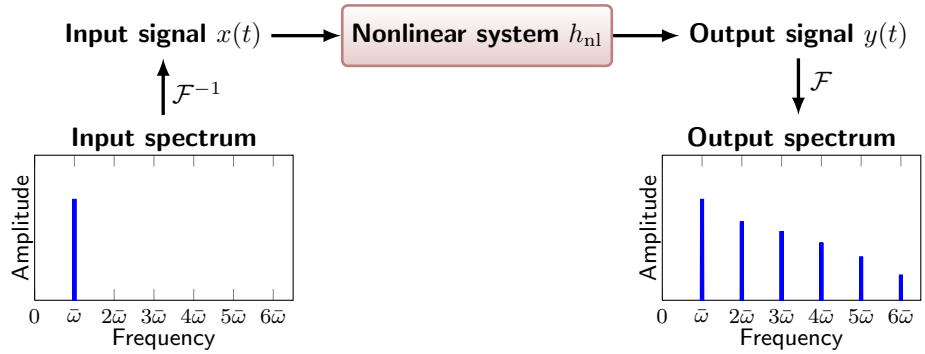

Figure 3.3: If the nonlinear system described by equation (3.3) is driven with one frequency $\bar{\omega}$ the response spectrum has non-zero spectral components at integer multiples of the drive frequency which are called harmonics.

the response of the nonlinear system defined by equation (3.3) contains terms like

$$\begin{aligned}
(\cos(\omega_1 t) + \cos(\omega_2 t))^2 &= 1 + \frac{1}{2}\cos(2\omega_1 t) + \frac{1}{2}\cos(2\omega_2 t) \\
&\quad + \cos\left((\omega_1 + \omega_2)t\right) + \cos\left((\omega_1 - \omega_2)t\right) \qquad (3.7) \\
(\cos(\omega_1 t) + \cos(\omega_2 t))^3 &= \frac{9}{4}\cos(\omega_1 t) + \frac{9}{4}\cos(\omega_2 t) \\
&\quad + \frac{1}{4}\cos(3\omega_1 t) + \frac{1}{4}\cos(3\omega_2 t) \\
&\quad + \frac{3}{4}\cos\left((2\omega_1 + \omega_2)t\right) + \frac{3}{4}\cos\left((\omega_1 + 2\omega_2)t\right) \\
&\quad + \frac{3}{4}\cos\left((2\omega_1 - \omega_2)t\right) + \frac{3}{4}\left((\omega_1 - 2\omega_2)t\right) \qquad (3.8) \\
&\vdots
\end{aligned}$$

In addition to the drive frequencies and their harmonics, frequency components in the response occur at at mixing frequencies of the two drive frequencies as depicted in figure3.4. These additional components are called intermodulation products (IMPs) and for a general multifrequency drive

$$x(t) = \cos(\omega_1 t) + \cos(\omega_2 t) + \ldots + \cos(\omega_M t)$$

the frequencies of the IMPs are given by integer linear combinations of the drive frequencies as

$$\omega_{\mathrm{IMP}} = m_1\omega_1 + m_2\omega_2 + \ldots + m_M\omega_M. \qquad (3.9)$$

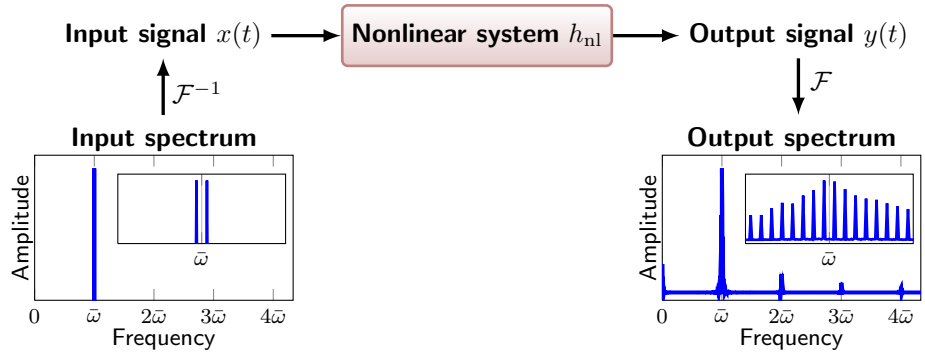

Figure 3.4: If the nonlinear system described by equation (3.3) is excited with two closely tones centered at frequency $\bar{\omega}$ the response spectrum does not only contain harmonics of the drive frequencies but also intermodulation products at frequencies which are integer linear combinations of the drive frequencies. The insets in the input and output spectrum show a zoom of into the region close to $\bar{\omega}$ revealing many IMPs which are all spaced in frequency by the difference between the two drive frequencies.

where $m_1, m_2, \ldots, m_M \in \mathbb{Z}$ and $\omega_1, \omega_2, \ldots, \omega_M$ are the drive frequencies. With equation (3.9) the order $\mathcal{O}_{\mathrm{IMP}}$ of an IMP can be defined as

$$\mathcal{O}_{\mathrm{IMP}} = |m_1| + |m_2| + \ldots + |m_M| \tag{3.10}$$

A nonlinear system might therefore generate a complicated response to a multifrequency drive but the frequencies in the response can be controlled externally by choosing an appropriately designed drive signal.

In intermodulation AFM (ImAFM) this control over the response frequencies is exploited to combine the high information content of AFM methods based on the measurement of higher harmonics with the high signal-to-noise ratio close to a cantilever resonance. From a systems point of view dynamic AFM depicted as in figure 3.5. The nonlinear system is a combination of the nonlinear interaction between tip and surface and the cantilever's linear response function which effectively filters out the response away from the cantilever resonances. In conventional dynamic AFM one cantilever resonance is excited with only one frequency. However, the cantilever's linear response function amplifies all frequencies in a continuous frequency band close to a resonance. To make more efficient use of these frequency bands a special multifrequency drive is applied to the system such that the nonlinear tip-surface force creates intermodulation that is concentrated in the frequency bands close to one or multiple cantilever resonances. In what follows we focus on

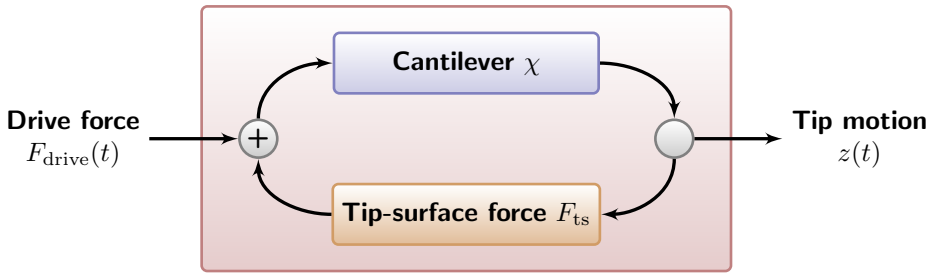

Figure 3.5: In dynamic AFM the drive force is externally applied to the cantilever which forms together with the nonlinear tip-surface force a nonlinear system. The output from the system is the measured tip motion.

the case of narrow-band ImAFM which utilizes only the first flexural cantilever resonance where numerous commercial AFM systems are able to measure the tip motion.

One of most simple drive waveforms used in narrow band ImAFM consists of only two frequencies which are detuned by $\delta\omega$ from the resonance frequency ω_0,

$$F_{\text{dual}}(t) = A_1 \cos\left((\omega_0 - \delta\omega)t\right) + A_2 \cos\left((\omega_0 + \delta\omega)t\right) \tag{3.11}$$

where A_1 and A_2 are the drive strengths. This drive signal corresponds to a beating signal in the time domain with beat frequency $\delta\omega/2$. One disadvantage of of this drive waveform is that only IMPs of odd order are created close to resonance as shown in figure 3.6.

A drive scheme creating both odd and even order IMPs on resonance is given by

$$F_{\text{low,high}}(t) = A_{\text{low}} \cos(\delta\omega t) + A_{\text{high}} \cos(\omega_0 t) \tag{3.12}$$

where $\delta\omega \ll \omega_0$. However, due to the low transfer gain at the low frequency $\delta\omega$ a strong low frequency drive is required which is hard to achieve in a real experiment. Therefore, the dual drive scheme in equation (3.11) is preferable for ImAFM.

3.2 IMP measurement and Fourier leakage

In a real experiment a continuous signal $x(t)$ is samples discretely over a finite time window. Therefore, the continuous and infinite Fourier transform cannot be used for signal analysis. Instead, the discrete Fourier transform (DFT) is used. For a finite set of N samples x_n sampled from $x(t)$ with sampling frequency ω_{samples} the DFT is defined as

$$\hat{x}_k = \frac{1}{N} \sum_{n=0}^{N-1} x_n e^{-2\pi i k n/N} \tag{3.13}$$

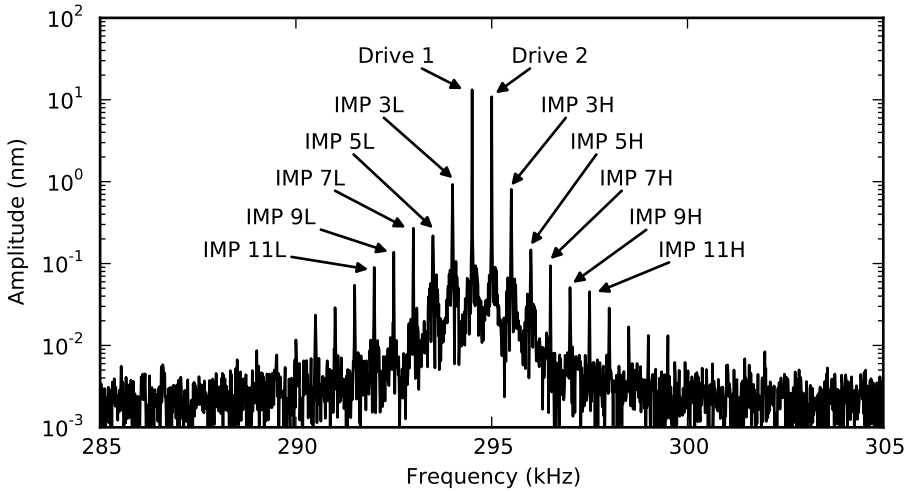

Figure 3.6: The intermodulation spectrum of a driven cantilever close to a sample surface. The cantilever is excited with the frequencies f_1 and f_2 close to the first flexural resonance frequency. Due to the nonlinear interaction between the tip and the surface many IMPs of different odd orders are created. The letters L and H denote if the IMP is at below or above the resonance frequency.

and the inverse transform is given by

$$x_n = \sum_{k=0}^{N-1} \hat{x}_k e^{2\pi i k n/N} \tag{3.14}$$

The frequency of the discrete spectral components $\hat{x}_k$ is given by

$$\omega_k = k\Delta\omega \tag{3.15}$$

where

$$\Delta\omega = \frac{\omega_{\text{samples}}}{N} \tag{3.16}$$

Moreover, the spectrum $\hat{x}_k$ is not only discrete but also has a maximum frequency of

$$\omega_{\text{Nyquist}} = \frac{\omega_{\text{samples}}}{2} \tag{3.17}$$

named after the Swedish-American engineer Harry Nyquist.

The discreteness and finiteness of the DFT spectrum puts up restrictions on the measurement of intermodulation in a narrow frequency band. The sampling frequency has to be at least two times higher than the highest frequency component in the signal. Otherwise frequency components above the Nyquist frequency will

mirrored to lower frequencies in the spectrum. This effect is called aliasing and it is regularly be observed in daily life when watching movie recordings of rotating wheels, which appear on the screen to rotate at lower speeds, in the wrong direction or stationary.

Furthermore, the finite measurement time can result in the DFT spectrum of a continuous mono-tone signal containing more than one non-zero frequency component. This behaviour is called Fourier leakage and it can be illustrated by considering a single frequency signal

$$x(t) = \cos(\bar{\omega}t) \tag{3.18}$$

at frequency $\bar{\omega}$ that is multiplied with a rectangular window function

$$\Pi(t) = \begin{cases} 1 & -\frac{1}{2} \leq t \leq \frac{1}{2} \\ 0 & \text{else} \end{cases} \tag{3.19}$$

such that

$$x_\Pi(t) = x(t)\Pi(t/T) \tag{3.20}$$

where T is the measurement time. Application of the convolution theorem yields the Fourier transform of the windowed signal,

$$\hat{x}_\Pi(\omega) = \frac{1}{4\pi}\frac{\sin\left((\omega-\bar{\omega})T/2\right)}{(\omega-\bar{\omega})T/2} + \frac{1}{4\pi}\frac{\sin\left((\omega+\bar{\omega})T/2\right)}{(\omega+\bar{\omega})T/2}. \tag{3.21}$$

For a sufficiently high sampling frequency the DFT spectrum of $x_\Pi(t)$ is given by the values of $\hat{x}_\Pi(\omega)$ at the frequencies $\omega_k = \Delta\omega$ as depicted in figure 3.7. If the signal frequency $\bar{\omega}$ is an integer multiple of $\Delta\omega$ the corresponding DFT spectrum exhibits only one non-zero spectral component from which amplitude and phase of the signal can be directly determined. In contrast, if $\bar{\omega}$ is not an integer multiple of $\Delta\omega$ the corresponding DFT spectrum contains many non-zero spectral components and the signal tone "leaks out" to other frequencies. When the Fourier leakage occurs, all non-zero spectral components (both amplitude and phases) are required to accurately determine signal frequency, amplitude and phase. For a signal containing multiple tones which are closely spaced and which are not integer multiples of $\Delta\omega$ it is not possible to determine the amplitudes and phases from a leaky DFT spectrum. Thus, the exact measurement of closely spaced IMPs requires a proper choice of the drive frequencies, the sampling frequency and the number of samples such that all IMPs occur at integer multiples of $\Delta\omega$.

Apart from the sampling parameters and the choice of drive frequencies, another source of Fourier leakage is a lack of synchronization of the clocks used for signal synthesis and acquisition. Figure 3.8 shows an early implementation of ImAFM where the drive signal is generated by two arbitrary waveform generators (AWGs) and the photodiode signal is acquired by an independent data acquisition card (DAQ). Each AWG and the DAQ has its own built-in clock which provides a reference

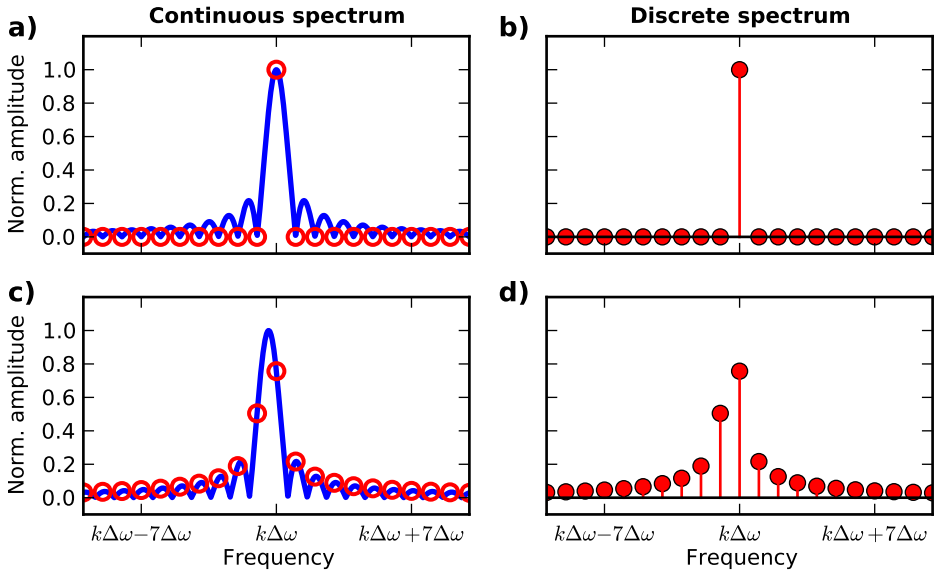

Figure 3.7: Relation between the signal frequency and Fourier leakage in the DFT spectrum. In the panels (a) and (c) the continuous Fourier transform of the windowed signal is shown and the red circles indicate which points of the continuous spectra form the DFT spectra in the panels (b) and (d). The DFT spectrum exhibits only one non-zero component (c), if the signal frequency is an exact integer multiple of the DFT base frequency $\Delta\omega$. In contrast, the DFT spectrum has many non-zero components (d), if the signal frequency is not an integer multiple of $\Delta\omega$ and

signal for the internal synthesis of output waveforms and the sampling frequency respectively. However, even with the high stability of the clock reference signals that can be achieved today, in a real experimental setup there is always a small drift between two reference clocks that can be due to different reasons like different physical clock implementations or different temperatures of the clocks. As a result of this clock drift the frequency of the a signal generated by an AWG might be appear to be slightly shifted when acquired with the DAQ. To mitigate this problem synchronization of all the clocks in the experimental setup is required such that no clock drifts with respect to another. In the setup shown in figure 3.8 the AWGs can be synchronized with each other by using a 10 MHz reference signal. The DAQ used in the experiment could not be synchronized to the same 10 MHz signal but an external sampling clock signal could be supplied by an additional AWG.

The importance of clock synchronization is illustrated in figure 3.9 which shows two DFT spectra of a signal with two closely spaced tones generated and measured with the setup in figure 3.8. The sampling frequency, the number of samples and

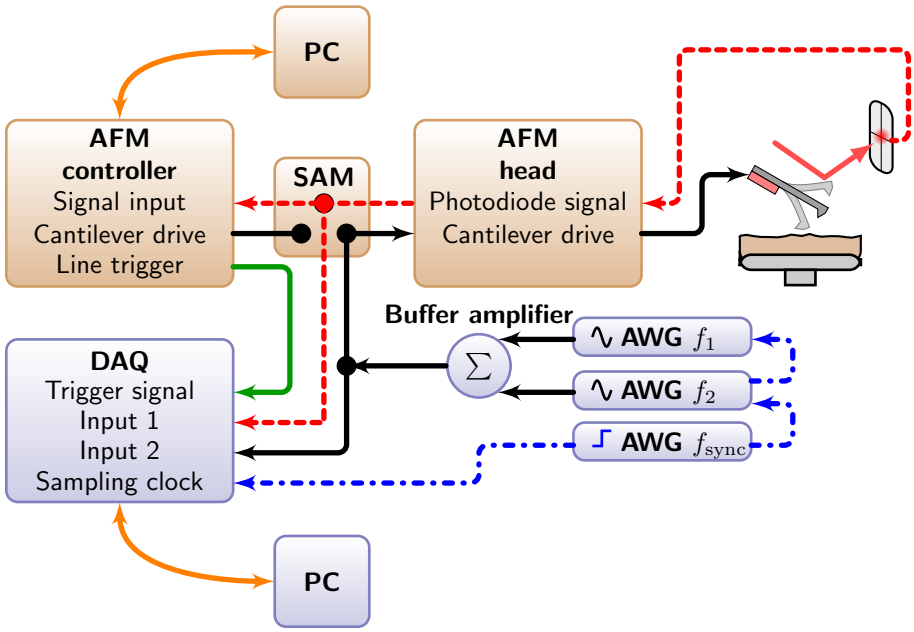

Figure 3.8: A setup for ImAFM experiments as used in reference [72]. The setup builds on a commercial AFM with an signal access module (SAM). The parts of the AFM system are shown in orange and the external components in blue. Three arbitrary waveform generators (AWGs) are used for synthesizing the drive signal (black) and the reference clock signal (blue). The photodiode signal (red) is measured with a data acquisition card (DAQ). Additionally, the drive signal is recorded to define a common reference signal for phase measurements.

the signal tomes are chosen such that all are multiples of the DFT base frequency $\Delta\omega$. In the case of synchronized clocks (blue line) the DFT spectrum shows two sharp peaks corresponding to the two signal frequencies. If the clocks are not synchronized (red line) the DFT spectrum exhibits significant Fourier leakage of the two frequencies. Thus, the correct choice of the DFT sampling parameters, the drive tones and synchronization of the clocks in the experimental setup are a crucial requirement for any multifrequency measurement technique, especially when these frequencies all occur in a narrow frequency band.

3.3 IMP phase measurements

IMPs not only have amplitude but also phase. The physical phase or phase shift is a quantity which is defined with respect to a reference signal. For an IMP phase

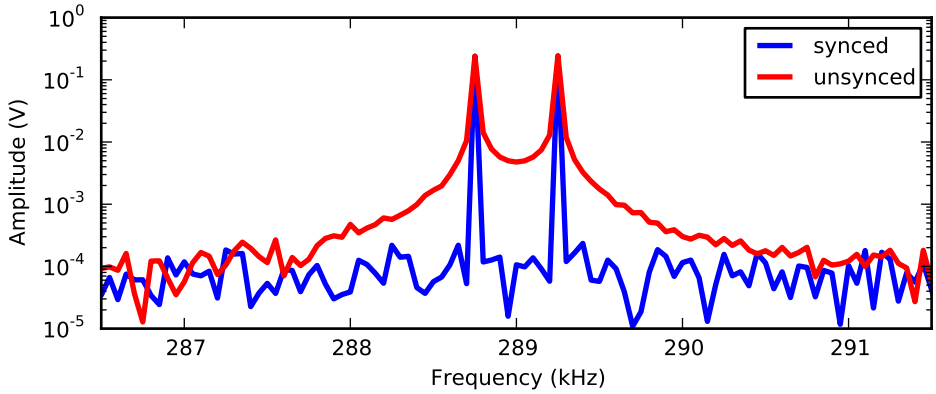

Figure 3.9: Measurement of a signal with two frequencies with un-synchronized and synchronized clocks in the experimental setup shown in figure 3.8. The un-synchronized measruements exhibits significant Fourier leakage whereas the synchronized measurement shows only two non-zero frequency components.

determined from a DFT spectrum, the reference signal is a cosine wave at the IMP frequency which is at maximum at the measurement start. To compare the values of two IMP phases at the same frequency the phases have to be defined with respect to the same reference signal. However, since the measurement start is generally arbitrary for any two measurements, the two measured phases would be defined with respect to two different reference signals and it would not be possible to compare their phases. In the ImAFM setup in figure 3.8 problem arises when scanning a surface where each scan line is an independent measurement. To create a common reference signal the drive signal was simultaneously recorded with the photodiode signal by the DAQ. The common reference signal for all measurements is then defined as a cosine whose argument is an integer multiple of 2π when both arguments of the drive cosines in equation (3.11) are zero, i.e. the reference signal for each IMP is at maximum when the drive beat is at maximum as shown in figure 3.10. The required phase shift for each IMP phase can readily be calculated from the phases of the measured drive phases φ_1 and φ_2 and the IMP frequency ω_{IMP} as

$$\varphi_{\mathrm{ref}} = \frac{\omega_{\mathrm{IMP}} - \omega_1}{\omega_2 - \omega_1} (\varphi_2 - \varphi_1) + \varphi_1 \tag{3.22}$$

where $(\omega_2 - \omega_1)/2$ and $\varphi_2 - \varphi_1$ can be identified with the frequency and phase of the beat envelope function.

If the references phase defined in equation (3.22) is subtracted from measured phases in all pixels of a scanned image, a consistent phase image forms in which the phases in all scan lines can be compared since they are all defined with respect to the same physical reference signal. An example of this phase correction is shown in figure 3.11 in which the raw measured phases do not seem to carry any valuable

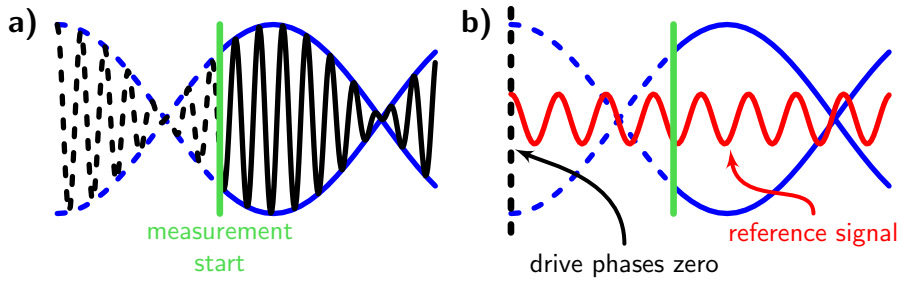

Figure 3.10: A measurement can start at any time during during the drive beat (a). To define a common reference signal for all IMP phase measurements the phase of an virtual reference signal at the desired frequency is computed such that the reference signal is at maximum when the drive beat is at maximum.

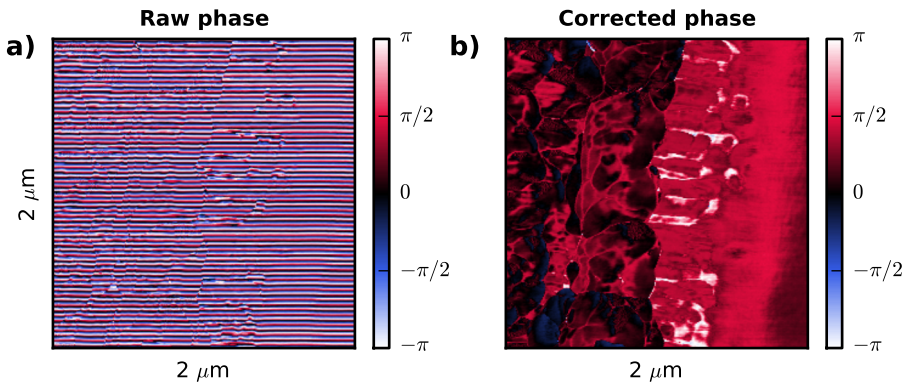

Figure 3.11: Scanned images of the phase of IMP 3H acquired with the setup in figure 3.8. The raw measured phase in the left panel does not seem to contain any information. However, after properly defining a common reference phase for each scan line an image forms which shows a surface with many features.

information whereas in the image with the corrected phases clearly shows detailed surface features.

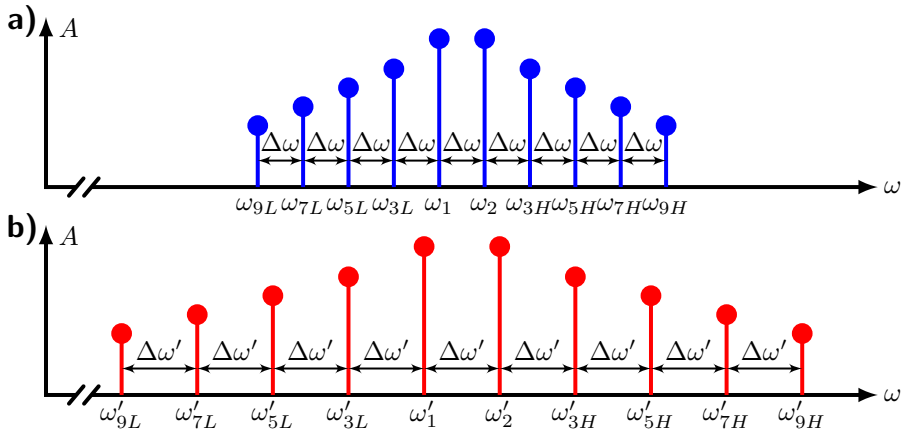

Figure 3.12: For a dual frequency drive all frequency components in the response spectrum are spaced by the difference between the two drive frequencies $\Delta\omega$ which in turn determines the required measurement bandwidth (a). To increase the speed of measurement, the frequency difference between the drive frequencies has to be increased. However, for an increased frequency spacing $\Delta\omega'$ the same number of IMPs are distributed over a wider frequency band.

3.4 Measurement time and the resonant detection band

The time T needed for an ImAFM measurement that is free of Fourier leakage is given by the inverse of the required DFT base frequency $\Delta\omega$,

$$T = \frac{2\pi}{\Delta\omega}$$

Hence, $\Delta\omega$ is called the measurement bandwidth and its largest possible value is given by the greatest common divisor of the frequencies in the drive signal. To increase the speed of the measurement the frequency spacing of the drive tones has to be increased, which in turn increases the frequency spacing between the IMPs. Thus, an increased measurement speed causes the same number of IMPs to be distributed over a wider frequency band as depicted in figure 3.12. However, due to the decreasing transfer gain of the cantilever's linear response function, the IMPs further away from resonance have lower SNR. Eventually, the IMPs disappear into the noise and the information they contain about the tip-surface interaction is no longer accessible. Therefore, a trade-off is inevitable between measurement speed and the number of IMPs that can be measured with good SNR.

The amount of bandwidth around a resonance that is available to measure IMPs with a signal-to-noise ratio bigger than one is quantified by the resonant detection bandwidth[85]. The resonant detection bandwidth is defined as the width of the

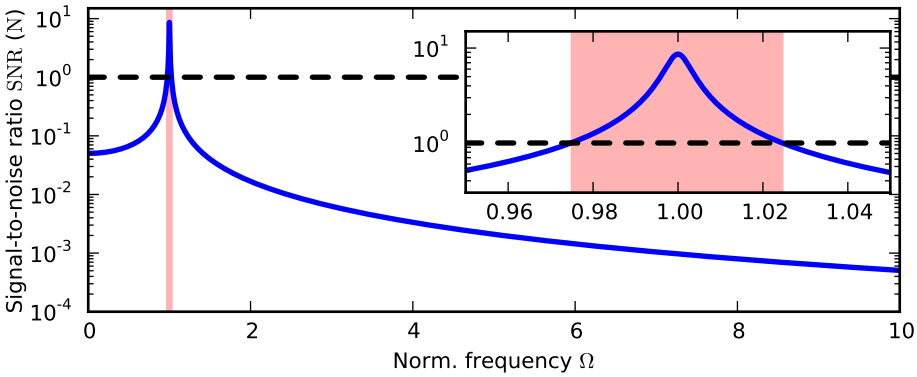

Figure 3.13: The SNR for a signal of strength 100 pN. The detector and thermal noise parameters are the same is in figure 1.5. The resonant detection band (red region) is the frequency band in which the SNR is bigger than one. For the harmonic oscillator subject to detector noise and thermal noise the resonant detection band is a narrow band around resonance.

frequency band in which a force of a specified strength can be measured with a specified measurement bandwidth at a signal-to-noise ratio bigger than one as depicted in figure 3.13 for a signal of strength 100 pN in the presence of thermal and detector noise. If thermal noise can be neglected, it can be shown that the resonant detection bandwidth is nearly independent of the cantilever's quality factor for a force of 10 pN and a measurement bandwidth of 500 Hz, whereas a lower spring constant increases the resonant detection bandwidth. In the same manner an increased resonance frequency increases the resonant detection bandwidth, making ImAFM compatible with high-speed scanning and higher-frequency cantilevers that are becoming more widely used at present[86, 87, 88]. On the other side, operation in liquids without exciting multiple cantilever resonances seems to be possible for similar cantilever parameters as for torsional harmonic cantilevers[89]. One should note that the analysis presented in [85] considers detector noise as the dominant noise source. However, thermal noise is also present in an experiment and might dominant over the detector noise over a wide frequency band in liquid environments.

3.5 FPGA-based measurements

To automatically satisfy the requirements avoiding Fourier leakage and to provide a "coherent" phase signal for all scan lines a new experimental setup based on a field programmable gate array (FPGA) was built by Erik and Mats Tholén[90]. An FPGA offers a performance comparable to an application-specific integrated circuit (ASIC) while at the same time being programmable. In the new FPGA setup only one clock is used for both signal synthesis and acquisition, removing

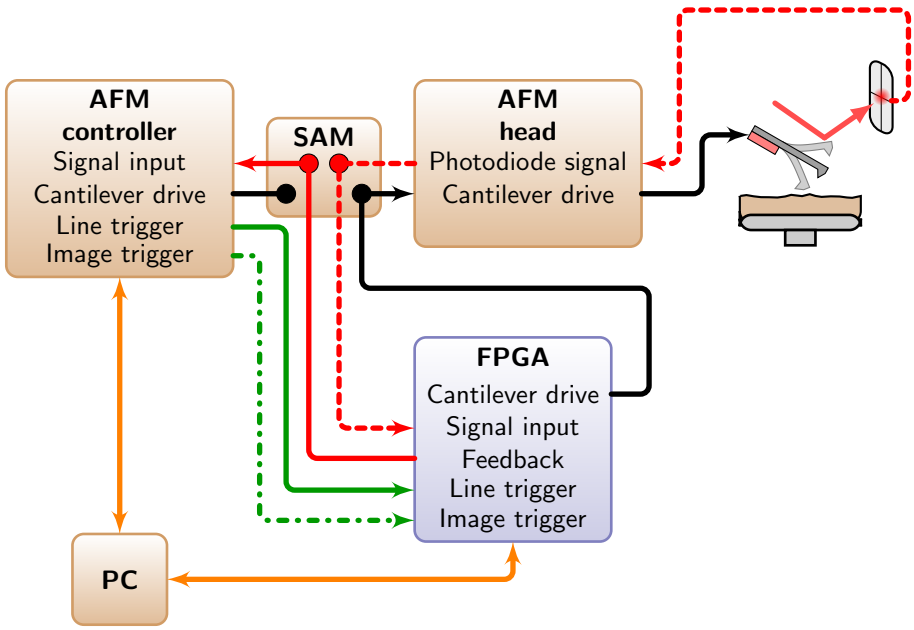

Figure 3.14: In the FPGA-based setup the FPGA is the only component outside the AFM system. From the measured photodiode signal the FPGA calculates a feedback signal which is routed to to the signal input of the AFM controller. Since all computationally extensive Fourier calculations are performed directly on the FPGA, the computer of the AFM system can control both the AFM and the FPGA.

the requirement of the complicated external synchronization of different clocks. Moreover, once started the measurement is continuous which implies that all phase measurements are directly comparable without an additional phase shift.

The FPGA-based setup offers the advantage of a real time measurement that could not be achieved with the previous setups. While scanning a surface the amplitude and phases of 32 different IMPs can be simultaneously acquired in real time allowing for a greatly improved interaction with the experiment. The FPGA platform is compatible with AFM systems which provide access to the cantilever drive signal, the photodiode signal and the line and image triggers. The signal flow is depicted in figure 3.14 where the FPGA is the only component outside the AFM. Furthermore, in the previous setups the feedback signal was generated by de-modulation in the AFM electronics which could not be synchronized to the external equipment. Thus, uncontrolled Fourier leakage was influencing the feedback and thereby image acquisition. In the FPGA-based setup the feedback signal is

generated in real-time on the FPGA which allows for a leakage-free measurement. The generated feedback signal mimics a contact mode deflection signal and is fed into the feedback loop of the AFM controller.

3.6 Intermodulation AFM Software Suite

The FPGA hardware platform is one advancement that improves the interaction with the experiment during a measurement, making the ImAFM measurement technique available for users that are not familiar with the experimental aspects discussed above. Another element is the "Intermodulation AFM Software Suite" which was developed to control the FPGA hardware platform and display and analyze multifrequency data. The software suite allows for a smooth interaction with the hardware setup and guides the user to chose the right parameters for an ImAFM measurements. A simple intuitive graphical user interface helps the users which are not so familiar with ImAFM or AFM experiments and it visualizes the measured data in real-time. Depending on the measurement results the user can change experimental parameters interactively while running the experiment. Moreover, the software suite takes care of the data storage and automatically logs chronologically the experiment such that all important experimental parameters are saved for later analysis. Different force reconstruction algorithms are included in the software suite and they can be used during data acquisition and for the analysis of save data. As part of these analysis capabilities is the calibration of cantilever constants from measured noise data included in the software suite.

For the implementation of the software suite we chose Python[91] as the programming language since it offers several advantages. Python is a well-established open-source programming language suitable for creating small scripts but also bigger software projects and running on the most popular operating systems (Micorsoft Windows, Apple Mac OS and Linux). The Python programming language is simple to learn allowing new students to contribute quickly to the software and it is distributed with a comprehensive standard library and a huge number of external packages exist in the open-source community. One of these external packages is wxPython[92] which we used for implementing the graphical user interface. wxPython is derived from the C library wxWidgets and provides a native look-and-feel of the user interface on Windows, Mac OS and Linux. The data handling is done by NumPy/SciPy[93] which is a Python wrapper of different LAPACK routines and netlib packages. For visualizing and plotting the data we use matplotlib[94, 95] integrated in the wxPython interface. The software suite was implemented by several developers. Thus, we established the use of mercurial[96] as a distributed versioning system.

The software suite underwent several versions and has grown into a project with approximately 40000 lines of code. A screenshot from the current development version (changeset 1782) is shown in figure 3.15. On the left of the program window a toolbar guides the user through the ImAFM work flow (from top to bottom: find-

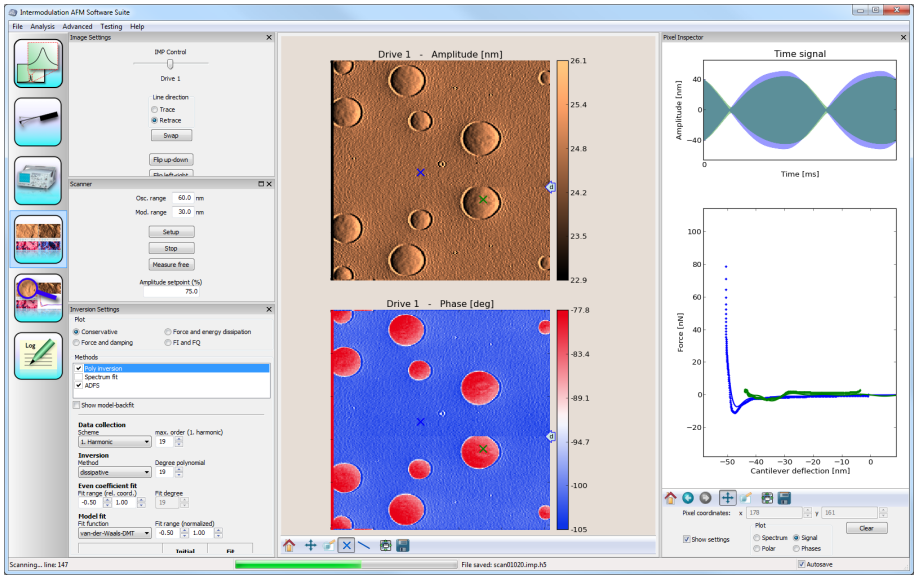

Figure 3.15: The Intermodulation AFM Software Suite on Windows 7.

ing the cantilever resonance, thermal calibration, optional setup, scanning, offline analysis, logbook). In the center the amplitude and phase images at the first drive frequency are shown as a polymer blend sample is scanned. Shown on the right is the measured tip motion and the reconstructed force curves at two pixels marked with x's in the image.

3.7 Experimental results

Two types of experiments have been performed using the ImAFM measurement technique. The first type of measurement is called ImAFM approach measurement in which the intermodulation response of the cantilever is measured as the static probe height is slowly moved toward and away from the surface above a fixed point on the sample surface. Even though the cantilever approaches the surface continuously, as shown in figure 3.16a, the time for one ImAFM measurement ($\sim 2\ \mu$s) is much smaller than the time for a complete surface approach (~ 1 s). Therefore, the static probe height is considered constant during a single ImAFM measurement.

In the second type of measurement the cantilever is scanned latterly above the sample surface while a feedback mechanism aims to keep the static probe height above the surface constant as shown in figure 3.16b. From the measured tip motion images of the IMP amplitudes and phases over the sample surface are generated. In all imaging experiments so far the IMP amplitude measured at the first drive frequency served as the input quantity for the AFM feedback system. This feed-

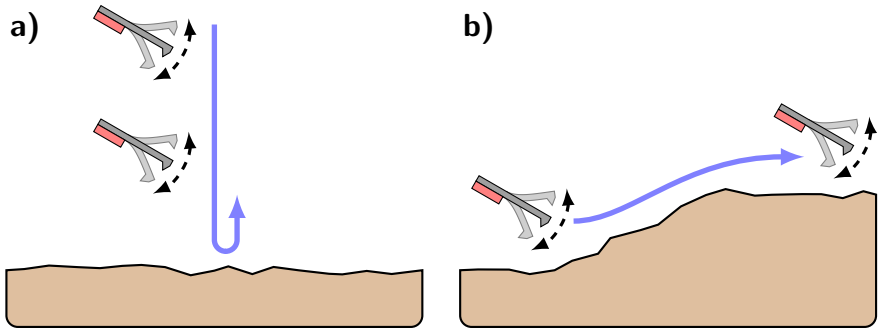

Figure 3.16: During an ImAFM approach the static probe height is slowly changed while the lateral position of the tip is kept constant (a). In contrast in ImAFM imaging a feedback mechanism aims to keep the static probe height constant while the tip is scanned over the surface.

back mode produced images with resolution not worse than conventional AM-AFM. However, with ImAFM much more data is available than the response at a single frequency and in the future, this data might be used to develop new feedback schemes that are faster and allow for optimization of the image resolution and decreased the back action exerted on the sample while scanning.

3.7.1 ImAFM approach measurements

Figure 3.17 shows the amplitude-distance curves at the drive frequencies and different IMPs frequencies obtained from ImAFM approaches on a silicon oxide, a poly(methyl methacrylate) (PMMA) and a polydimethylsiloxane (PDMS) surface[97]. The response at the drive frequencies and the IMP frequencies exhibits a complex dependence on the static probe height. The amplitudes at the drive frequencies decreases nearly linearly as the surface is approached, providing a suitable signal for the topography feedback system. However, at the onset of interaction between the tip and the surface there is some non-monatonic behavior of the response amplitudes at the drive frequencies which reflects the transition from the purely attractive forces to dominantly repulsive force acting on the tip. Similar behaviour is routinely observed in conventional dynamic AFM using only one drive frequency.

The behaviour of the amplitudes at IMP frequencies depends on the order of the IMP. Generally, the higher the order of an IMP the more minima and maxima can be found in the amplitude-distance curves. Moreover, the IMP response is strongly dependent on the surface material. For a stiff materials the amplitudes at high order IMPs are higher than for soft materials. Thus, the information encoded in the IMPs can be used to generate compositional contrast on different materials. The experimental observation of a strong material dependence of the IMP response

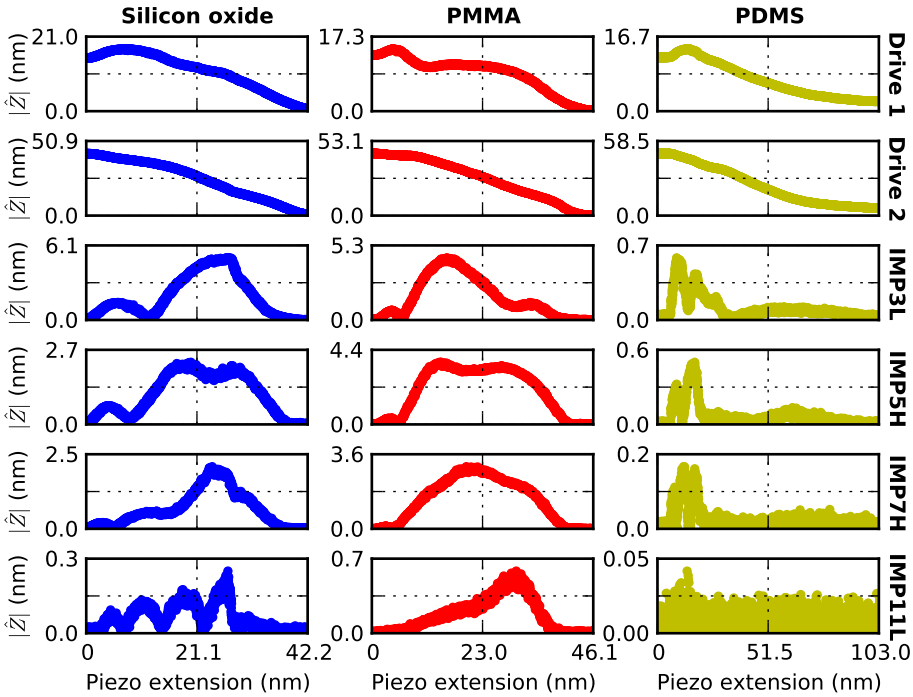

Figure 3.17: The measured amplitudes at the drive frequencies and different IMP frequencies during ImAFM approaches on different materials. Since the absolute probe height is unknown during an experiment the x axis corresponds to the piezo extension in z direction.

is also supported by the numerical simulations. In figure 3.18 the amplitudes at the drive frequencies and at different IMP frequencies for simulated ImAFM approach measurements are shown as a function of static probe height and the material stiffness. For the interaction between the tip and the sample we assume a van der Waal-DMT force model[98] of the form

$$F_{\mathrm{DMT}}(z) = \begin{cases} -\frac{HR}{(a_0 - z)^2} & z > 0 \\ -\frac{HR}{a_0^2} + \frac{4}{3} E^* \sqrt{R} (-z)^{3/2} & z \leq 0 \end{cases} \tag{3.23}$$

where H is the Hamaker constant, R is the tip radius and E^* the effective stiffness of the combined tip-sample system. For integrating the equation of motion we used CVODE[99], an adaptive step size integrator whit discrete event detection to account for the piecewise definition of the vdW-DMT force model. The simulations reveal three different regimes in which the IMP and drive amplitudes show qualitatively different behaviour: At low stiffness the drive and IMP amplitudes depends predominantly on the static probe height. For stiffness between 10^{-2}

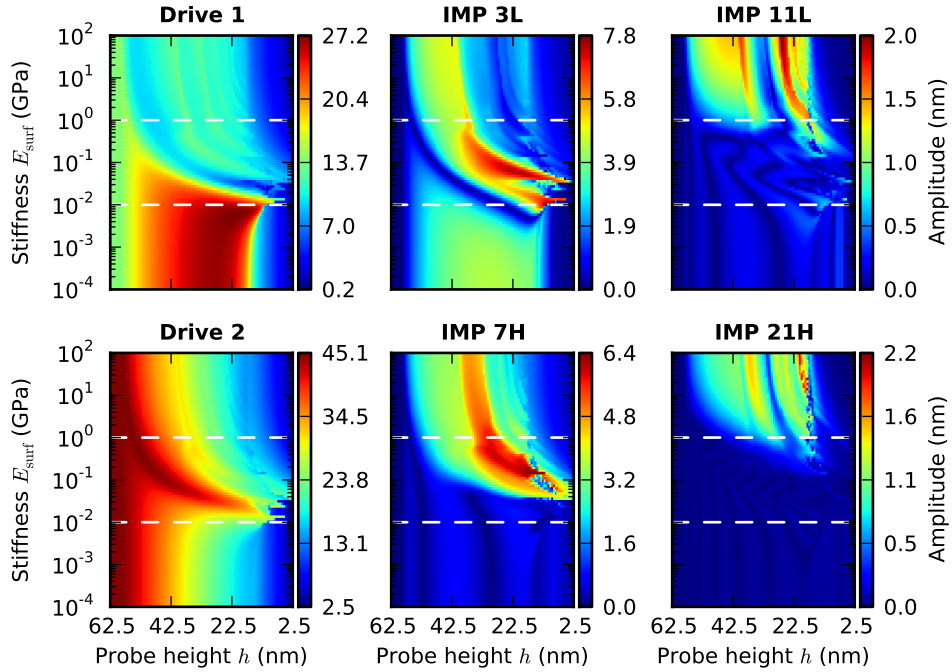

Figure 3.18: Amplitudes at the drive frequencies and different IMP frequencies as a function of the static probe height and the sample stiffness. The dashed lines separate the regions in which the simulated response shows different behaviour.

and 10^0 GPa both amplitudes exhibit a strong dependence on both static probe height and material stiffness, with sudden amplitude jumps for different parameters. Above 10^0 GPa the dependence on the material stiffness is weaker but as in experiment, the amplitudes of higher order IMPs tend to increase further for stiffer materials. However, a comparison between experiments and simulations only gives qualitative insight into the IMP behaviour since the simulations rely on a force model which is idealized in the sense of the assumed interaction geometry and it neglects the presence of dissipative interactions. Moreover, it is not clear if the van der Waals-DMT model is applicable over the full stiffness interval studied in the simulation.

The measured phases in an ImAFM approach measurement show an nearly linear dependence on the static probe height as shown in figure 3.19. This linear phase evolution makes the IMP phase an alternative feedback signal for tracking the surface topography. However, when the IMP amplitude goes to zero the IMP phase often jumps by $\pi/2$. The rate of the phase change is higher for higher order IMPs which can be seen in the polar plots of figure 3.20 where amplitude and phase information have been combined. The multiple loopings of the path in the ploar

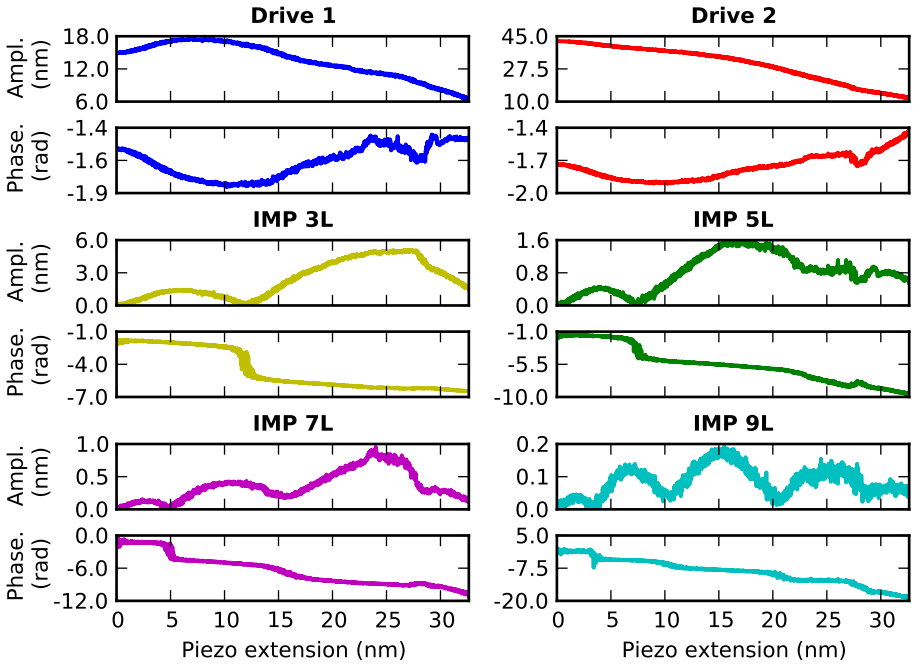

Figure 3.19: The measured amplitudes and unwrapped phases at the drive frequencies and different IMP frequencies during an ImAFM approach on silicon oxide. The x axis shows the piezo extension in z direction.

plot for higher order IMPs reflects the higher the rate of phase change.

3.7.2 ImAFM imaging

The time required for an ImAFM measurement is the inverse of the frequency spacing in the IMP spectrum and this can be set by the user in the experiment. Typically a spacing of 500 Hz is used, giving a measurement time of 2 ms. This time allows for scanning a sample surface at normal speeds for "tapping mode^{TM}" AFM (1 Hz scan line frequency), while performing an ImAFM measurement in every pixel. In this manner a large number of IMP amplitude[71] and phase images[72] can be generated in a single scan of the surface. These IMP images can be considered as additional information channels not present in conventional dynamic AFM. Various samples have been imaged with ImAFM. In addition to the data previously published[71, 72] the example shown in figure 3.21 illustrates the analytic capabilities of ImAFM. The topography image in figure 3.21a shows pillars of photo-resist on top of a anti-reflecting coating (sample courtesy of David Abraham, IBM). The height of the pillars is 150 nm and the scan size 2×2 μm^2. The topography image

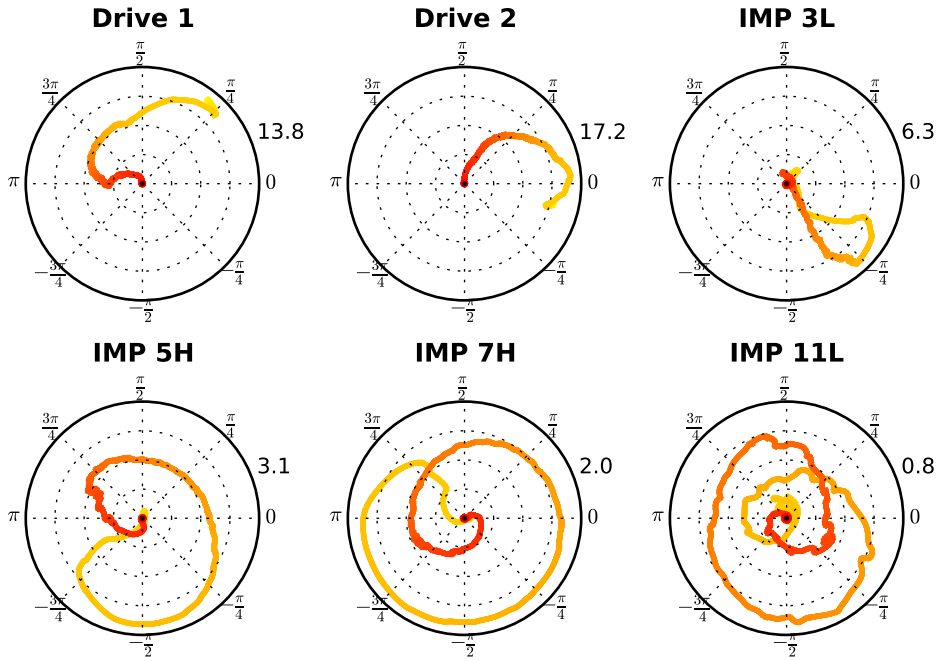

Figure 3.20: Polar plots of the amplitudes and phases at the drive frequencies and different IMP frequencies during an ImAFM approach on silicon oxide. At the beginning of the measurement (yellow end of the plotted lines) the drive amplitudes are at maximum while the IMP amplitudes are zero. While the static probe height slowly changes the IMP phasors loop several times around. The higher the order of an IMP the more loops it shows until the end of the measurement (red end of the plotted lines)

was obtained using the AFM feedback to keep the amplitude at the first drive frequency constant and does not show any significant other features on the surface. In contrast, the amplitude of the IMP 3H in figure 3.21b clearly show small features on top of the pillars and on the background coating. Since these features do not correlate with features in topography we attribute them to variation in the material composition. This compositional contrast can also be found in IMPs of different order and the impression of all IMP improves the qualitative analysis of the sample.

Apart from the IMP amplitude images, the IMP phase images can also be used to identify different materials. Figure 3.22 shows two images from the ImAFM scan used in the study of a polystyrene (PS) and PMMA blend sample in[85]. PS and PMMA are immiscible and so the blend forms PS- and PMMA-rich domains when spin-coated from solution (for fabrication details see A.1). These two domains can

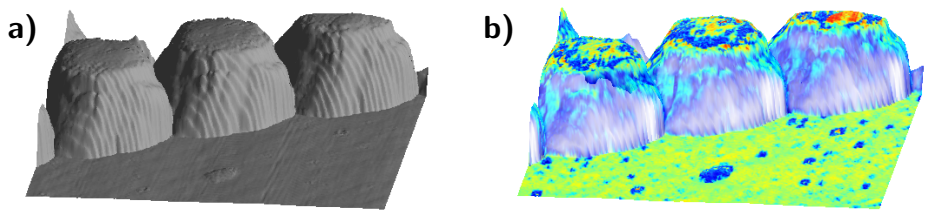

Figure 3.21: 3D topography (a) of pillars of photo resist with a height of 150 nm on a anti-reflective coating (sample courtesy of David Abraham, IBM) and the amplitude of IMP 3H plotted on top of the 3D topography (b). Both topography and IMP 3L data have been acquired in the same ImAFM scan with a scan size of $2 \times 2\ \mu\text{m}^2$.

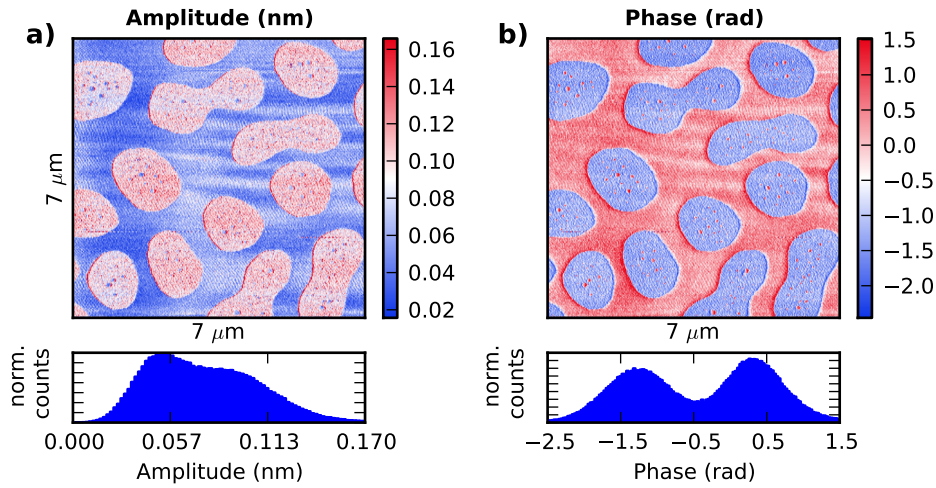

Figure 3.22: Amplitude (a) and phase (b) of IMP 9H on a blend PS/PMMA blend spin-cast on a silicon oxide substrate. The image has a resolution of 256×1024 pixels and was acquired within 17 minutes.

be clearly identified in the amplitude and phase image of IMP 9H. The enhanced phase sensitivity for high-order IMPs results in a high compositional resolution revealing small PS-rich domains inside the PMMA-rich domains which are due to a secondary phase separation of the two polymers. The amplitude and phase histograms reveal that the contrast is better in the phase image.

ImAFM imaging has been used to explore new compositional contrasts on different samples. However, the possibilities of ImAFM to increase the lateral resolution

or decrease the back-action on the sample while scanning have not been explored so far. A step into this direction could be the development of new true multifrequency feedback schemes which are not based on the amplitude of one single frequency component. Thus, feedback schemes that are more sensitive or motivated by more physical constraints might enhance ImAFM in the future.

One problem that is inherent to ImAFM, and generally multifrequency AFM, is the need for interpretation of the measured raw spectral data. The amplitude and phases can not be directly mapped to physical surface properties and their interpretation might be different for different samples. Therefore, alternative data representation schemes and new analysis methods are required for multifrequency AFM to develop from a qualitative imaging technique to a quantitative microscopy technique.

Chapter 4

Interpreting narrow-band AFM

4.1 Motion and force

Both conventional dynamic AFM (AM-AFM and FM-AFM) and ImAFM can be considered as a specific case of narrow-band dynamic AFM[100], where the tip motion is confined in a narrow frequency band surrounding a high quality-factor resonance. The center frequency of the band is much higher than its bandwidth as depicted in figure 4.1a. In conventional AFM the band is populated by only one non-zero frequency component whereas in ImAFM the full band is filled with discrete frequency components.

In the time domain, the tip motion in conventional dynamic AFM can be written as

$$z(t) = A\cos(\bar{\omega}t + \varphi) + h \tag{4.1}$$

where h is the static probe height. The oscillation amplitude A and phase φ are constants and the narrow frequency band is defined such that its center frequency is the oscillation frequency $\bar{\omega}$. However, generally the time domain tip motion in narrow-band AFM is given by

$$z(t) \approx A(t)\cos\left(\bar{\omega}t + \varphi(t)\right) + h \tag{4.2}$$

where the oscillation amplitude A and phase φ themselves are function of time. Their time-dependence is given by the narrow band spectrum that is down-shifted by $\bar{\omega}$ as illustrated in figure 4.1b. The down-shifted spectrum is the spectrum of a complex-valued envelope function $E(t)$ which determines the oscillation amplitude A and phase φ as

$$A(t) = |E(t)| \tag{4.3}$$

$$\varphi(t) = \arg\left(E(t)\right) \tag{4.4}$$

Thus the motion is completely described by a rapidly oscillating part and a slowly varying envelope function. One should note that equation (4.2) also describes

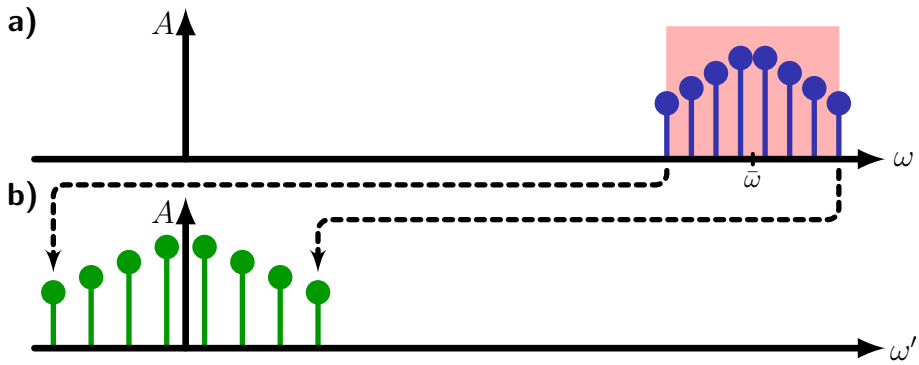

Figure 4.1: The measured spectrum in narrow-band AFM is confined to frequency band with a center frequency $\bar{\omega}$ much higher than the bandwidth (a). The spectrum of the envelope function is determined by down-shifting the original spectrum such that the new center frequency is zero (b)

frequency shifts. The instantaneous frequency shift $\delta\omega$ is given by the derivative of the time-dependent phase

$$\delta\omega(t) = \frac{\partial\varphi(t)}{\partial t} \tag{4.5}$$

One important goal in dynamic AFM is not only to describe the tip motion accurately, but also to understand which forces between the tip and the sample which perturbs the tip motion since from knowledge of this tip-sample force a manifold of sample properties can be derived. To separate the tip-surface force F_{ts} from the drive force F_{drive} we consider the equation of motion of an engaged cantilever

$$m\ddot{z} + \frac{mQ}{\omega_0}\dot{z} + kz = F_{\text{ts}}(t) + F_{\text{drive}}(t) \tag{4.6}$$

and a cantilever away from the surface

$$m\ddot{z}_{\text{free}} + \frac{mQ}{\omega_0}\dot{z}_{\text{free}} + kz_{\text{free}} = F_{\text{drive}}(t) \tag{4.7}$$

where the tip-surface force is zero and the tip motion z_{free}only depends on the drive force. Subtracting equation (4.7) from (4.6), we can easily solve for the tip-surface force $\hat{F}_{\text{ts}}$ in Fourier space such that

$$\hat{F}_{\text{ts}} = \hat{\chi}^{-1}\left(\hat{z} - \hat{z}_{\text{free}}\right) \tag{4.8}$$

where $\hat{\chi}$ is the cantilever's linear response function. Although this relation is mathematically quite simple it can be seldomly used to determine the forces in a real experiment. The equations (4.1) and (4.2) describe the motion only approximately

in that sense that there might be non-zero spectral components of the motion outside of the narrow frequency band. These components do not contribute significantly to the motion spectrum and are usually below the detection noise floor. However, they might correspond to significant components in the force spectrum as the inverse linear response function $\hat{\chi}^{-1}$ grows rapidly away from the resonances. In this sense the cantilever can be considered as a band-pass filter which filters out all the components of the time-dependent tip-surface force which are outside a cantilever resonance. Reconstructing from this filtered, or partial force spectrum is the fundamental dilemma in measurement with dynamic AFM.

4.2 Force representation and limits of blind force reconstruction

Up to this point the tip-sample force has been considered as a time-dependent force. However, to derive sample properties from the tip-surface force it is necessary to establish a functional relation between the force and the tip motion. The tip-surface force is often considered to have an implicit dependence on time, as the tip-surface force usually depends on the instantaneous tip position z and velocity $\dot{z}$ and the past tip trajectory $\{z(t)\}$ like for hysteretic forces,

$$F_{\mathrm{ts}}(t) = F_{\mathrm{ts}}\left(z(t), \dot{z}(t), \{z(t)\}\right). \tag{4.9}$$

The tip-surface force is frequently decomposed into a conservative and a non-conservative, dissipative, part

$$F_{\mathrm{ts}}\left(z, \dot{z}, \{z(t)\}\right) = F_{\mathrm{c}}(z) + F_{\mathrm{nc}}\left(z, \dot{z}, \{z(t)\}\right) \tag{4.10}$$

for which the conservative part only depends on the tip position. However, materials might exhibit a frequency-dependent elastic response which is considered to be constant over the frequency range used in a typical AFM experiment. The decomposition into a conservative and a non-conservative force has been discussed extensively in the literature[101, 102, 103, 104, 105, 106, 107, 108]. Nevertheless, no unified approach to the analysis has emerged, and especially the treatment of the non-conservative part of the interaction remains difficult. A variety of different models for the non-conservative part have been put forward. One popular example is the representation of the non-conservative interaction with a position-dependent viscous damping λ such that

$$F_{\mathrm{damp}}(z, \dot{z}) = -\lambda(z)\dot{z} \tag{4.11}$$

Other models of hysteretic behaviour and nonlinear dependence on the tip velocity have been investigated[108, 109]. However, all these models are rather specific, describing only one dissipation mechanism, and they might not be applicable for non-conservative forces of different physical origin. A general description or representation of dissipative forces has been missing.

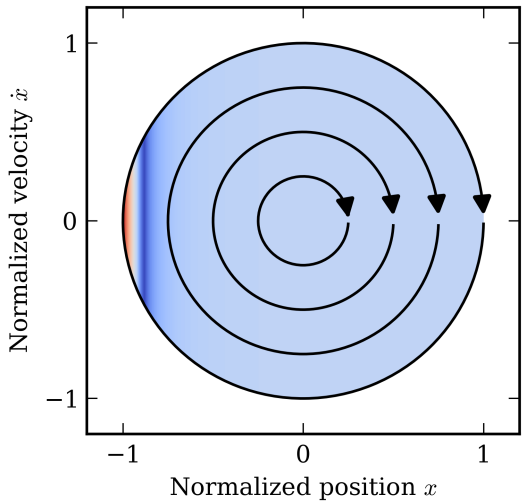

Figure 4.2: The force as a function of normalized tip position and velocity. Sinusoidal motion corresponds to circular orbits which do not intersect. Thus, every point in phase space can uniquely be mapped to one tip trajectory.

The difficulty in finding a complete force representation is incorporation of the dependence on the history of the tip motion. At fixed static probe height this dependence can be implemented for narrow-band AFM using the fact the oscillation amplitude and phase vary slowly and can be considered constant during a fast cantilever oscillation cycle. Under this approximation each fast oscillation cycle corresponds to a circular trajectory in phase space. The trajectories for different oscillation amplitudes do not intersect and therefore each point in phase space is linked to a unique past tip trajectory. The force is then completely described as a function of instantaneous tip position and velocity as shown in figure 4.2. Thus, in narrow band AFM at fixed static probe height even complicated hysteretic forces are fully described as simple two dimensional functions in phase space. Since there is always a maximum oscillation amplitude in an experiment it is sufficient to define the force on a finite disk. This force representation is called the force disk and it is a complete description of the forces in an narrow-band AFM experiment at fixed static probe height[110].

To understand which parts of the force disk are contained in the partial tip-sample force reconstructed from the measured tip motion using equation (4.8) the force disk is expressed in the polar coordinates A and φ and expanded into an orthogonal set of basis functions,

$$F_{\mathrm{ts}}(A,\varphi) = \sum_{n=0}^{\infty} \sum_{m=-n}^{n} a_{nm} \Psi_{nm}(A,\varphi). \tag{4.12}$$

When using a Zernike expansion or a Fourier-Bessel expansion of the force, it can be readily shown that only the coefficients $a_{\pm 1m}$ contribute to the partial force in narrow band AFM. Therefore, a complete reconstruction of the force disk requires additional assumptions about the force in order to determine the other expansion coefficients.

4.3 Single cycle time domain analysis

In conventional AM-AFM and FM-AFM the measured tip oscillation is usually expressed in terms of the oscillation amplitude and phase or the oscillation frequency and the drive force. Equivalently, the data can also be expressed in terms of two force quadratures. The quadrature F_I corresponds to the tip-surface force that is in-phase with the tip motion, the quadrature F_Q corresponds to the out-of-phase component of the tip-surface force. For force depending on tip position and velocity the two quadratures can be written as

$$F_I(h, A, \bar{\omega}) = \frac{\bar{\omega}}{2\pi} \int_0^{\frac{2\pi}{\bar{\omega}}} F_{\mathrm{ts}} \left(A\cos(\bar{\omega}t) + h, -\bar{\omega} A \sin(\bar{\omega}t) \right) \cos(\bar{\omega}t) dt, \quad (4.13)$$

$$F_Q(h, A, \bar{\omega}) = \frac{\bar{\omega}}{2\pi} \int_0^{\frac{2\pi}{\bar{\omega}}} F_{\mathrm{ts}} \left(A\cos(\bar{\omega}t) + h, -\bar{\omega} A \sin(\bar{\omega}t) \right) \sin(\bar{\omega}t) dt. \quad (4.14)$$

The force quadratures F_I and F_Q are basically the real and imaginary part of the first expansion coefficient in a Fourier series expansion of the time-dependent tip-surface force in the oscillation frequency $\bar{\omega}$. The force quadrature F_I is only affected by the conservative part of the tip-surface force and has earlier been identified as the virial of the tip motion[42] whereas F_Q depends only on dissipative interactions and is connected to the energy dissipated during one oscillation cycle[102, 103, 43]. Moreover, the force quadratures serve as the the basic input quantities for all force spectroscopy methods in single frequency AM-AFM[44, 46, 45, 47] and FM-AFM[41, 38, 37, 39] for which they have been considered as functions of the static probe height h only.

The fact that F_I and F_Q depend also on the oscillation amplitude A and frequency $\bar{\omega}$ can be used to apply the force quadrature concept to the more general case of multifrequency narrow-band ImAFM. In the time domain the tip motion is given by equation (4.2) in which the oscillation amplitude and phase can be considered to be constant over one fast oscillation cycle. We then decompose the tip motion into single oscillation cycles where each oscillation cycle has a fixed amplitude, frequency or phase as shown in figure 4.3. The slow variation of amplitude and phase can be determined from the motion envelope function. For the sake of discussion we focus on the case of constant oscillation frequency in what follows.

Application of the linear response function converts the measured tip motion envelope function into an envelope function for the partial force signal. It can be shown that the force envelope function can be used to determine the values of F_I

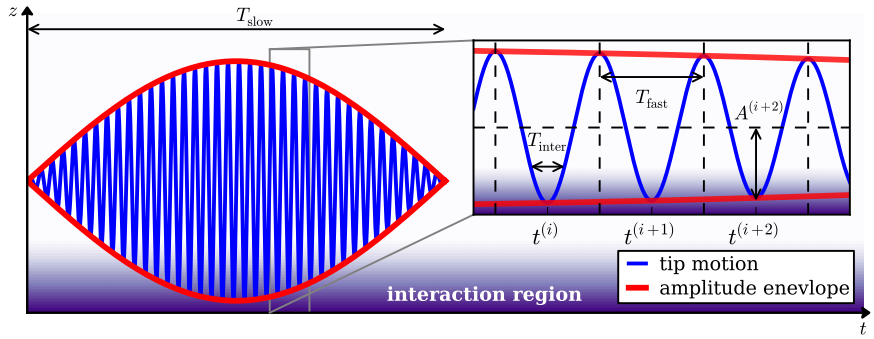

Figure 4.3: Sketch of a narrow-band signal. On the slow time scale T_{slow} the tip motion shows an amplitude modulation. On the fast time scale T_{fast} the signal rapidly oscillates. During each oscillation cycle the tip interacts with the surface for the time T_{inter} during which the oscillation amplitude and phase are approximately constant.

and F_Q for every single oscillation cycle. This is illustrated in figure 4.4 for a simulation with a known model force. In the upper panel the tip motion is shown over a time interval which is relatively small compared to the required measurement time. In the lower panel the solid red curve is actual force acting on the lever. The solid yellow line is the force signal given by the partial force spectrum. The dashed red line is a signal determined from to the first component of a Fourier expansion of the full tip-surface force for each tip oscillation cycle. As the red dashed curve and the solid yellow curve are in excellent agreement, the value of the force envelope function is equal to the first harmonic of a local Fourier expansion of the force for each oscillation cycle. This interpretation of the motion and force envelope functions is presented more rigorously in reference [100].

Since each tip oscillation cycle has a different amplitude, a single ImAFM measurement can be interpreted as the rapid measurement of the amplitude dependence of the force quadratures F_I and F_Q over a finite amplitude interval at fixed static probe height. The representation of the measured data in terms of the force quadrature F_I and F_Q, as opposed to the raw motion spectra has the advantage of a more direct physical interpretation. Moreover, since the force quadratures are defined for simple sinusoidal motion they disentangle the analysis of force from the actual tip motion.

Considering the force quadratures as functions of both static probe height and oscillation amplitude allows for a comparison of conventional AM-AFM and FM-AFM force measurement techniques with ImAFM. In conventional FM-AFM the static probe height is slowly varied while keeping the oscillation amplitude constant, whereas in AM-AFM the oscillation amplitude can change during the slow surface approach. The FM-AFM measurement approach correspond to measurements of

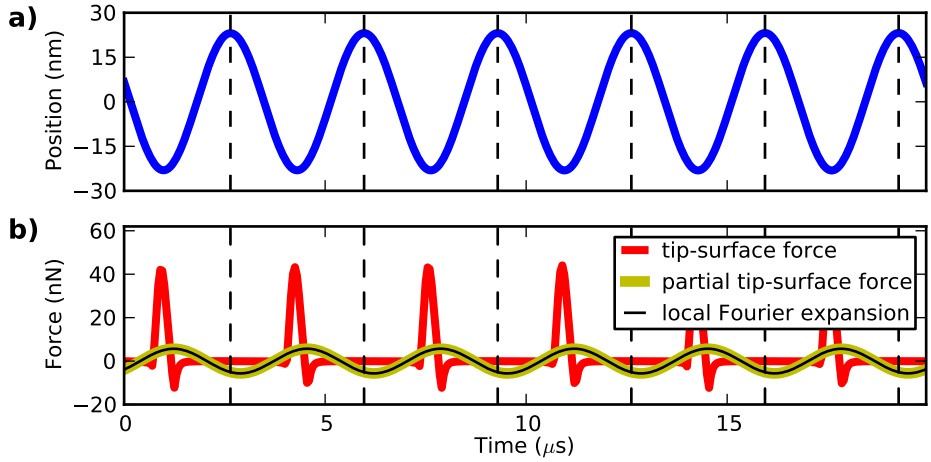

Figure 4.4: The tip motion (a) over a few oscillation cycles of simulated tip motion. The complete tip-surface (red line) shows a complicated force pulse during each oscillation cycle whereas the measured partial force (yellow line) exhibits only sinusoidal behaviour and is in excellent agreement with the force corresponding to the first component in a local Fourier expansion for each oscillation cycle of the complete force (black line).

F_I and F_Q along a horizontal path in the h-A plane as shown in figure 4.5. AM-AFM has a more complicated path in the where jumps can occur due to dynamic instabilities. In contrast, a single ImAFM measurement does not require a change of the static probe height and its measurement path is a vertical line in the $h-A$ plane. During a slow ImAFM approach an single ImAFM measurement is performed at each probe height. Thus, an ImAFM approach reveals the force quadratures in the full $h - A$ plane and not along a specific path.

The single cycle analysis has been tested on simulated data and was used to generate generate $F_I(h, A)$ and $F_Q(h, A)$ maps from ImAFM approach measurements.

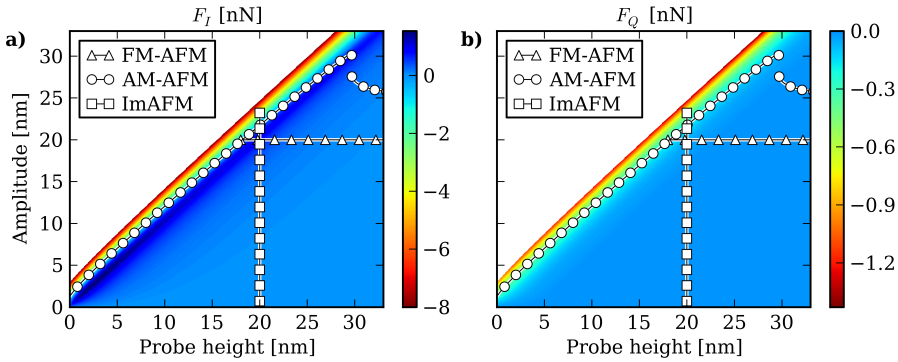

Figure 4.5: Model $F_I(h, A)$ and $F_Q(h, A)$ maps for the vdW-DMT force with exponential damping. The displayed measurement paths correspond to a frequency-shift–distance curve in FM-AFM, an amplitude–phase–distance curve in AM-AFM and an ImAFM measurement. For the FM-AFM measurements it is assumed that the dependence of the force quadratures on the frequency shift can be neglected. In contrast to FM-AFM and AM-AFM, the static probe height is constant during an ImAFM measurement and the h–A plane is explored along a path parallel to the A axis. One should also note the amplitude jump along the AM-AFM path at a probe height of $h = 30$ nm.

Chapter 5

Force reconstruction methods

One of the most important goals in dynamic AFM is the determination of the tip-surface force from the measured tip motion. However, even with the advent of multifrequency AFM and the new data channels for characterizing the tip-sample interaction, force reconstruction remains an ill-posed problem. Certain assumptions about the tip-surface force are required for reconstruction from the measured data. Depending on the type of assumption, different reconstruction methods can be used. In what follows we describe two main types of force reconstruction methods applicable to different data representations.

5.1 Approximative reconstruction methods

Force reconstruction in AFM requires an accurate measurement of the tip motion including the conversion factor between the measured photodiode signal of the optical lever system and the tip position, and the cantilever's linear response function. The result of a measurement can be expressed with different physical quantities, like the amplitude and phases of the spectral components in the force spectrum or the force quadratures introduced in 4.3. Approximative force reconstruction methods are based on a parametrized model of the tip-surface force implying a relation between the force model parameters and the considered physical quantities. Through this relation the force model parameters are determined such that the physical quantities calculated from the model parameters best approximate the measured physical quantities.

Clearly, the choice of the force model used for the reconstruction is crucial with approximative methods. The number of model parameters should not be bigger than the number of measured physical quantities and the force model should be able accurately represent the real tip-surface force. Hence, it is important to to understand the expected nature of the tip-surface force. For example, from the discussion in 4.2, complicated hysteretic force models can be excluded for narrow-band AFM at fixed static probe height. Depending on the type of force model either

linear or nonlinear approximation algorithms have to be used as detailed below.

5.1.1 Linear approximative methods

A force model is called linear if the physical quantities of interest are linear in the model parameters. Mathematically, this means that the physical quantities q_i are a linear combinations of the model parameters p_n of finite degree M,

$$q_i = \sum_{n=0}^{N} p_n \Theta_n \{z(t)\} \tag{5.1}$$

where each parameter is weighted by a functional Θ_n depending on the tip motion. The parameters p_n can then be determined algebraically from the measured physical quantities.

The idea of linear approximative force reconstruction methods can be nicely illustrated with the assumption that the tip-surface force is a purely conservative force given by a polynomial[111, 112, 113]

$$F_{\mathrm{ts}}(z) = \sum_{n=0}^{M} p_n z^n. \tag{5.2}$$

Moreover, the tip motion is fully described by the finite vector $\mathbf{z}$ of discretely sampled values of the continuous tip motion $z(t)$, which implies that the tip motion is periodic and band-limited. The vector $\mathbf{f}$ contains the values of F_{ts} at the discrete sampling points in time and is given by

$$\mathbf{f} = \mathbf{H}\mathbf{p} \tag{5.3}$$

where $\mathbf{p}$ is the vector of the polynomial coefficients p_n and the matrix $\mathbf{H}$ is computed from the tip motion as

$$\mathbf{H} = \begin{pmatrix} \mathbf{z}^0 & \mathbf{z}^1 & \mathbf{z}^2 & \cdots & \mathbf{z}^M \end{pmatrix}. \tag{5.4}$$

Experimentally only the Fourier components of the force in a narrow band around resonance are accessible. To account for this fact we multiply equation (5.3) with a unitary matrix $\mathbf{F}$ performing a DFT and with a diagonal windowing matrix $\mathbf{W}$

$$\mathbf{WFf} = \mathbf{WFHp} \tag{5.5}$$

for which we introduce the notation

$$\hat{\mathbf{f}}_W = \hat{\mathbf{H}}_W \mathbf{p} \tag{5.6}$$

This relation is a special case of equation (5.1). The measured physical quantities are spectral components of the force and the model parameters are the polynomial coefficients. The matrix $\hat{\mathbf{H}}_W$ establishes the relation between the model parameters

and the considered physical quantities. However, it is not possible to say generally if a unique solution for $\mathbf{p}$ exists which satisfies equation (5.6). Therefore, we use the pseudo-inverse $\hat{\mathbf{H}}_W^+$ of the matrix $\hat{\mathbf{H}}_W$ to solve equation (5.6) for the coefficient vector $\mathbf{p}$,

$$\mathbf{p} = \hat{\mathbf{H}}_W^+ \hat{\mathbf{f}}_W. \tag{5.7}$$

Taking into account the external drive forces which can be determined from the measured free motion far away from the surface $\mathbf{z}_{\text{free}}$ and the discrete linear response function $\hat{\mathbf{X}}$, equation (5.7) becomes

$$\mathbf{p} = \hat{\mathbf{H}}_W^+ \hat{\mathbf{X}}_W^{-1} \left(\hat{\mathbf{z}} - \hat{\mathbf{z}}_{\text{free}} \right). \tag{5.8}$$

Equation (5.8) is the final polynomial force reconstruction equation and it can be extended to more complicated polynomial force models. One possible extension is the inclusion of a position-dependent damping force.

The matrix $\hat{\mathbf{H}}_W$ is determined by Fourier transforming the Vandermonde-like matrix $\mathbf{H}$ (see equation (5.4)). Alternatively, the matrix $\hat{\mathbf{H}}_W$ can be computed directly in the Fourier domain from successive convolutions of the measured tip-motion spectrum $\hat{\mathbf{z}}$. In both cases care should be taken to avoid aliasing or circular convolution artifacts when numerically determining the matrices $\mathbf{H}$ and $\hat{\mathbf{H}}_W$. Moreover, before pseudo-inversion the matrix $\hat{\mathbf{H}}_W$ should be carefully pre-conditioned to improve the numerical stability of the algorithm. The pre-conditioning can be efficiently implemented by rescaling time and position coordinates. Moreover, since most linear algebra routines are defined for real-valued matrices, it is advisable to combine the real and imaginary part of the complex-valued equation (5.8) into one real-valued equation.

Even with perfect numerical treatment of a dual drive scheme a problem arises which is illustrated in figure 5.1. For the matrix $\hat{\mathbf{H}}_W$ shown in figure 5.1a the result of the multiplication $\hat{\mathbf{H}}_W \mathbf{p}$ does not depend on the even order coefficients of $\mathbf{p}$. Thus, the even polynomial coefficients cannot be determined by the application of the corresponding pseudo-inverse $\hat{\mathbf{H}}_W^+$ shown in figure 5.1b. However, there is no physical reason why the even order coefficients should be zero.

One possible solution is the use of a different drive scheme as the scheme defined by equation (3.12) which creates even and odd order IMPs close to resonance[111]. Another solution utilizes additional knowledge of the tip-surface interaction. In most cases the tip-surface force is localized close to the surface and goes quickly to zero further away from the surface. Thus, for sufficiently large oscillation amplitudes the even order polynomial coefficients can be determined from the assumption that the force is zero over a finite interval ending at the maximum tip deflection. This procedure is illustrated in figure 5.2 and can be expressed in matrix notation as

$$\mathbf{H}_{\text{even}} \mathbf{p}_{\text{even}} = -\mathbf{H}_{\text{odd}} \mathbf{p}_{\text{odd}} \tag{5.9}$$

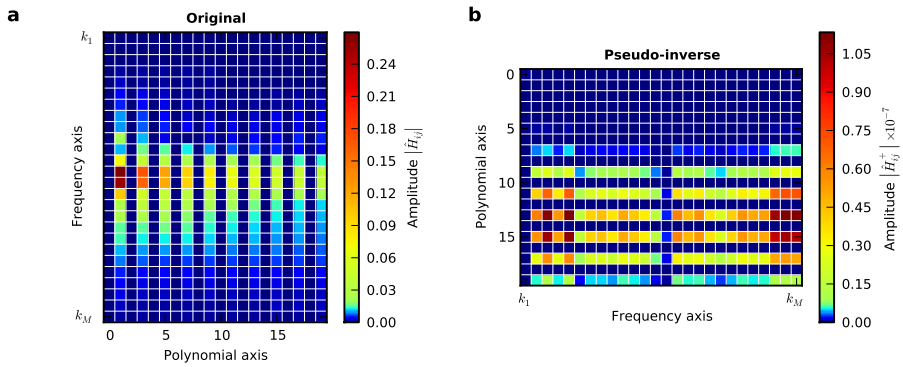

Figure 5.1: The absolute values of an example matrix $\hat{\mathbf{H}}_W$ (a) and its pseudo-inverse $\hat{\mathbf{H}}^{+}_W$. The matrices have been computed from an ImAFM measurement on a polystyrene sample in the repulsive regime.

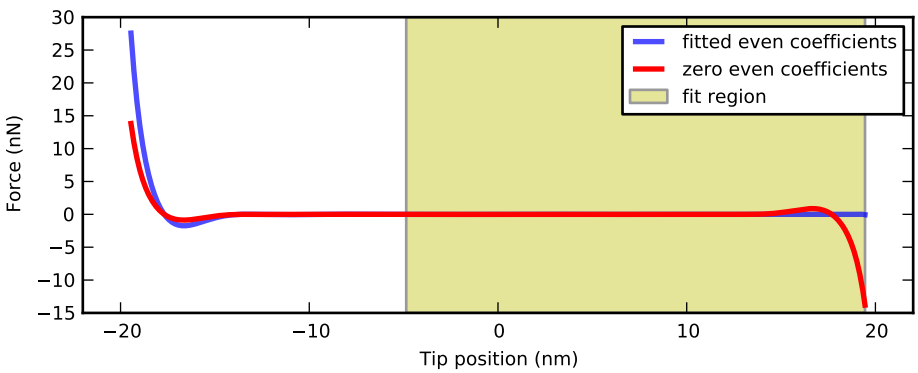

Figure 5.2: Determination of the even order polynomial coefficients for experimental data obtained from an ImAFM measurement on a polystyrene surface. The polynomial with odd symmetry (red) curve was obtained by using equation (5.8). The final polynomial reconstruction (blue) has the same odd order coefficients as the red curve and the even order coefficients have been determined from the assumption that the force is zero in the shaded region.

where $\mathbf{p}_{\text{even}}$ and $\mathbf{p}_{\text{odd}}$ are the even and odd order coefficient vectors respectively and the matrices $\mathbf{H}_{\text{even}}$ and $\mathbf{H}_{\text{odd}}$ are given by

$$\mathbf{H}_{\text{even}} = \begin{pmatrix} \mathbf{z}_{\text{fit}}^0 & \mathbf{z}_{\text{fit}}^2 & \cdots & \mathbf{z}_{\text{fit}}^{M-1} \end{pmatrix} \tag{5.10}$$

$$\mathbf{H}_{\text{odd}} = \begin{pmatrix} \mathbf{z}_{\text{fit}}^1 & \mathbf{z}_{\text{fit}}^3 & \cdots & \mathbf{z}_{fit}^{M} \end{pmatrix} \tag{5.11}$$

for a suitable vector $\mathbf{z}_{\text{fit}}$ and M odd.

The polynomial reconstruction method can readily be adapted for the application to force quadrature data instead of raw spectral force data, illustrating the generality of approximative reconstruction methods for applications on different measured physical quantities. This linear approximative method has been tested has been tested on simulated data and applied to experimental data generating high-resolution surface stiffness maps.

5.1.2 Nonlinear approximative methods

Linear force models are only a small subset of all possible force models. In fact, for most standard models of tip-surface interactions the relation between the considered physical quantities and the model parameters is nonlinear. For such models algebraic solutions do not exist in general and numerical methods must be used to find the optimal model parameters[50].

In the context of ImAFM Daniel Forchheimer developed a numerical method for determining surface properties[114]. The method is based on minimizing the total least square error between the measured force spectrum and the force spectrum created by an arbitrary force model for the measured tip motion. During the minimization process the force model parameters are adjusted by a Levenberg–Marquardt algorithm which interpolates between the Gauss–Newton algorithm and the method of gradient descent. Other optimization algorithms like the nonlinear simplex algorithm, stochastic annealing, parameter space girding or combinations of them can might be used to improve the quality of the minimization since the Levenberg–Marquardt algorithm finds only local minima and is thus very dependent on the given initial conditions. However, for the data studied we found, that the total error as a function of the model parameters was a continuous function with only one minimum and in this case the Levenberg–Marquardt algorithm offers good performance.

Numerical approximative methods have several advantages over linear methods. With numerical methods essentially any kind of force model can be used, including models like piecewise-defined forces or hysteretic forces which are difficult to treat analytically. Models with long range interactions can be investigated and in reference to the discussion in 5.1.1 the assumption of a force localized to the surface might be readily exchanged for an assumed long-range behaviour of the force[115]. The numerical methods can also be applied to linear force models for which they ideally would give the same result as linear methods. However, we found that the performance of numerical solver was worse than the algebraic pseudo-inversion in

these cases. Furthermore, numerical methods do not require extensive mathematical modeling for finding analytic relations between the measured physical quantities and the force parameters. Moreover, the obtained surface force parameters usually have a physical meaning like sample stiffness or adhesion, giving a direct interpretation for each single parameter.

On the other hand the standard force models often rely in very idealized assumptions about the interaction geometry between the tip and the surface. Often further knowledge about the tip-radius is required. In this context of finding the right force model it can be difficult to judge the applicability of a force model and the quality of the optimization from the force parameters obtained, since numerical methods always return a set of parameters which are optimal for any model used. Therefore, the validity of a specific force model has to be carefully checked and different models might be required for different regions on the sample surface. However, due to their ease of implementation and their straight-forward interpretation, numerical nonlinear approximative methods for force reconstruction are a very useful tools for qualitative and quantitative surface analysis.

5.2 Integral reconstruction methods

As stated in in chapter 4 the measured physical quantities in multifrequency AFM are inherently integral quantities as they are derived from spectral data involving Fourier integrals. The integral character of the physical quantities implies they can be expressed as an integral equation relating them with the tip-surface force. Integral reconstruction techniques thus aim to invert this integral relation between force and measured physical quantities to reconstruct the force. In order to do so the tip-surface force is assumed to be a function depending on one or more variables. Depending on the choice of variables, different methods are used for force reconstruction.

5.2.1 Amplitude-dependence force spectroscopy

One of the most simple functional representation of the tip-surface force is a function depending only on the tip-position. In this case the tip-surface force is purely conservative and can be written as

$$F_{\mathrm{ts}} = F_{\mathrm{c}}(z) \tag{5.12}$$

For a purely conservative force of this type the force F_Q, which is quadrature to the harmonic motion ($\pi/2$ phase shifted), is equal to zero and by a substitution of variables the in-phase force quadrature F_I can be written as[85, 110]

$$F_I(A, h, \bar{\omega}) = \frac{1}{\pi} \int_{-A}^{A} F_{\mathrm{c}}(z' + h) \frac{z'/A}{\sqrt{A^2 - z'^2}} dz' \tag{5.13}$$

In the following we consider F_I as a function of the oscillation amplitude only. By assuming that the maximum oscillation amplitude is at least two times bigger than the decay length of the tip-surface force and, introducing $\tilde{A} = A^2$, $\tilde{F}_I(\tilde{A}) = -2\pi F_I\left(\sqrt{\tilde{A}}\right)$ and $\tilde{F}_c(u) = F_c(-\sqrt{u}+h)$ equation (5.13) becomes

$$\tilde{F}_I(\tilde{A}) \approx \int_0^{\tilde{A}} \frac{\tilde{F}_c(u)}{\sqrt{\tilde{A}-u}} du. \tag{5.14}$$

Equation (5.14) reveals that the in-phase force quadrature is the Abel transform of the tip-surface interaction[116]. The Abel transform $\mathcal{A}$ of a function f is defined as

$$(\mathcal{A}f)(x) = \int_0^x \frac{f(t)}{\sqrt{x-t}} dt. \tag{5.15}$$

The Abel transform of a differentiable function has a unique inverse which can be determined either by solving equation (5.15) in Laplace space, or from the fact that

$$\mathcal{A}^2 f(x) = \pi F(x) \tag{5.16}$$

where F is the antiderivative of f (see A.2). Hence, the inverse of the Abel transform is simply given by

$$\mathcal{A}^{-1} = \frac{1}{\pi}\mathcal{D}\mathcal{A}. \tag{5.17}$$

where $\mathcal{D}$ is the derivative operator. The application of $\mathcal{A}^{-1}$ to equation (5.14) yields

$$\tilde{F}_c(u) = \frac{1}{\pi}\frac{d}{du}\int_0^u \frac{\tilde{F}_I(\tilde{A})}{\sqrt{u-\tilde{A}}} d\tilde{A} \tag{5.18}$$

allowing reconstruction of the conservative part of the tip-surface from the amplitude dependence of the in-phase force F_I.

For a position-dependent damping force of the form

$$F_{nc}(z, \dot{z}) = \lambda(z)\dot{z} \tag{5.19}$$

the damping curve $\lambda(z)$ is obtained in a similar manner from the amplitude dependence of the out-of-phase quadrature F_Q[110]. At oscillation frequency $\bar{\omega}$ we define $\tilde{F}_Q(\tilde{A}) = -(2\pi\sqrt{\tilde{A}}/\bar{\omega})F_Q(\sqrt{\tilde{A}})$ and $\tilde{\lambda}(u) = \lambda(-\sqrt{u}+h)/\sqrt{u}$ so that the force quadrature integral can be written as

$$\tilde{F}_Q(\tilde{A}) \approx \int_0^{\tilde{A}} \tilde{\lambda}(u)\sqrt{\tilde{A}-u} du \tag{5.20}$$

which has the solution

$$\tilde{\lambda}(u) = \frac{2}{\pi}\frac{d^2}{d\tilde{A}^2}\int_0^u \frac{\tilde{F}_Q(\tilde{A})}{\sqrt{u-\tilde{A}}} d\tilde{A} \tag{5.21}$$

Since both the conservative force and the position-dependent damping have been reconstructed by considering the amplitude dependence of the force quadratures F_I and F_Q while keeping the static probe height h, constant the method of force reconstruction is called amplitude-dependence force spectroscopy (ADFS). The integrals that appear in ADFS are structurally similar to integrals that have been considered before in the literature[40, 41, 39, 44, 45]. However, apart from[117], ADFS is the first integral force reconstruction methods in which the static probe height is kept constant.

Equation (5.18) implies that ADFS requires the integration over the $F_I(A)$ curve as a single-valued function of the amplitude. However, due to the presence of noise in the experimental data, the $F_I(A)$ curves are never single valued when the value if F_I is measured twice during an ImAFM measurement, such as a beating tip motion with an amplitude that first increases and then decreases again. In most cases the deviations of the measured F_I values are small as shown in figure 5.3a. However, when imaging a surface sudden turning points and loops can occur on the measured $F_I(A)$ curve. The curve in figure 5.3b is an extreme example of such behaviour. Since $F_I(A)$ curves determined from ImAFM approach measurements generally do not show sudden turning points, we attribute their appearance in imaging data as the result of the feedback system which is constantly working while scanning. Small changes of the static probe height can appear as significant changes in the $F_I(A)$ curves and thus small feedback errors can have a big effect on the measured data, especially in the repulsive regime. We observed that the feedback signal computed by the FPGA is most constant during the amplitude increase of the tip's oscillation amplitude. During this time the $F_I(A)$ curve also exhibits fewer discontinuities. Therefore, for applying ADFS to imaging data we only use F_I data for which the oscillation amplitude is increasing. The ability to specifically select certain parts of the measured force data based on time domain constraints is actually one strength of the force quadrature data representation.

Together with the ability of ImAFM to rapidly measure the amplitude dependence of the force quadratures F_I and F_Q, force measurements with ADFS are at least one order of magnitude faster than with conventional methods based on a slow change of the static probe height. ImAFM measurements are easily performed during imaging and ADFS together with ImAFM allow for the combination of high-resolution imaging and high-accuracy force measurements in a single scan. ADFS and ImAFM thus provide a solution to a long-standing problem in the field of AFM. Moreover, ImAFM and ADFS do not require special cantilevers and are compatible with most existing AFM platforms. ADFS was tested on both simulated data and in experiments where it generate high-resolution surface property maps and enabled a critical analysis of standard model of the tip-surface interaction[85].

5.2.2 Atomic force tomography

Even though the forces experience by the tip in dynamic AFM can be complicated functions of multiple variables conventional force reconstruction methods are

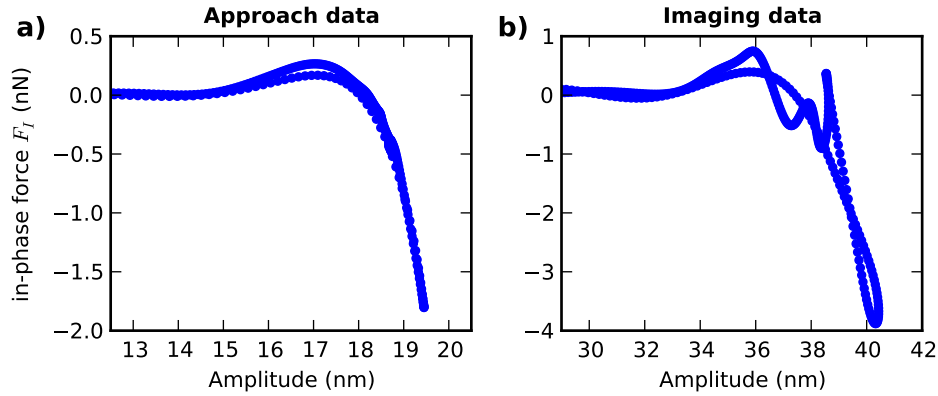

Figure 5.3: During the approach measurement there are small deviations between the $F_I(A)$ curve where the oscillation amplitude increased and where the amplitude decreased (a). When imaging a surface with ImAFM the $F_I(A)$ curve can exhibit sharp turning points and loops when the amplitude decreases (b).

based on quite simplistic functional representations of the force, like purely position-dependent forces and damping. No attempt has been undertaken to expand the possibilities of force reconstruction beyond purely position-dependent functions to reconstruct for example force disks (see figure 4.2). However, there is an interesting connection between ADFS and the Fourier projection slice theorem which indicates that there exists a connection to more general reconstruction techniques. Geometrically the Abel transform can be interpreted as projection of a two-dimensional circularly symmetrically function along parallel lines. For two dimensional circularly symmetric function the Abel transform is, moreover, part of the so-called Fourier-Hankel-Abel (FHA) cycle which means that a Abel transform $\mathcal{A}$ of the two dimensional function followed by a Fourier transform $\mathcal{F}$, is equivalent to a zeroth order Hankel transform $\mathcal{H}^{(0)}$ of the original function. In operator notation this relation between the transforms can be expressed as

$$\mathcal{F}\mathcal{A} = \mathcal{H}^{(0)} \tag{5.22}$$

which is in turn a special case of the projection-slice theorem depicted in figure 5.4. This general theorem states that for a two-dimensional function $f(x, y)$ the projection $\mathcal{P}_1$ of the original function onto a one dimensional line followed by a one dimensional Fourier transform $\mathcal{F}_1$ is equivalent to a slice $\mathcal{S}_1$ through the origin of the two-dimensional Fourier transform $\mathcal{F}_2$ of the original function,

$$\mathcal{F}_1\mathcal{P}_1 f(x, y) = \mathcal{S}_1\mathcal{F}_2 f(x, y). \tag{5.23}$$

The Fourier projection slice theorem is closely related to the Radon transform

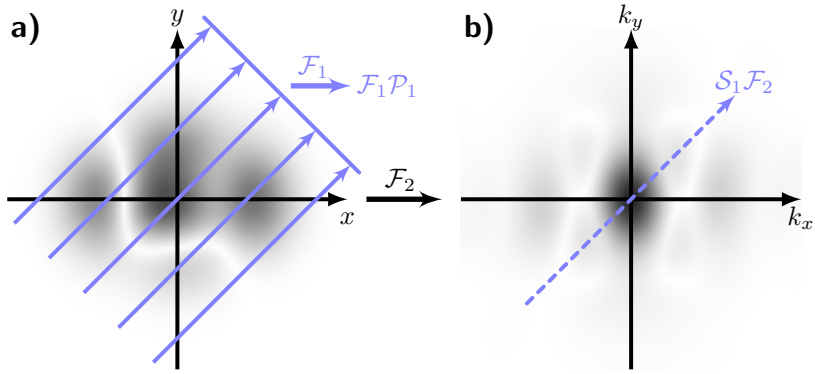

Figure 5.4: The projection $\mathcal{P}_1$ of a two dimensional function $f(x, y)$ yields a one dimensional function (a) whose Fourier transform $\mathcal{F}_1$ equals a slice $\mathcal{S}_1$ of the two dimensional Fourier transform of the original function (b). The slice goes through the origin and makes the same angle with the k_x as the projection lines with the x axis.

which forms the mathematical backbone of computed tomography (CT). In CT a patient's body is imaged from different angles with x-rays and the inverse Radon transform is used to reconstruct the three dimensional internal structure of the body from the recorded two dimensional x-ray images. Mathematically, the body can be considered as an x-ray attenuation factor which is a function of position in the body. The (forward) Radon transform is defined as the integration or projection of the attenuation function along parallel lines as depicted in figure 5.5a. Thus, x-ray imaging in CT can be considered as computing the Radon transform of the body's x-ray attenuation, and the basic mathematical problem is to invert this transform, or find the attenuation factor from line integrals through it.

Early in the history of CT it was realized that the integration along straight lines is not the only possible geometry for tomography[118]. A variation of the conventional Radon transform is the circular Radon transform in which the integrals are line integrals over closes spheres which is illustrated for two dimensions in figure 5.5b. The projections are characterized by the radius of the sphere and its center which are usually located on a hyperplane or a closed surface[119, 120]. This type of tomography problem is encountered for example in synthetic aperture radar (SAR)[121] or sonar[122]. In sonar for example a submarine moves along a straight line while it sends out sound pulses. The sound pulses have a much higher velocity than the submarine which measures the echo due to reflected sound waves. The sound sensor has no directional sensitivity such that the measured echo signal is the accumulated reflection from a sphere centered at the submarine. The sphere's radius is determined from the time delay between sent pulses and the measured echo. By measuring many echos as the submarine moves forward, an image of the

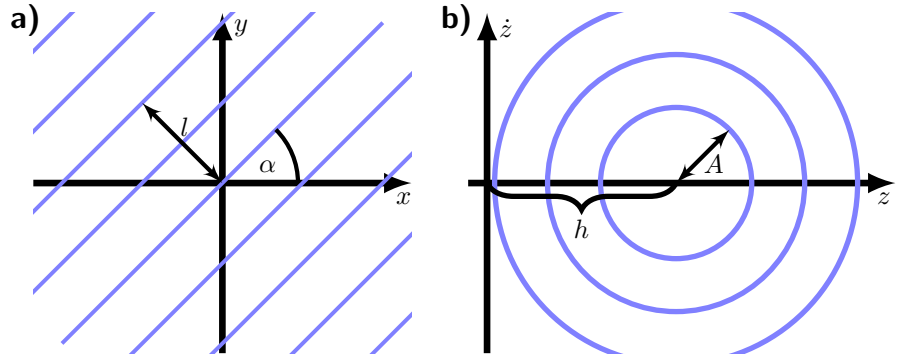

Figure 5.5: The normal Radon transform integrates a two dimensional function along parallel straight lines (a). Each line is characterized by the angle between the line and the x axis and the shortest distance between the line and the origin. The circular Radon transform is based integration along circular paths (b) which are described by their radius and the distance of the center of the circle to the origin.

surrounding sound reflectivity is generated.

The data collection in sonar is very similar to that of an ImAFM approach measurement. As the static probe height is slowly changed the tip performs a sinusoidal motion moving on a circular orbit in phase space. The measured force quadrature data corresponds to the line integral of the force along the circular orbit in phase space. The radius of the force line integrals is given by the instantaneous oscillation amplitude and the centers are moved along the position axes by changing the static probe height. However, in contrast to the circular Radon transform, the line integrals contain a weight factor because they represent Fourier integrals or Fourier coefficients of the force at the oscillation frequency.

For the sake of discussion we rescale and mirror the original two dimensional force such that

$$F_{\mathrm{ts}}(z,\dot{z}) = f_{\mathrm{ts}}(z,-\dot{z}/\bar{\omega}) \tag{5.24}$$

and we continue to decompose the tip-surface interaction into an effective conservative part f_{c} and an effective non-conservative part f_{nc},

$$f_{\mathrm{ts}}(z,\dot{z}) = f_{\mathrm{c}}(z,\dot{z}) + f_{\mathrm{nc}}(z,\dot{z}) \tag{5.25}$$

The conservative force is symmetric in $\dot{z}$ whereas the non-conservative force is anti-symmetric in $\dot{z}$. With these assumptions the in-phase force quadrature F_I can be written as a function of static probe height h and oscillation amplitude A as

$$F_I(h,A) = \frac{1}{2\pi}\int_0^{2\pi} f_{\mathrm{c}}\left(A\cos(\theta)+h, A\sin(\theta)\right)\cos(\theta)d\theta \tag{5.26}$$

Substituting in the two dimensional Fourier transform of the force equation (5.26) can be written as

$$\begin{aligned} F_I(h,A) &= i\int_{-\infty}^{\infty}\int_{-\infty}^{\infty} f_{\mathrm{c}}^{(\mathcal{F},\mathcal{F})}(k_x,k_y)\cos\left(\psi(k_x,k_y)\right) \\ &\quad \times J_1\left(\sqrt{k_x^2+k_y^2}A\right)e^{ik_x h}dk_x dk_y \end{aligned} \tag{5.27}$$

where i is the complex unit and the superscript $(\mathcal{F},\mathcal{F})$ indicates that $f_{\mathrm{c}}^{(\mathcal{F},\mathcal{F})}$ is the Fourier transform of f_{c} in both variables (see A.3). The phase function ψ is given by

$$\psi(k_x,k_y) = \operatorname{atan2}(k_x,k_y) - \frac{\pi}{2} \tag{5.28}$$

and J_1 is the first Bessel function of first kind. Applying a Fourier transform $\mathcal{F}$ in the first argument of F_I and a first Hankel transform $\mathcal{H}^{(1)}$ in the second argument of F_I equation (5.27), becomes

$$F_I^{\left(\mathcal{F},\mathcal{H}^{(1)}\right)}(k,\lambda) = \frac{2i}{\sqrt{\lambda^2-k^2}}\cos\left(\psi\left(k,\sqrt{\lambda^2-k^2}\right)\right) f_{\mathrm{c}}^{(\mathcal{F},\mathcal{F})}\left(k,\sqrt{\lambda^2-k^2}\right) \tag{5.29}$$

where we have used the fact that $f_{\mathrm{c}}^{(\mathcal{F},\mathcal{F})}(k_x,k_y)$ is symmetric in k_y. A similar relation between F_Q and the non-conservative force f_{nc} can be derived,

$$F_Q^{\left(\mathcal{F},\mathcal{H}^{(1)}\right)}(k,\lambda) = \frac{2i}{\sqrt{\lambda^2-k^2}}\sin\left(\psi\left(k,\sqrt{\lambda^2-k^2}\right)\right) f_{\mathrm{nc}}^{(\mathcal{F},\mathcal{F})}\left(k,\sqrt{\lambda^2-k^2}\right) \tag{5.30}$$

Equations (5.29) and (5.30) reveal that the Fourier-Hankel transforms of the force quadrature maps (see figure 4.5) are directly related to the two dimensional Fourier transforms of the conservative and non-conservative force respectively. The functions $\cos(\psi)$ and $\sin(\psi)$ are shown in figure 5.6 and they have the effect of filtering of the original force in Fourier space. For the conservative force, any component which is purely directed in the $\dot{z}$ direction of the force is filtered out, while the sensitivity increases for force components which are directed in the z direction. For the non-conservative part of the force the situation is just opposite (see figure 5.6). The fact that both filter functions are zero in one direction implies that the force quadrature can not be used to reconstruct arbitrary completely forces. However, for physical forces there are good reasons to assume that the force components that are filtered out by $\cos(\psi)$ and $\sin(\psi)$ are zero anyway. The force inversion equations are then given by

$$f_{\mathrm{c}}^{(\mathcal{F},\mathcal{F})}(k,\rho) = \frac{|\rho|}{2i}\frac{F_I\left(k,\sqrt{\rho^2+k^2}\right)}{\cos\left(\psi(k,|\rho|)\right)} \quad \text{for } \cos\left(\psi(k,|\rho|)\right)\neq 0 \tag{5.31}$$

$$f_{\mathrm{nc}}^{(\mathcal{F},\mathcal{F})}(k,\rho) = \frac{\rho}{2i}\frac{F_Q\left(k,\sqrt{\rho^2+k^2}\right)}{\sin\left(\psi(k,\rho)\right)} \quad \text{for } \sin\left(\psi(k,\rho)\right)\neq 0 \tag{5.32}$$

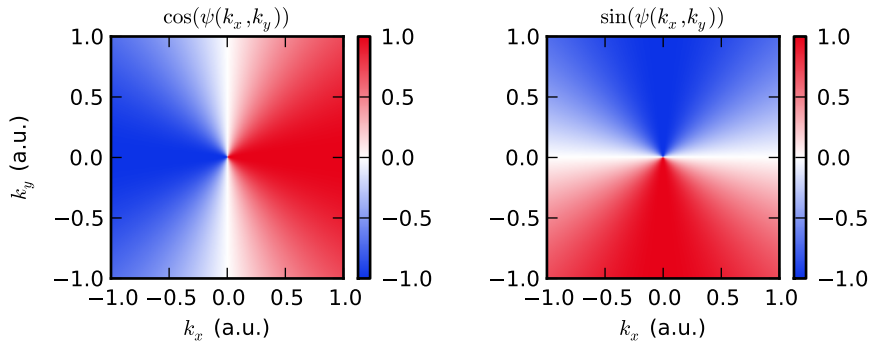

Figure 5.6: The filter functions $\cos(\psi)$ and $\sin(\psi)$. The Fourier transform of the conservative part of the force is multiplied with $\cos(\psi)$ which is symmetric in k_y while the Fourier transform of the non-conservative force is multiplied with the anti-symmetric function $\sin(\psi)$.

Equations (5.31) and (5.32) are tomographic force reconstruction equations, enabling two dimensional force reconstructions or the determination of the nonlinear dependence of force on both position an velocity. However, they suffer from the fact that they involve Fourier transforms of the force quadrature data over infinite domains. In real experiments the force quadratures can only be determined over finite or at least semi-finite domains. Therefore, the construction of a local tomography operator is required for application on experimental data. The field of tomography developed different methods for the construction of such an operator by for example using pseudo-inverse methods[123] or the expansion of the original function in terms of localized functions such as wavelets[124, 125] as opposed to of de-localized plane waves. Alternatively, a discretization of the problem or the use of the uni-literal Laplace transform could provide another method to improve the quality of the reconstruction from finite data.

Chapter 6

Conclusions and outlook

Physics is often concerned with predicting the response of a system when it is subject to an known excitation. Here, we focused on the inverse problem of determining the excitation that acts on a system by studying the system response. We chose the harmonic oscillator as the system of interest as it is one of the most widely used model systems in physics and has applications in many different areas. Dynamic AFM is one example whose physics is described by the harmonic oscillator. The high quality factor of the oscillator significantly limits the extractable information about the tip-surface interaction . To increase the amount of measurable information in dynamic AFM we developed ImAFM which utilizes the nonlinear tip-surface interaction to concentrate as much information as possible in the narrow frequency band around the cantilever resonance. We established and implemented the accurate measurement of amplitude and phase in a multifrequency AFM. We performed imaging and approach measurements on different samples showing that the intermodulation response of the tip depends on the tip-sample interaction.

ImAFM is part of the recent development in AFM exploring multifrequency drive and detection schemes. However, as more data is acquired, multifrequency AFM measurements require more complicated analysis. Therefore, new analysis tools are required which allow for a more direct interpretation of the measured data in multifrequency AFM. One question that immediately arises in dynamic AFM the completeness of representation of the tip-surface force. One dimensional force curves are clearly inadequate, so we introduce the force disk as a more complete description of surface forces while scanning at constant height. Within the force disk picture we are able to illuminate the fundamental limits of narrow-band AFM. Moreover, the notion of an oscillation envelope function allows for an analysis of single oscillation cycles in narrow-band ImAFM and for an interpretation of the ImAFM measurement as an rapid measurement of the amplitude-dependence of two force quadratures. We note that the force quadratures are not only functions of the static probe height but also of oscillation amplitude and frequency. This observation allows us to represent the data of ImAFM approach measurements as

force quadrature maps.

However, one of the most important goals in dynamic AFM is the reconstruction of the force between the tip and the surface from the measured data. This reconstruction is an ill-posed inverse problem since the measured force spectrum is incomplete. We introduce two different types of methods to mitigate this problem. Approximative reconstruction methods assume a specific model for the tip-surface interaction and, depending on the model, algebraic linear reconstruction methods or numerical nonlinear methods are applied for determining the parameters of the force model. Linear models such as polynomial force models are simple to understand while still allowing for a wide range of different surface forces. On the other hand nonlinear models provide a direct physical interpretation of the model parameters. Integral methods aim to reconstruct the tip-surface interaction without model assumptions. We use ADFS together with ImAFM to combine high-speed high-resolution imaging with accurate force measurements. Furthermore, we explore a connection to tomographic reconstruction methods and introduce atomic force tomography which adds a new dimension to force measurements in dynamic AFM.

In the future, we anticipate that methods from the well-established field of tomography will appear in the field of AFM and help to construct a localized atomic force tomography reconstruction operator. In the work presented here we focused on ImAFM using only one narrow frequency band and one of the most simple drive schemes. However, an AFM cantilever has multiple eigenmodes which may be simultaneously excited either by driving externally or by the tip-surface interaction in highly damped environment such as liquids. Multi-modal ImAFM requires new methods for analyzing the measured motion but will also provide a deeper insight into the tip-surface interaction. Important problems in this context are the search for new multi-frequency drive signals optimized for different for high signal-to-noise ratio force measurements and the experimental implementation of ImAFM based on frequency shift measurements. Moreover, new feedback schemes for higher spatial resolution , higher scan speed and lower back-action on the sample are of interest in the future.

Bibliography

[1] *Langenscheidts Taschenwörterbuch Latein.* Langenscheidt, 54 edition, 2003.

[2] N. Copernicus. *De revolutionibus orbium coelestium.* Johannes Petreius, Nürnberg, 1543.

[3] H. Berger. *Über das Elektrenkephalogramm des Menschen.* Archiv für Psychiatrie und Nervenkrankheiten, **87**, 527–570, 1929.

[4] R. Owen. *Report to the Committee of the Association for the Relief of the Manufacturing Poor.* 1817.

[5] J. C. L. de Sismondi. *Nouveaux Principes d'économie politique.* 1819.

[6] B. Belousov. *Periodically acting reaction and its mechanism.* Collection of Abstracts on Radiation Medicine, **147**, 145, 1959.

[7] A. Zhabotinsky. *Periodical process of oxidation of malonic acid solution.* Biophysics, **9**, 306–311, 1964.

[8] B. Pontecorvo. *Mesonium and anti-mesonium.* Soviet Journal of Experimental and Theoretical Physics, **6**, 429, 1957.

[9] D. Keown. *Buddhism: A Very Short Introduction.* Oxford University Press, 1 edition, 2001.

[10] J. Hemleben. *Galilei, Galileo.* rororo, 20 edition, 1969.

[11] William Thomson (Lord Kelvin) and P. Guthrie. *Resolution of Forces Effective Component.* In *Treatise on Natural Philosophy.* Cambridge University Press, 1879.

[12] Q. Zheng and Q. Jiang. *Multiwalled Carbon Nanotubes as Gigahertz Oscillators.* Physical Review Letters, **88**(4), 045503, 2002.

[13] A. D. O'Connell, M. Hofheinz, M. Ansmann, R. C. Bialczak, M. Lenander, E. Lucero, M. Neeley, D. Sank, H. Wang, M. Weides, J. Wenner, J. M. Martinis and A. N. Cleland. *Quantum ground state and single-phonon control of a mechanical resonator.* Nature, **464**(7289), 697–703, 2010.

[14] J. D. Teufel, T. Donner, D. Li, J. W. Harlow, M. S. Allman, K. Cicak, A. J. Sirois, J. D. Whittaker, K. W. Lehnert and R. W. Simmonds. *Sideband cooling of micromechanical motion to the quantum ground state.* Nature, **475**(7356), 359–363, 2011.

[15] F. Huber, H. P. Lang, N. Backmann, D. Rimoldi and C. Gerber. *Direct detection of a BRAF mutation in total RNA from melanoma cells using cantilever arrays.* Nature nanotechnology, **8**(2), 125–9, 2013.

[16] J. Chaste, A. Eichler, J. Moser, G. Ceballos, R. Rurali and A. Bachtold. *A nanomechanical mass sensor with yoctogram resolution.* Nature nanotechnology, **7**(5), 301–4, 2012.

[17] R. García. *Dynamic atomic force microscopy methods.* Surface Science Reports, **47**(6-8), 197–301, 2002.

[18] J. Fourier. *Mémoire sur la propagation de la chaleur dans les corps solides.* Nouveau Bulletin des sciences par la Société philomatique de Paris I, **6**, 215–221, 1808.

[19] A. Einstein. *Über die von der molekularkinetischen Theorie der Wärme geforderte Bewegung von in ruhenden Flüssigkeiten suspendierten Teilchen.* Annalen der Physik, **322**(8), 549–560, 1905.

[20] R. Kubo. *Statistical-Mechanical Theory of Irreversible Processes. I. General Theory and Simple Applications to Magnetic and Conduction Problems.* Journal of the Physical Society of Japan, **12**(6), 570–586, 1957.

[21] G. Binnig, C. F. Quate and C. Gerber. *Atomic Force Microscope.* Physical Review Letters, **56**(9), 930–933, 1986.

[22] F. Ohnesorge and G. Binnig. *True atomic resolution by atomic force microscopy through repulsive and attractive forces.* Science, **260**(5113), 1451–6, 1993.

[23] P. K. Hansma, J. P. Cleveland, M. Radmacher, D. A. Walters, P. E. Hillner, M. Bezanilla, M. Fritz, D. Vie, H. G. Hansma, C. B. Prater, J. Massie, L. Fukunaga, J. Gurley and V. B. Elings. *Tapping mode atomic force microscopy in liquids.* Applied Physics Letters, **64**(13), 1738, 1994.

[24] F. J. Giessibl. *Atomic resolution of the silicon (111)-(7x7) surface by atomic force microscopy.* Science, **267**(5194), 68–71, 1995.

[25] D. Rugar, C. S. Yannoni and J. A. Sidles. *Mechanical detection of magnetic resonance.* Nature, **360**(6404), 563–566, 1992.

[26] H.-J. Butt, B. Cappella and M. Kappl. *Force measurements with the atomic force microscope: Technique, interpretation and applications.* Surface Science Reports, **59**(1-6), 1–152, 2005.

[27] F. Pérez-Murano, G. Abadal, N. Barniol, X. Aymerich, J. Servat, P. Gorostiza and F. Sanz. *Nanometer-scale oxidation of Si(100) surfaces by tapping mode atomic force microscopy.* Journal of Applied Physics, **78**(11), 6797, 1995.

[28] R. García, M. Calleja and H. Rohrer. *Patterning of silicon surfaces with noncontact atomic force microscopy: Field-induced formation of nanometer-size water bridges.* Journal of Applied Physics, **86**(4), 1898, 1999.

[29] Y. Sugimoto, M. Abe, S. Hirayama, N. Oyabu, O. Custance and S. Morita. *Atom inlays performed at room temperature using atomic force microscopy.* Nature materials, **4**(2), 156–9, 2005.

[30] L. D. Landau and E. M. Lifshitz. *Mechanics.* Pergamon, 1968.

[31] J. E. Sader. *Frequency response of cantilever beams immersed in viscous fluids with applications to the atomic force microscope.* Journal of Applied Physics, **84**(1), 64, 1998.

[32] T. R. Rodriguez and R. García. *Tip motion in amplitude modulation (tapping-mode) atomic-force microscopy: Comparison between continuous and point-mass models.* Applied Physics Letters, **80**(9), 1646, 2002.

[33] J. Melcher, S. Hu and A. Raman. *Equivalent point-mass models of continuous atomic force microscope probes.* Applied Physics Letters, **91**(5), 053101, 2007.

[34] A. San Paulo and R. García. *Tip-surface forces, amplitude, and energy dissipation in amplitude-modulation (tapping mode) force microscopy.* Physical Review B, **64**(19), 193411, 2001.

[35] T. R. Albrecht, P. Grütter, D. Horne and D. Rugar. *Frequency modulation detection using high-Q cantilevers for enhanced force microscope sensitivity.* Journal of Applied Physics, **69**(2), 668, 1991.

[36] F. J. Giessibl. *A direct method to calculate tip-sample forces from frequency shifts in frequency-modulation atomic force microscopy.* Applied Physics Letters, **78**(1), 123, 2001.

[37] J. E. Sader and S. P. Jarvis. *Accurate formulas for interaction force and energy in frequency modulation force spectroscopy.* Applied Physics Letters, **84**(10), 1801, 2004.

[38] J. E. Sader and S. P. Jarvis. *Interpretation of frequency modulation atomic force microscopy in terms of fractional calculus.* Physical Review B, **70**(1), 8–10, 2004.

[39] J. E. Sader, T. Uchihashi, M. J. Higgins, A. Farrell, Y. Nakayama and S. P. Jarvis. *Quantitative force measurements using frequency modulation atomic force microscopy - theoretical foundations.* Nanotechnology, **16**(3), S94–S101, 2005.

[40] U. Dürig. *Relations between interaction force and frequency shift in large-amplitude dynamic force microscopy.* Applied Physics Letters, **75**(3), 433, 1999.

[41] U. Dürig. *Extracting interaction forces and complementary observables in dynamic probe microscopy.* Applied Physics Letters, **76**(9), 1203, 2000.

[42] R. García and A. San Paulo. *Attractive and repulsive tip-sample interaction regimes in tapping-mode atomic force microscopy.* Physical Review B, **60**(7), 4961–4967, 1999.

[43] R. García and A. San Paulo. *Dynamics of a vibrating tip near or in intermittent contact with a surface.* Physical Review B, **61**(20), R13381–R13384, 2000.

[44] H. Hölscher. *Quantitative measurement of tip-sample interactions in amplitude modulation atomic force microscopy.* Applied Physics Letters, **89**(12), 123109, 2006.

[45] S. Hu and A. Raman. *Inverting amplitude and phase to reconstruct tip-sample interaction forces in tapping mode atomic force microscopy.* Nanotechnology, **19**(37), 375704, 2008.

[46] M. Lee and W. Jhe. *General Theory of Amplitude-Modulation Atomic Force Microscopy.* Physical Review Letters, **97**(3), 036104, 2006.

[47] A. J. Katan, M. H. van Es and T. H. Oosterkamp. *Quantitative force versus distance measurements in amplitude modulation AFM: a novel force inversion technique.* Nanotechnology, **20**(16), 165703, 2009.

[48] R. García and E. T. Herruzo. *The emergence of multifrequency force microscopy.* Nature Nanotechnology, **7**(4), 217–226, 2012.

[49] R. W. Stark. *Bistability, higher harmonics, and chaos in AFM.* Materials Today, **13**(9), 24–32, 2010.

[50] A. Raman, S. Trigueros, A. Cartagena, a. P. Z. Stevenson, M. Susilo, E. Nauman and S. A. Contera. *Mapping nanomechanical properties of live cells using multi-harmonic atomic force microscopy.* Nature nanotechnology, **6**(12), 809–14, 2011.

[51] R. Hillenbrand, M. Stark and R. Guckenberger. *Higher-harmonics generation in tapping-mode atomic-force microscopy: Insights into the tip-sample interaction.* Applied Physics Letters, **76**(23), 3478, 2000.

[52] M. Stark, R. W. Stark, W. M. Heckl and R. Guckenberger. *Spectroscopy of the anharmonic cantilever oscillations in tapping-mode atomic-force microscopy.* Applied Physics Letters, **77**(20), 3293, 2000.

[53] S. Hembacher, F. J. Giessibl and J. Mannhart. *Force microscopy with light-atom probes.* Science, **305**(5682), 380–3, 2004.

[54] M. Stark, R. W. Stark, W. M. Heckl and R. Guckenberger. *Inverting dynamic force microscopy: from signals to time-resolved interaction forces.* Proceedings of the National Academy of Sciences of the United States of America, **99**(13), 8473–8, 2002.

[55] O. Sahin. *High-resolution imaging of elastic properties using harmonic cantilevers.* Sensors and Actuators A: Physical, **114**(2-3), 183–190, 2004.

[56] O. Sahin, S. Magonov, C. Su, C. F. Quate and O. Solgaard. *An atomic force microscope tip designed to measure time-varying nanomechanical forces.* Nature nanotechnology, **2**(8), 507–14, 2007.

[57] J. Legleiter, M. Park, B. Cusick and T. Kowalewski. *Scanning probe acceleration microscopy (SPAM) in fluids: mapping mechanical properties of surfaces at the nanoscale.* Proceedings of the National Academy of Sciences of the United States of America, **103**(13), 4813–8, 2006.

[58] T. R. Rodriguez and R. García. *Compositional mapping of surfaces in atomic force microscopy by excitation of the second normal mode of the microcantilever.* Applied Physics Letters, **84**(3), 449, 2004.

[59] N. F. Martínez, J. R. Lozano, E. T. Herruzo, F. Garcia, C. Richter, T. Sulzbach and R. García. *Bimodal atomic force microscopy imaging of isolated antibodies in air and liquids.* Nanotechnology, **19**(38), 384011, 2008.

[60] J. R. Lozano and R. García. *Theory of phase spectroscopy in bimodal atomic force microscopy.* Physical Review B, **79**(1), 014110, 2009.

[61] J. W. Li, J. P. Cleveland and R. Proksch. *Bimodal magnetic force microscopy: Separation of short and long range forces.* Applied Physics Letters, **94**(16), 163118, 2009.

[62] S. Kawai, T. Glatzel, S. Koch, B. Such, A. Baratoff and E. Meyer. *Systematic Achievement of Improved Atomic-Scale Contrast via Bimodal Dynamic Force Microscopy.* Physical Review Letters, **103**(22), 1–4, 2009.

[63] J. Melcher, C. Carrasco, X. Xu, J. L. Carrascosa, J. Gómez-Herrero, P. José de Pablo and A. Raman. *Origins of phase contrast in the atomic force microscope in liquids.* Proceedings of the National Academy of Sciences of the United States of America, **106**(33), 13655–60, 2009.

[64] E. T. Herruzo, H. Asakawa, T. Fukuma and R. García. *Three-dimensional quantitative force maps in liquid with 10 piconewton, angstrom and sub-minute resolutions.* Nanoscale, 2012.

[65] M. Aksoy and A. Atalar. *Force spectroscopy using bimodal frequency modulation atomic force microscopy.* Physical Review B, **83**(7), 1–6, 2011.

[66] D. Martinez-Martin, E. T. Herruzo, C. Dietz, J. Gomez-Herrero and R. García. *Noninvasive Protein Structural Flexibility Mapping by Bimodal Dynamic Force Microscopy.* Physical Review Letters, **106**(19), 198101, 2011.

[67] E. T. Herruzo and R. García. *Theoretical study of the frequency shift in bimodal FM-AFM by fractional calculus.* Beilstein journal of nanotechnology, **3**, 198–206, 2012.

[68] S. D. Solares and G. Chawla. *Triple-frequency intermittent contact atomic force microscopy characterization: Simultaneous topographical, phase, and frequency shift contrast in ambient air.* Journal of Applied Physics, **108**(5), 054901, 2010.

[69] S. Jesse, S. V. Kalinin, R. Proksch, A. P. Baddorf and B. J. Rodriguez. *The band excitation method in scanning probe microscopy for rapid mapping of energy dissipation on the nanoscale.* Nanotechnology, **18**(43), 435503, 2007.

[70] S. Jesse and S. V. Kalinin. *Band excitation in scanning probe microscopy: sines of change.* Journal of Physics D: Applied Physics, **44**(46), 464006, 2011.

[71] D. Platz, E. A. Tholén, D. Pesen and D. B. Haviland. *Intermodulation atomic force microscopy.* Applied Physics Letters, **92**(15), 153106, 2008.

[72] D. Platz, E. A. Tholén, C. Hutter, A. C. von Bieren and D. B. Haviland. *Phase imaging with intermodulation atomic force microscopy.* Ultramicroscopy, **110**(6), 573–7, 2010.

[73] J. L. Hutter and J. Bechhoefer. *Calibration of atomic-force microscope tips.* Review of Scientific Instruments, **64**(7), 1868, 1993.

[74] J. E. Sader, I. Larson, P. Mulvaney and L. R. White. *Method for the calibration of atomic force microscope cantilevers.* Review of Scientific Instruments, **66**(7), 3789, 1995.

[75] J. E. Sader, J. W. M. Chon and P. Mulvaney. *Calibration of rectangular atomic force microscope cantilevers.* Review of Scientific Instruments, **70**(10), 3967, 1999.

[76] M. J. Higgins, R. Proksch, J. E. Sader, M. Polcik, S. Mc Endoo, J. P. Cleveland and S. P. Jarvis. *Noninvasive determination of optical lever sensitivity in atomic force microscopy.* Review of Scientific Instruments, **77**(1), 013701, 2006.

[77] E. A. Tholén, A. Ergül, E. M. Doherty, F. M. Weber, F. Grégis and D. B. Haviland. *Nonlinearities and parametric amplification in superconducting coplanar waveguide resonators.* Applied Physics Letters, **90**(25), 253509, 2007.

[78] E. A. Tholén, A. Ergül, K. Stannigel, C. Hutter and D. B. Haviland. *Parametric amplification with weak-link nonlinearity in superconducting microresonators.* Physica Scripta, **T137**, 014019, 2009.

[79] R. B. Boyd. *Nonlinear Optics.* Academic Press, 3 edition, 2008.

[80] E. W. Hagley, J. Wen, P. S. Julienne, J. E. Simsarian, K. Helmerson, S. L. Rolston and W. D. Phillips. *Four-wave mixing with matter waves.* Nature, **398**(March), 218–220, 1999.

[81] V. Eguíluz, M. Ospeck, Y. Choe, A. Hudspeth and M. Magnasco. *Essential Nonlinearities in Hearing.* Physical Review Letters, **84**(22), 5232–5235, 2000.

[82] F. Jülicher, D. Andor and T. Duke. *Physical basis of two-tone interference in hearing.* Proceedings of the National Academy of Sciences of the United States of America, **98**(16), 9080–5, 2001.

[83] L. Robles and M. A. Ruggero. *Mechanics of the mammalian cochlea.* Physiological reviews, **81**(3), 1305–52, 2001.

[84] G. Tartini. *Trattato di musica secondo la vera scienza dell'armonia.* 1754.

[85] D. Platz, D. Forchheimer, E. A. Tholén and D. B. Haviland. *Interaction imaging with amplitude-dependence force spectroscopy.* Nature Communications, **4**, 1360, 2013.

[86] M. Li, H. X. Tang and M. L. Roukes. *Ultra-sensitive NEMS-based cantilevers for sensing, scanned probe and very high-frequency applications.* Nature nanotechnology, **2**(2), 114–20, 2007.

[87] T. Ando, T. Uchihashi and T. Fukuma. *High-speed atomic force microscopy for nano-visualization of dynamic biomolecular processes.* Progress in Surface Science, **83**(7-9), 337–437, 2008.

[88] L. Mininni, A. Slade, J. Kindt and S. Hu. *High-Speed Atomic Force Microscopy Enables New Applications.* Microscopy Today, **19**(06), 12–15, 2011.

[89] M. Dong, S. Husale and O. Sahin. *Determination of protein structural flexibility by microsecond force spectroscopy.* Nature nanotechnology, **4**(8), 514–7, 2009.

[90] E. A. Tholén, D. Platz, D. Forchheimer, V. Schuler, M. O. Tholén, C. Hutter and D. B. Haviland. *Note: The intermodulation lockin analyzer.* Review of Scientific Instruments, **82**(2), 026109, 2011.

[91] *Python Programming Language.* URL `www.python.org`.

[92] *wxPython.* URL `http://www.wxpython.org/`.

[93] *SciPy: Open source scientific tools for Python.* URL `www.scipy.org`.

[94] *matplotlib.* URL `matplotlib.org`.

[95] J. D. Hunter. *Matplotlib: A 2D Graphics Environment.* Computing in Science & Engineering, **9**(3), 90–95, 2007.

[96] *Mercurial SCM.* URL `http://mercurial.selenic.com/`.

[97] D. Platz, D. Forchheimer, E. A. Tholén, C. Hutter and D. B. Haviland. *Effect of Material Stiffness on Intermodulation Response in Dynamic Atomic Force Microscopy.* In *Volume 4: 12th International Conference on Advanced Vehicle and Tire Technologies; 4th International Conference on Micro- and Nanosystems*, pages 499–506. ASME, 2010.

[98] B. V. Derjaguin, V. M. Muller and Y. P. Toporov. *Effect of contact deformations on the adhesion of particles.* Journal of Colloid and Interface Science, **53**(2), 314–326, 1975.

[99] A. C. Hindmarsh, P. N. Brown, K. E. Grant, S. L. Lee, R. Serban, D. E. Shumaker and C. S. Woodward. *SUNDIALS: Suite of nonlinear and differential/algebraic equation solvers.* ACM Transactions on Mathematical Software, **31**(3), 363–396, 2005.

[100] D. Platz, D. Forchheimer, E. A. Tholén and D. B. Haviland. *Interpreting motion and force for narrow-band intermodulation atomic force microscopy.* Beilstein Journal of Nanotechnology, **4**, 45–56, 2013.

[101] J. Tamayo and R. García. *Effects of elastic and inelastic interactions on phase contrast images in tapping-mode scanning force microscopy.* Applied Physics Letters, **71**(16), 2394, 1997.

[102] J. P. Cleveland, B. Anczykowski, A. E. Schmid and V. B. Elings. *Energy dissipation in tapping-mode atomic force microscopy.* Applied Physics Letters, **72**(20), 2613, 1998.

[103] B. Anczykowski, B. Gotsmann, H. Fuchs, J. P. Cleveland and V. B. Elings. *How to measure energy dissipation in dynamic mode atomic force microscopy.* Applied Surface Science, **140**(3-4), 376–382, 1999.

[104] U. Dürig. *Conservative and dissipative interactions in dynamic force microscopy.* Surface and Interface Analysis, **27**(56), 467–473, 1999.

[105] B. Gotsmann, C. Seidel, B. Anczykowski and H. Fuchs. *Conservative and dissipative tip-sample interaction forces probed with dynamic AFM.* Physical Review B, **60**(15), 11051–11061, 1999.

[106] U. Dürig. *Interaction sensing in dynamic force microscopy.* New Journal of Physics, **2**, 5, 2000.

[107] H. Hölscher, B. Gotsmann, W. Allers, U. D. Schwarz, H. Fuchs and R. Wiesendanger. *Measurement of conservative and dissipative tip-sample interaction forces with a dynamic force microscope using the frequency modulation technique.* Physical Review B, **64**(7), 1–6, 2001.

[108] R. García, C. Gómez, N. Martinez, S. Patil, C. Dietz and R. Magerle. *Identification of Nanoscale Dissipation Processes by Dynamic Atomic Force Microscopy.* Physical Review Letters, **97**(1), 016103, 2006.

[109] L. Zitzler, S. Herminghaus and F. Mugele. *Capillary forces in tapping mode atomic force microscopy.* Physical Review B, **66**(15), 1–8, 2002.

[110] D. Platz, D. Forchheimer, E. A. Tholén and D. B. Haviland. *Tip-surface interactions in dynamic atomic force microscopy.* manuscript, 2013.

[111] C. Hutter, D. Platz, E. A. Tholén, T. H. Hansson and D. B. Haviland. *Reconstructing Nonlinearities with Intermodulation Spectroscopy.* Physical Review Letters, **104**(5), 050801, 2010.

[112] D. Platz, D. Forchheimer, E. A. Tholén and D. B. Haviland. *The role of nonlinear dynamics in quantitative atomic force microscopy.* Nanotechnology, **23**(26), 265705, 2012.

[113] D. Platz, D. Forchheimer, E. A. Tholén and D. B. Haviland. *Polynomial force approximations and multifrequency atomic force microscopy.* accepted for publication in Beilstein Journal of Nanotechnology, 2013.

[114] D. Forchheimer, D. Platz, E. A. Tholén and D. B. Haviland. *Model-based extraction of material properties in multifrequency atomic force microscopy.* Physical Review B, **85**(19), 195449, 2012.

[115] D. Forchheimer, D. Platz, E. A. Tholén and D. B. Haviland. *Simultaneous quantitative imaging of surface and magnetic forces.* submitted, 2013.

[116] G. B. Arfken and H. J. Weber. *Mathematical methods for physicists.* Elsevir Academic Press, 2005.

[117] H. Hölscher, W. Allers, U. D. Schwarz, A. Schwarz and R. Wiesendanger. *Determination of Tip-Sample Interaction Potentials by Dynamic Force Spectroscopy.* Physical Review Letters, **83**(23), 4780–4783, 1999.

[118] A. M. Cormack. *Representation of a Function by Its Line Integrals, with Some Radiological Applications.* Journal of Applied Physics, **34**(9), 2722, 1963.

[119] J. A. Fawcett. *Inversion of N -Dimensional Spherical Averages.* SIAM Journal on Applied Mathematics, **45**(2), 336–341, 1985.

[120] L.-E. Andersson. *On the Determination of a Function from Spherical Averages.* SIAM Journal on Mathematical Analysis, **19**(1), 214–232, 1988.

[121] H. Hellsten and L.-E. Andersson. *An inverse method for the processing of synthetic aperture radar data.* Inverse Problems, **3**(1), 111–124, 1987.

[122] W. Munk, P. Worcester and C. Wunsch. *Ocean Acoustic Tomography (Cambridge Monographs on Mechanics).* Cambridge University Press, 1995.

[123] E. T. Quinto, A. Rieder and T. Schuster. *Local inversion of the sonar transform regularized by the approximate inverse.* Inverse Problems, **27**(3), 035006, 2011.

[124] M. Unser and A. Aldroubi. *A review of wavelets in biomedical applications.* Proceedings of the IEEE, **84**(4), 626–638, 1996.

[125] J. J. Benedetto and A. I. Zayed. *Sampling, Wavelets, and Tomography (Applied and Numerical Harmonic Analysis).* Birkhäuser, 2004.

[126] I. N. Bronstein, K. A. Semendjajew, G. Musiol and H. Mühlig. *Taschenbuch der Mathematik.* Harri Deutsch, 5 edition, 2000.

Appendix

A.1 Fabrication of the PS/PMMA blend sample

The PS/PMMA blend sample studied in references [85, 113] used PS (M_w = 280 kDa), PMMA (M_w = 120 kDa) and toluene obtained from Sigma-Aldrich as purchased. The polymers were dissolved in toluene at a concentration of 0.52 wt% and 30 μL of the solution were spin-cast on a silicon substrate for 30 s at 2150 rpm. The silicon substrate was cleaned in acetone for 20 minutes at 50 °C in an ultrasonic cleaner bath (VWR USC300D, strength 7) and surface activated for 4 minutes in an oxygen plasma (Oxford Instruments PlasmaLab 80 Plus RIE/ICP) at a flow rate of 80 sccm at a pressure of 40 mTorr directly before spin-casting.

A.2 The double Abel transform

The Abel transform $\mathcal{A}$ of differentiable function f is defined as

$$(\mathcal{A}f)(x) = \int_0^x \frac{f(t)}{\sqrt{x-t}} dt. \tag{A.1}$$

Applying the Abel transform twice to a function yields the antiderivative of the original function:

$$(\mathcal{A}^2 f)(x) = \int_0^x \frac{1}{\sqrt{x-t}} \int_0^t \frac{f(t')}{\sqrt{t-t'}} dt' dt \tag{A.2}$$

Applying Fubini's theorem which yields

$$(\mathcal{A}^2 f)(x) = \int_0^x f(t') \int_{t'}^x \frac{1}{\sqrt{x-t}\sqrt{t-t'}} dt dt' \tag{A.3}$$

$$= \pi \int_0^x f(t) dt \tag{A.4}$$

where the last integral in equation (A.3) has been evaluated using integral no. 146 in[126].

A.3 Derivations of the atomic force tomography equations

For the force defined in equation (5.24) the in-phase force component is given by

$$F_I(h,A) = \frac{1}{2\pi}\int_0^{2\pi} f_{\mathrm{c}}(A\cos\theta + h, A\sin\theta)\cos\theta d\theta \tag{A.5}$$

where we consider the oscillation frequency $\bar{\omega}$ as constant. The force f_{c} can be written in terms of its two dimensional Fourier transform $f_{\mathrm{c}}^{(\mathcal{F},\mathcal{F})}$ where the superscript $(\mathcal{F},\mathcal{F})$ denotes a Fourier transform in the first and the second argument of f_{c}. Using the force Fourier transform in equation (A.5) yields

$$\begin{aligned} F_I(h,A) &= \frac{1}{2\pi}\int_{-\infty}^{\infty}\int_{-\infty}^{\infty} f_{\mathrm{c}}^{(\mathcal{F},\mathcal{F})}(k_x,k_y)e^{ik_x h} \\ &\quad \times \int_0^{2\pi} e^{i(k_x A\cos\theta + k_y A\sin\theta)}\cos\theta d\theta dk_x dk_y \qquad \text{(A.6)} \\ &= \frac{1}{2\pi}\int_{-\infty}^{\infty}\int_{-\infty}^{\infty} f_{\mathrm{c}}^{(\mathcal{F},\mathcal{F})}(k_x,k_y)e^{ik_x h} \\ &\quad \times \int_0^{2\pi} e^{i\sqrt{k_x^2+k_y^2}A\cos(\theta+\psi(k_x,k_y))}\cos\theta d\theta dk_x dk_y \qquad \text{(A.7)} \end{aligned}$$

where

$$\psi(k_x,k_y) = \operatorname{atan2}(k_x,k_y) - \frac{\pi}{2}. \tag{A.8}$$

The atan2 is a arctangent function which ensures the correct quadrant for the computed angle depending on the signs of k_x and k_y. It is a smooth function of k_x and k_y except for the negative k_x axis where it exhibits a discontinuous jump of 2π. By introducing $\theta' = \theta + \psi$ we can further rewrite the integral equation for F_I

$$\begin{aligned} F_I(h,A) &= \frac{1}{2\pi}\int_{-\infty}^{\infty}\int_{-\infty}^{\infty} f_{\mathrm{c}}^{(\mathcal{F},\mathcal{F})}(k_x,k_y)e^{ik_x h}\int_{\psi}^{2\pi+\psi} e^{i\sqrt{k_x^2+k_y^2}A\cos\theta'} \\ &\quad \times(\cos\theta'\cos\psi + \sin\theta'\sin\psi)\,d\theta' dk_x dk_y \qquad \text{(A.9)} \\ &= i\int_{-\infty}^{\infty}\int_{-\infty}^{\infty} f_{\mathrm{c}}^{(\mathcal{F},\mathcal{F})}(k_x,k_y)\cos\left(\psi(k_x,k_y)\right) \\ &\quad \times e^{ik_x h}J_1\left(\sqrt{k_x^2+k_y^2}A\right)dk_x dk_y \qquad \text{(A.10)} \end{aligned}$$

where we have used the 2π periodicity of the complex exponential function and the cosine function and the Jacobi-Anger expansion

$$e^{i\sqrt{k_x^2+k_y^2}A\cos\theta} = \sum_{n=-\infty}^{\infty} i^n J_n\left(\sqrt{k_x^2+k_y^2}A\right)e^{in\theta} \tag{A.11}$$

involving the Bessel functions of first kind J_n. To solve equation (A.10) for the force f_{c} we Fourier transform F_I in the height coordinate h and Hankel transform

it in the amplitude argument A such that

$$F_I^{\left(\mathcal{F},\mathcal{H}^{(1)}\right)}(k,\lambda) = i\int_{-\infty}^{\infty} f_{\mathrm{c}}^{(\mathcal{F},\mathcal{F})}(k,k_y)\cos\left(\psi(k,k_y)\right)\frac{1}{\lambda}\delta\left(\lambda-\sqrt{k^2+k_y^2}\right)dk_y \tag{A.12}$$

where $\mathcal{H}_1$ denotes the first Hankel transform δ is the Dirac delta function and we have used the orthogonality relations

$$\int_{-\infty}^{\infty} e^{i(k-k')x}dx = 2\pi\delta(k-k') \tag{A.13}$$

$$\int_0^{\infty} J_n(\lambda x)J_n(\rho x)xdx = \frac{1}{\lambda}\delta(\lambda-\rho) \tag{A.14}$$

The two dimensional function $f_{\mathrm{c}}(x,y)$ is the effective conservative part of the total tip-surface force which is symmetric in the second coordinate (velocity coordinate). Thus, its two dimensional Fourier transform $f_{\mathrm{c}}^{(\mathcal{F},\mathcal{F})}$ is symmetric in the second coordinate as well. The phase function $\cos(\psi)$ is also symmetric in the second coordinate and we can restrict the lower integration limit in equation (A.12) to zero such that

$$F_I^{\left(\mathcal{F},\mathcal{H}^{(1)}\right)}(k,\lambda) = \frac{2i}{\sqrt{\lambda^2-k^2}} f_{\mathrm{c}}^{(\mathcal{F},\mathcal{F})}(k,\sqrt{\lambda^2-k^2})\cos\left(\psi\left(k,\sqrt{\lambda^2-k^2}\right)\right) \tag{A.15}$$

If $\cos(\psi)\neq 0$ we can solve for the Fourier transform of the force which we can write as

$$f_{\mathrm{c}}^{(\mathcal{F},\mathcal{F})}(k_x,k_y) = \frac{|k_y|}{2i}\frac{F_I\left(k_x,\sqrt{k_x^2+k_y^2}\right)}{\cos\left(\psi(k_x,k_y)\right)} \tag{A.16}$$

for the redefined variables $k_x = k$ and $k_y = \sqrt{\lambda^2-k^2}$.

The quadrature force component F_Q is defined in a similar way with the non-conservative part f_{nc} of the total tip-surface force and with $\sin\theta$ as the Fourier weight factor,

$$F_Q(h,A) = \frac{1}{2\pi}\int_0^{2\pi} f_{\mathrm{nc}}(A\cos\theta+h, A\sin\theta)\sin\theta d\theta \tag{A.17}$$

Following the same steps as above we can write F_Q as

$$F_I^{\left(\mathcal{F},\mathcal{H}^{(1)}\right)}(k,\lambda) = \frac{2i}{\sqrt{\lambda^2-k^2}} f_{\mathrm{nc}}^{(\mathcal{F},\mathcal{F})}(k,\sqrt{\lambda^2-k^2})\sin\left(\psi\left(k,\sqrt{\lambda^2-k^2}\right)\right) \tag{A.18}$$

where we have used that both f_{nc} and $\sin(\psi)$ are anti-symmetric in the second coordinate. For $\sin(\psi)\neq 0$ we can solve for the Fourier transform of the non-conservative force,

$$f_{\mathrm{nc}}^{(\mathcal{F},\mathcal{F})}(k_x,k_y) = \frac{|k_y|}{2i}\frac{F_I\left(k_x,\sqrt{k_x^2+k_y^2}\right)}{\sin\left(\psi(k_x,k_y)\right)} \tag{A.19}$$

Acknowledgments

This work would not have been possible without the support of numerous people which I would like to acknowledge.

First of all, I would like to thank my supervisor Prof. David Haviland for giving me the opportunity to join the Nanostructure Physics group at KTH, for supporting me in good and in difficult times and showing me that physics in not either experiment or theory. I would not have accomplished this work without his unbreakable enthusiasm and optimism. I would also like to thank Prof. Vlad Korenivski for asking difficult questions about my research, fundamental physics and life. Special thanks to Dr. Erik Tholén for introducing me to physical measurements and reminding me that simple solutions are usually the best solutions. Daniel Forchheimer deserves a special thank for perfecting the experimental setup and working with samples with enormous patience and persistence. I thank Dr. Carsten Hutter for helping to develop both elegant theory and powerful software. Dr. Stanislav Borysov for continuing the theoretical work. Thank you Arndt von Bieren, Dr. Adrian Iovan, Dr. David Schaeffer and Adem Ergül for helping me with sample fabrication. Dr. Devrim Pesen for providing the sample for our first paper and helping me doing the first steps with the AFM. A special thanks also to Dr. Anders Liljeborg for running the clean room and offering a helping hand for any kind of computer problem. Prof. Hans Hansson, Prof. Alexander Balatsky and Dr. Astrid de Wijn for contributing to numerous discussion rounds.

I would like to thank all the present and former members of the Nanostructure Physics group at KTH and the Experimental Condensed Matter Physics group at Stockholm University for creating such a nice working atmosphere.

Finally, I would like thank my family and my friends. Thank you for all your support and for just being there.

Daniel Platz
Stockholm, May 2013

"Am Ziel deiner Wünsche wirst Du jedenfalls eines vermissen: dein Wandern zum Ziel."

(When you have reached the objective of your desires, you will surely miss the wandering path toward them.)

Marie von Ebner-Eschenbach (1830-1916)
Austrian writer

Part II

Papers

List of publications

- **Paper I**
  Daniel Platz, Erik A. Tholén, Devrim Pesen and David B. Haviland. *Intermodulation atomic force microscopy*. Applied Physics Letters **92**, 153106 (2008)
  I built the data acquisition system and performed the experiments. I analyzed the data and prepared the figures for the manuscript. I took part in writing the manuscript.

- **Paper II**
  Daniel Platz, Erik A. Tholén, Carsten Hutter, Arndt C. von Bieren and David B. Haviland. *Phase imaging with intermodulatino atomic force microscopy*. Ultramicroscopy **110**, 573-577 (2010)
  I built the data acquisition system, took part in fabricating the sample and performed the experiments. I took part in writing the manuscript and prepared the figures.

- **Paper III**
  Carsten Hutter, Daniel Platz, Erik A. Tholén, Thor H. Hansson and David B. Haviland. *Reconstructing Nonlinearities with Intermodulation Spectroscopy*. Physical Review Letters **104**, 050801 (2010)
  I contributed to the development of the reconstruction method and to discussions leading to the manuscript.

- **Paper IV**
  Erik A. Tholén, Daniel Platz, Daniel Forchheimer, Vivien Schuler, Mats O. Tholén, Carsten Hutter and David B. Haviland. *Note: The intermodulation lockin analyzer*. Review of Scientific Instruments **82**, 026109 (2011)
  I contributed to the development of the design specifications of the intermodulation lock-in analyzer and to the external control software. I performed and assisted the measurements and prepared figures for the manuscript.

- **Paper V**
  Daniel Platz, Daniel Fochheimer, Erik A. Tholén and David B. Haviland. *The role of nonlinear dynamics in quantitative atomic force microscopy*. Nanotechnology **23**, 265705 (2012)
  I developed and implemented the theory for the polynomial reconstruction method. I developed the code for the numerical simulations. I took part in writing of the manuscript.

- **Paper VI**
  Daniel Forchheimer, Daniel Platz, Erik A. Tholén and David B. Haviland. *Model-based extraction of material properties in multifrequency atomic force microscopy*. Physical Review B **85**, 195449 (2012)

I took part in discussions about the fit method and contributed to the discussions around the manuscript.

- **Paper VII**
  Daniel Platz, Daniel Forchheimer, Erik A. Tholén and David B. Haviland. *Interaction imaging with amplitude-dependence force spectroscopy*. Nature Communications **4**, 1360 (2013)
  I developed the theory, performed the data analysis and fabricated the PS/PMMA sample. I contributed to the measurements and led the writing of the manuscript. I prepared all the figures for the manuscript.

- **Paper VIII**
  Daniel Platz, Daniel Forchheimer, Erik A. Tholén and David B. Haviland. *Interpreting motion and force for narrow band intermodulation atomic force microscopy*. Beilstein Journal of Nanotechnology **4**, 45-56 (2013)
  I developed the theory and performed the simulations. I fabricated the sample, performed the measurements and analyzed the data. I led the writing of the manuscript and prepared the figures.

- **Paper IX**
  Daniel Platz, Daniel Forchheimer, Erik A. Tholén and David B. Haviland. *Polynomial force reconstruction and multifrequency atomic force microscopy*. accepted for publication in Beilstein Journal of Nanotechnology, arXiv:1302.1829
  I fabricated the sample, performed the experiments, analyzed the data and developed the extended generalized polynomial reconstruction. I led the writing of the manuscript and prepared the figures.

- **Paper X**
  Daniel Platz, Daniel Forchheimer, Erik A. Tholén and David B. Haviland. *Tip-surface interactions in dynamic atomic force microscopy*. arXiv:1301.7340
  I developed the theory and performed the simulations. I led the writing of the manuscript and prepared the figures.

Publications not included in this thesis

- Daniel Platz, Daniel Forchheimer, Erik A. Tholén, Carsten Hutter and David B. Haviland. *Effect of material stiffness on intermodulation response in dynamic atomic force microscopy*. Proceedings of the ASME 2010 International Design Engineering Technical Conferences & Computers and Information in Engineering Conference IDETC/CIE 2010.

- Daniel Forchheimer, Daniel Platz, Erik A. Tholén and David B. Haviland. *Simultaneous quantitative imaging of surface and magnetic forces*. arXiv:1303.2134

- Stanislav S. Borysov, Daniel Platz, Daniel Forchheimer, Astrid S. de Wijn, Erik A. Tholén, Alexander V. Balatsky and David B. Haviland. *Reconstruction of Tip-Surface Interactions with Multimodal Intermodulation Atomic Force Microscopy*. arXiv:1305.0167